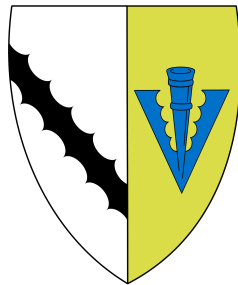




UNIVERSITY OF  
CAMBRIDGE

# Three-dimensional spectroscopy of galaxies in the early Universe



**Joris Nicolaas Witstok**

Supervisors:

Dr Renske Smit, Prof Roberto Maiolino

Department of Physics  
University of Cambridge

This dissertation is submitted for the degree of  
*Doctor of Philosophy*



---

I would like to dedicate this thesis to my loving parents ...



## DECLARATION

---

I hereby declare that except where specific reference is made to the work of others, the contents of this dissertation are original and have not been submitted in whole or in part for consideration for any other degree or qualification in this, or any other university. This thesis is my own work and contains nothing which is the outcome of work done in collaboration with others, except as specified in the text and Acknowledgements. This dissertation contains fewer than 60 000 words including abstract, tables, and footnotes, but excluding table of contents, photographs, diagrams, figure captions, list of figures, list of abbreviations, bibliography, appendices and acknowledgements.

Joris Nicolaas Witstok  
January 2022



## ACKNOWLEDGEMENTS

---

First of all, I would like to acknowledge the Institute of Astronomy for having made possible this research. Also, my gratitude goes out to the the developers of all software packages used for this research:

- PYTHON, and its packages: the SCIPY library ([Jones et al., 2001](#)), NUMPY ([Van der Walt et al., 2011](#)), MATPLOTLIB ([Hunter, 2007](#)), and ASTROPY ([Astropy Collaboration et al., 2013, 2018](#)).
- SAOIMAGE DS9 and TOPCAT (Tool for OPerations on Catalogues And Tables)
- The LaTeX distribution ([CITE](#))

Special thanks goes to Ewald, Girish, and Martin for all their assistance, useful advice, and enlightening discussions.



## ABSTRACT

---

**Key words:** Intergalactic medium – Large-scale structure of Universe – Diffuse radiation – Cosmology: theory – Methods: numerical



## TABLE OF CONTENTS

---

<b>Introduction</b>	<b>3</b>
<b>1 Prospects for observing the low-density cosmic web in Lyman-<math>\alpha</math> emission</b>	<b>7</b>
1.1 Introduction . . . . .	7
1.2 Methodology . . . . .	9
1.2.1 Ly $\alpha$ emission through recombination . . . . .	10
1.2.2 Ly $\alpha$ emission through collisional excitation . . . . .	13
1.2.3 Emissivity . . . . .	14
1.2.4 Cosmological hydrodynamical simulation . . . . .	14
1.3 Results . . . . .	16
1.3.1 Luminosity density . . . . .	16
1.3.2 Surface brightness maps . . . . .	22
1.3.3 Observing facilities . . . . .	23
1.3.4 Simulated observations . . . . .	27
1.4 Conclusions . . . . .	34
<b>2 Assessing the sources of reionisation: a spectroscopic case study of a 30<math>\times</math> lensed galaxy at <math>z \sim 5</math> with Ly<math>\alpha</math>, C iv, Mg ii, and [Ne iii]</b>	<b>37</b>
2.1 Introduction . . . . .	37
2.2 Observations . . . . .	39
2.2.1 X-shooter spectroscopy . . . . .	39
2.2.2 SINFONI spectroscopy . . . . .	41
2.2.3 <i>HST</i> imaging . . . . .	41
2.3 Results . . . . .	42
2.3.1 X-shooter . . . . .	42
2.3.2 SINFONI . . . . .	44
2.4 Discussion . . . . .	44
2.4.1 C iv: driven by star formation or AGN activity? . . . . .	44
2.4.2 The [Ne III]/[O II] line ratio as an ionisation and metallicity diagnostic alternative to [O III]/[O II] . . . . .	47

## Table of contents

---

2.4.3	LyC escape traced by Ly $\alpha$ and Mg II emission . . . . .	58
2.5	Summary . . . . .	61
<b>References</b>		<b>63</b>
<b>Appendix A</b>	<b>Modelling Lyman-<math>\alpha</math> emission</b>	<b>71</b>
A.1	Model parameters and fitting functions . . . . .	71
A.1.1	Emission processes . . . . .	71
A.2	Ly $\alpha$ optical depth . . . . .	76
A.3	Redshift evolution . . . . .	77
<b>Appendix B</b>	<b>Assessing the sources of reionisation: a spectroscopic case study of a 30<math>\times</math> lensed galaxy at <math>z \sim 5</math> with Ly<math>\alpha</math>, C IV, Mg II, and [Ne III]</b>	<b>79</b>
B.1	Mg II and C III significance . . . . .	79
B.2	SDSS selection . . . . .	80
B.3	JWST ETC calculation . . . . .	82

## LIST OF FIGURES

---

I.1	Hubble Ultra-Deep Field . . . . .	4
1.1	Limiting SB and density quantities as a function of redshift . . . . .	11
1.2	Theoretical Ly $\alpha$ emissivity as a function of temperature . . . . .	12
1.3	Redshift evolution of the Ly $\alpha$ luminosity density . . . . .	17
1.4	Total Ly $\alpha$ surface brightness at $z = 4.8$ . . . . .	18
1.5	Ly $\alpha$ surface brightness of recombination and collisional excitation processes at $z = 4.8$ . . . . .	19
1.6	Ly $\alpha$ luminosities of recombination and collisional excitation processes in phase space at $z = 4.8$ . . . . .	20
1.7	Inferred noise in the MUSE HDFS observation . . . . .	26
1.8	Observed Ly $\alpha$ surface brightness at $z = 4.8$ . . . . .	28
1.9	Overview surface brightness map at $z = 4.8$ for different noises and density cut-offs	29
1.10	Observed Ly $\alpha$ surface brightness at $z = 4.8$ . . . . .	30
2.1	Overview of the observations discussed in Sects. 2.2.1 to 2.2.3 . . . . .	40
2.2	C IV/He II line ratio diagnostics . . . . .	45
2.3	Measurements of [Ne III]/[O II] line ratios of local and high-redshift galaxies .	48
2.4	Correlation between the [Ne III]/[O II] and [O III]/[O II] line ratios of SDSS galaxies	50
2.5	Offsets from the FMR . . . . .	53
2.6	EWs of Ly $\alpha$ and Mg II $\lambda 2796$ . . . . .	56
2.7	Escape fractions compared to velocity offsets of Ly $\alpha$ and Mg II $\lambda 2796$ . . . . .	57
A.1	2D histogram of Ly $\alpha$ optical depth $\tau$ and overdensity $\rho/\bar{\rho}$ at $z = 4.8$ . . . . .	73
A.2	Observed column density at $z = 4.8$ . . . . .	74
A.3	Observed Ly $\alpha$ surface brightness at different redshifts . . . . .	75
B.1	Various X-shooter spectra of Mg II . . . . .	80
B.2	Non-detections of C III . . . . .	81



## LIST OF TABLES

---

1.1	Observational experiments . . . . .	24
2.1	Observational results . . . . .	39
A.1	Coefficients $c_i$ in Eq. (A.4) . . . . .	72
B.1	Significance of the Mg II detection . . . . .	79



## ABSTRACT

---

**Key words:** Intergalactic medium – Large-scale structure of Universe – Diffuse radiation – Cosmology: theory – Methods: numerical



## INTRODUCTION

---

*“We are just an advanced breed of monkeys on a minor planet of a very average star. But we can understand the Universe. That makes us something very special.”*

Stephen Hawking

Arguably the oldest and most prominent question in the history of humanity, captivating not only many philosophers and scientists, but really all humankind – both religious and irreligious, wise and unsophisticated, civilised and uncivilised – is

“*Where do we come from?*”

Among other related questions, this might even be the one that drove humans to engage in an endeavour that we presently categorise as *science*, and for many, it probably still is the profound motivation to continue investigating nature and the astonishing phenomena it presents us. Although seemingly simple, it has proven to be one of the most difficult scientific questions to answer – if it even can be identified as a proper scientific question, given its broad and universal character.

Even so, many have made great progress on finding the answer to this mystery. There are numerous possible approaches to achieving this, but to scientifically divide up this general question into specific and rational problems seems to have proven the most successful and fruitful way.

## The Universe

Through astronomical observations, we have learned a tremendous amount about the *cosmos*, or everything that exists around us. We have, for example, concluded that we reside in the Solar System, and we inhabit one of eight planets orbiting the Sun, a very ordinary star, which itself is part of the Milky Way, an immense collection of stars, mostly very similar to our Sun.

The Milky Way is, again, quite an average galaxy, of which extremely many exist. Astronomers observe them in different shapes and sizes, and even at different times in the past, which is possible due to the finite velocity that light travels with. For this reason, they are able

## Introduction

---

to study their evolution and thereby the evolution of the Universe as a whole. Moreover, this allows for the investigation of the origins of the cosmos by reversing the physical processes that we have identified and can mathematically describe.

However, constrained by observational limits posed to telescopes, mainly due to the astronomical sizes the Universe assumes (the galaxy closest to the Milky Way, Andromeda, is approximately 60 000 000 000 000 times more distant from Earth than the Moon is), many questions still remain to be answered.

Although our understanding of the Universe at this point is far-reaching, many questions about it still remain unanswered. In cosmology, a very robust model of the Universe has been developed over the years, built upon on the theory of General Relativity, and called after its primary components: the Lambda Cold Dark Matter ( $\Lambda$ CDM) cosmological model. This theory has proven extremely successful in explaining a broad range of distinct phenomena, being able to predict the outcome of experiments with very high precision, after having been provided with only a handful of parameters. However, the present model still is undecided about a number of controversies, and is known to have some issues – therefore, it has to be tested rigorously, and possibly amended<sup>1</sup> to match the observational evidence that is continuously supplied or improved upon.

---

<sup>1</sup>Or, according to some, even replaced...

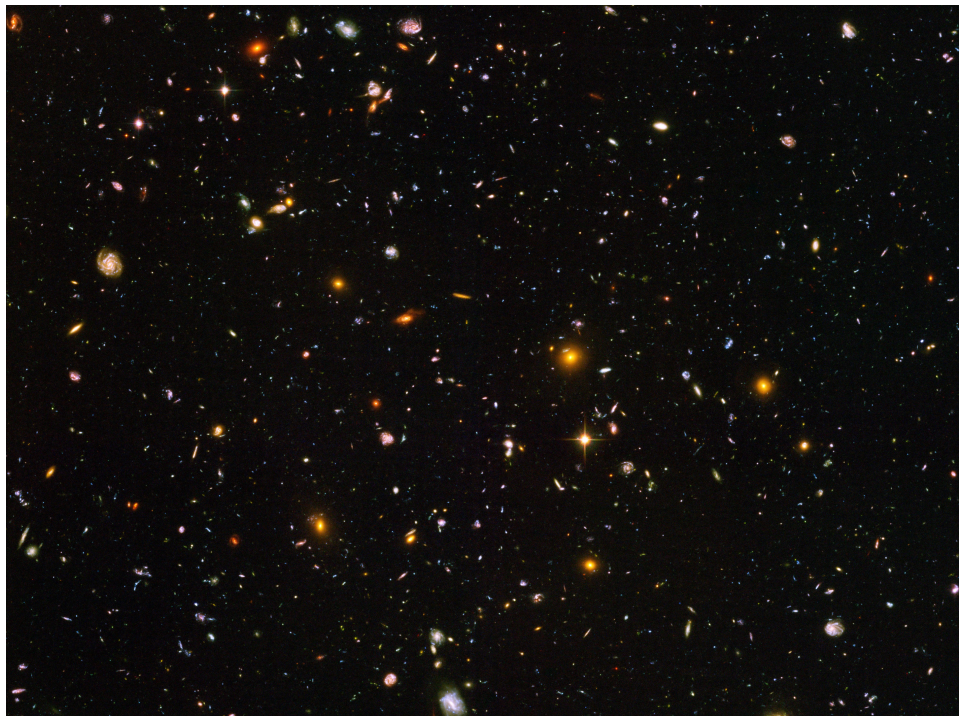


**Figure I.1** Hubble Ultra-Deep Field (HUDF) image, showing a range of distant galaxies in the wavelength range of near-infrared to ultraviolet. Credit: NASA/ESA/Hubble

---

Specifically, the question of how stars precisely are formed in the quantities that eventually together form galaxies that are observed today, assembling with other galaxies to form massive galaxy clusters, that are again part of an even bigger structure – the very largest of structures that we observe in the Universe today, termed the *cosmic web* – is a ubiquitous topic in present cosmological, and indeed astronomical research. The general framework behind the process of the formation of this structure, in which galaxy formation is a vital element, is understood in the  $\Lambda$ CDM model. Still, a variety of subtly different versions of these models have to be tested in order to decide which can explain best how galaxies and other structures have developed, and thereby discover more clearly how the Universe evolved as a whole. The cosmic web is thought to play a major role in this evolution.

## Cosmic web

On the very large scales – that is, at distances of well over 10 Mpc – the Universe is known to exhibit a filamentary structure: this is known as the cosmic web. This web contains most of the matter present in the Universe, leaving large voids with extremely low densities in between the filaments. At the intersection of filamentary structures, galaxies cluster together in groups. Baryonic matter can partly be traced down to reside in stars and gas in these galaxies, whose distribution follows the filamentary structure – surprisingly, however, most of the visible matter in the Universe is actually thought to be located in the *intergalactic medium* (IGM). There, it manifests as a cold, dilute gas; hydrogen is by far the largest constituent of the IGM, while there is little metal enrichment.

## Main research goals

This report investigates...



# CHAPTER 1

## PROSPECTS FOR OBSERVING THE LOW-DENSITY COSMIC WEB IN LYMAN- $\alpha$ EMISSION

---

### 1.1 Introduction

As the reservoir of the majority of baryons in the Universe, the intergalactic medium (IGM) presents an invaluable means to understanding the evolution of cosmic structure (Meiksin, 2009). The IGM has been detected in absorption at a wide range of overdensities out to redshift  $z \sim 6$  using H I Lyman- $\alpha$  (Ly $\alpha$ ) absorption lines in the spectra of background quasars. Successively larger numbers of quasars have been targeted for this purpose, resulting in a large data set of Ly $\alpha$  absorption measurements of the IGM. Before reionisation is completed, understanding the physical state of the IGM is complicated by the rather uncertain details of the emergence of the first stars, black holes, and galaxies during the epoch of reionisation, but the post-reionisation ( $z \lesssim 5.5$ ) IGM should be well described by cosmological hydrodynamical simulations (Cen et al., 1994; Hernquist et al., 1996; Weinberg & et al., 1999; Oñorbe et al., 2017, 2019; Lukić et al., 2015; Bolton et al., 2017). In these simulations, the observed properties of the IGM are reproduced by a fluctuating gas density distribution tracing the cosmic structure formation process. The gas is thereby in ionisation equilibrium with a uniform UV background (UVB) created by galaxies and active galactic nuclei (AGN). This has led to constraints on the ionisation and thermal state of the IGM out to  $z \sim 6$  (Rauch et al., 1997; Davé et al., 1999; Schaye et al., 2000; Meiksin & White, 2003; Faucher-Giguère et al., 2008; Becker et al., 2011; Bolton et al., 2012; Becker & Bolton, 2013; Garzilli et al., 2017; Walther et al., 2019; Khaire et al., 2019) derived from Ly $\alpha$  absorption observations.

In contrast, Ly $\alpha$  emission from the IGM has received relatively little attention, despite a history of just over half a century of theoretically predicted prospects (Partridge & Peebles, 1967; Hogan & Weymann, 1987; Gould & Weinberg, 1996; Fardal et al., 2001; Furlanetto et al., 2003, 2005; Cantalupo et al., 2005; Kollmeier et al., 2010; Faucher-Giguère et al., 2010; Rosdahl & Blaizot, 2012; Silva et al., 2013, 2016; Heneka et al., 2017; Augustin et al., 2019; Elias et al., 2020). Observing intergalactic Ly $\alpha$  emission instead of absorption has distinct

advantages. First, unlike absorption Ly $\alpha$  emission is directly sensitive to the recombination and collisional physics of the neutral as well as the ionised hydrogen content of the IGM and the circumgalactic medium (CGM) that feeds the formation and evolution of galaxies. Second, observations of the Ly $\alpha$  emission allow us to homogeneously probe three-dimensional volumes. Although three-dimensional Ly $\alpha$ -forest studies have now become possible owing to the high number density of observed bright quasars (see e.g. Cisewski et al., 2014), the number of such quasars drops rapidly towards high redshifts (Kulkarni et al., 2019b). Third, observations of Ly $\alpha$  emission can potentially provide independent constraints on the IGM temperature and photoionisation rate, particularly at densities higher than those probed by the Ly $\alpha$  forest ( $\Delta \gtrsim 10$ ).

Using narrowband imaging and integral field unit (IFU) imaging, emission in Ly $\alpha$  from the CGM and/or IGM has now been observed as ‘giant Ly $\alpha$  nebulae’ in the proximity ( $\sim 100$  kpc) of radio-loud and radio-quiet quasars (Djorgovski et al., 1985; Hu et al., 1991; Heckman et al., 1991; McCarthy et al., 1990; Venemans et al., 2007; Villar-Martín et al., 2007; Cantalupo et al., 2008; Humphrey et al., 2008; Rauch et al., 2008; Sánchez & Humphrey, 2009; Rauch et al., 2011; Cantalupo et al., 2012; Rauch et al., 2013; Cantalupo et al., 2014; Martin et al., 2014; Roche et al., 2014; Hennawi et al., 2015; Arrigoni Battaia et al., 2016; Borisova et al., 2016; Fumagalli et al., 2016; Cantalupo, 2017). The circumgalactic hydrogen is strongly affected by ionising radiation from these quasars. Observations suggest that the Ly $\alpha$  emission is mostly recombination radiation and that dense ( $n > 1 \text{ cm}^{-3}$ ), ionised, and relatively cold ( $T \sim 10^4 \text{ K}$ ) pockets of gas should surround massive galaxies (Cantalupo, 2017).

Ly $\alpha$  emission can also result from fluorescent re-emission of the ionising UVB radiation. In the last two decades, significant progress has been made in detecting extended Ly $\alpha$  emission around galaxies (Francis et al., 1996; Fynbo et al., 1999; Keel et al., 1999; Steidel et al., 2000; Hayashino et al., 2004; Rauch et al., 2008; Steidel et al., 2011; Matsuda et al., 2012; Prescott et al., 2013; Momose et al., 2014; Geach et al., 2016; Wisotzki et al., 2016; Cai et al., 2017; Leclercq et al., 2017; Vanzella et al., 2017; Oteo et al., 2018; Wisotzki et al., 2018; Arrigoni Battaia et al., 2019). Using deep ( $\sim 30$  h exposure time) VLT/MUSE observations of the *Hubble* Deep Field South (HDFS) and *Hubble* Ultra-Deep Field (HUDF) reported in Bacon et al. (2015, 2017), the sensitivity of median-stacked radial profiles of Ly $\alpha$  emission currently reaches a surface brightness (SB) of  $\sim 4 \cdot 10^{-21} \text{ erg s}^{-1} \text{ cm}^{-2} \text{ arcsec}^{-2}$  (Wisotzki et al., 2018). This faint signal from Ly $\alpha$  halos can be traced out to projected (physical) galactic radii of  $\sim 60$  kpc (Wisotzki et al., 2018). Even deeper data sets, such as the MUSE Ultra Deep Field (MUDF, described in Lusso et al., 2019) and the MUSE Extremely Deep Field (MXDF, see Bacon et al., 2021) are beginning to be explored. Both will reach a depth of the order of  $\sim 100$  h (i.e. reaching a sensitivity of the order of a few times  $10^{-20} \text{ erg s}^{-1} \text{ cm}^{-2} \text{ arcsec}^{-2}$ ). The Ly $\alpha$  emission coming from the intergalactic gas between galaxies is just beginning to be probed and is the focus of this work.

## **1.2 Methodology**

---

So far, it has proven very difficult to map the spatial distribution of the IGM beyond the CGM and to study its global properties by directly observing the IGM in emission rather than absorption. This has so far only been achieved in special cases, for example in the vicinity of AGN (e.g. [Cantalupo et al., 2014](#); [Martin et al., 2014](#); [Hennawi et al., 2015](#); [Borisova et al., 2016](#); [Umeshata et al., 2019](#)), by applying statistical image processing techniques ([Gallego et al., 2018](#), ; in this case, the CGM only showed a preferential direction of extension towards neighbouring galaxies, no significant signal of filamentary structure in the IGM was found), by cross-correlating Ly $\alpha$  emitters (LAEs) and Ly $\alpha$  intensity mapping ([Kakuma et al., 2019](#)), by observing the thermal Sunyaev-Zel'dovich effect (e.g. [de Graaff et al., 2019](#); [Tanimura et al., 2019](#)), or by detection of warm-hot gas in X-ray emission (e.g. [Kull & Böhringer, 1999](#); [Eckert et al., 2015](#)).

Building on the work of previous studies (such as those by [Gould & Weinberg, 1996](#); [Furlanetto et al., 2003](#); [Cantalupo et al., 2005](#); [Silva et al., 2013, 2016](#)), this work investigates the possibility of such observations. We explore a simulation run based on the Sherwood simulation project ([Bolton et al., 2017](#)), which incorporates an on-the-fly self-shielding model to predict the properties of Ly $\alpha$  emission from the cosmic web. The simulation is aimed at accurately modelling the IGM and employs a modified version of the uniform metagalactic UVB model by [Haardt & Madau \(2012, ; HM12 hereafter\)](#) that is calibrated to match observations of the Ly $\alpha$  forest. The large volume and high dynamic range of the simulation allows us to probe the physical environment of the IGM with well-resolved under- and overdense regions. Moreover, this enables us to study the prospects of an array of current and future observational facilities aiming to detect this emission. We focus on a future reincarnation of VLT/MUSE on next-generation observatories such as the Extremely Large Telescope (ELT) for a more detailed sensitivity analysis.

We describe the simulations used in this work in Sect. 1.2, together with our model for Ly $\alpha$  production in the IGM. Sect. 1.3 presents our results and a discussion of the detection prospects. We summarise our conclusions in Sect. 1.4. Throughout this work, we adopt the cosmological parameters  $\Omega_m = 0.308$ ,  $\Omega_\Lambda = 0.692$ ,  $\Omega_b = 0.0482$ , and  $h = 0.678$  (so  $H_0 = 67.8 \text{ km s}^{-1} \text{ Mpc}^{-1}$ ), taken from the best-fitting  $\Lambda$ CDM model for the combined *Planck*+WP+highL+BAO measurements ([Planck Collaboration et al., 2014](#)). The helium fraction is assumed to be  $f_{\text{He}} = 0.24$ .

## **1.2 Methodology**

Ly $\alpha$  emission from the moderately dense IGM is produced via recombinations and collisional excitations. Recombination is the process in which a free electron is captured by an ion, which in this case is H II. Ly $\alpha$  is emitted provided the recombination leaves hydrogen in an excited state and the last step of the resulting series of energy transition(s) is from energy level  $n = 2$  to  $n = 1$ . Collisional excitation is the effect in which neutral hydrogen (H I) is excited through a

collision with an electron, which can subsequently lead to the emission of Ly $\alpha$  in the same way as with recombinations. We used a hydrodynamical simulation calibrated to UVB constraints from the Ly $\alpha$  forest along with an on-the-fly self-shielding prescription to model these processes.

In the analysis, we focus on low-density gas (below the critical density above which self-shielding becomes a dominant process) as we are primarily interested in detecting emission from the cosmic web. At  $z = 4.8$ , this critical density corresponds to an overdensity  $\Delta \equiv \rho/\bar{\rho} \simeq 100$  (see Sect. 1.2.2). Furthermore, modelling of all relevant feedback and radiative transfer effects becomes increasingly challenging at higher densities.

### 1.2.1 Ly $\alpha$ emission through recombination

#### Emissivity

The underlying equation governing Ly $\alpha$  emission resulting from recombination in a gas containing hydrogen is given by (see e.g. [Dijkstra, 2014](#); [Silva et al., 2016](#))

$$\epsilon_{\text{rec}}(T) = f_{\text{rec, A/B}}(T) n_e n_{\text{HII}} \alpha_{\text{A/B}}(T) E_{\text{Ly}\alpha}, \quad (1.1)$$

where  $\epsilon_{\text{rec}}$  is the Ly $\alpha$  luminosity density (in units of  $\text{erg s}^{-1} \text{cm}^{-3}$ ) as a function of the temperature  $T$  of the gas. In this equation,  $f_{\text{rec, A/B}}$  is the fraction of case-A or case-B recombinations, which ultimately result in the emission of a Ly $\alpha$  photon; and the free electron and H II number densities are denoted by  $n_e$  and  $n_{\text{HII}}$ , respectively. Case A and case B refer to the way in which recombination occurs. All possible recombinations of H II and a free electron are considered in case A; this includes any recombination event that take the resulting neutral hydrogen directly to the ground state ( $n = 1$ ). In case B, only recombinations resulting in hydrogen in an excited state are considered. The recombination coefficient given in unit volume per unit time ( $\text{cm}^3 \text{s}^{-1}$ ) for case-A or -B recombination is denoted by  $\alpha_{\text{A/B}}$ , and  $E_{\text{Ly}\alpha}$  is the energy of a Ly $\alpha$  photon.

Since direct recombinations into the ground state do not result in Ly $\alpha$  emission, an appropriately lower fraction that results in Ly $\alpha$  emission,  $f_{\text{rec, A}} < f_{\text{rec, B}}$ , has to be used if  $\alpha_A$  rather than  $\alpha_B$  is adopted as the recombination coefficient. The luminosity densities obtained for case A and case B are then equivalent, except for minor differences due to different fitting functions for the coefficients. We chose to fix our calculations to use case-B coefficients. We modelled  $f_{\text{rec, B}}$  using the relations given by [Cantalupo et al. \(2008\)](#) and [Dijkstra \(2014\)](#), whose fitting formulae are presented in Sect. A.1; for example at  $T = 10\,000\,\text{K}$ , this fraction is  $\sim 0.68$ . We elected to use case B because the model for  $f_{\text{rec, A}}(T)$  from [Dijkstra \(2014\)](#) is only valid up to  $\sim 10^{6.5}\,\text{K}$ , whereas gas temperatures in our simulations range up to  $\sim 10^7\,\text{K}$  (Sect. 1.3.2). For the recombination coefficient,  $\alpha_B(T)$ , we adopted the fitting function given in [Draine \(2011\)](#). The precise expressions can also be found in Sect. A.1.

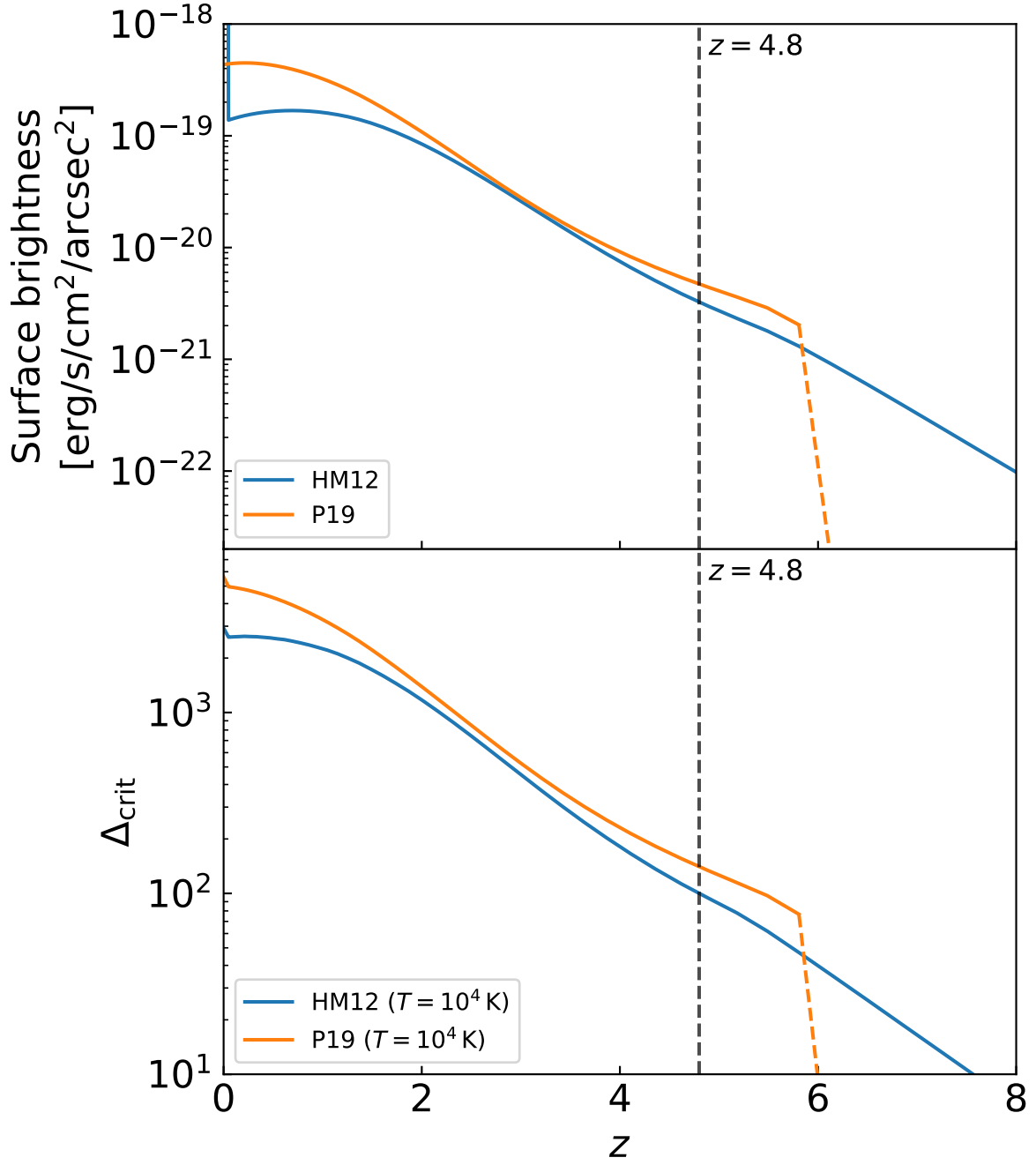


**Figure 1.1** Limiting SB and density quantities as a function of redshift. The top panel shows the limiting SB of Ly $\alpha$  in the mirror assumption, where 65% of ionising photons in the UVB are reprocessed into Ly $\alpha$  photons (see text for details) and the bottom panel shows the self-shielding critical density contrast  $\Delta_{\text{crit}}$ . The two different lines correspond to UVBs of Haardt & Madau (2012, , HM12) and Puchwein et al. (2019, , P19). Above  $z > 6$ , where the line is dashed, the P19 limits are not representative of ionised bubbles during patchy reionisation because the impact of neutral regions on the effective opacity to hydrogen ionising photons is included in the modelling (see P19) and hence a neutral hydrogen-weighted average over both neutral and ionised regions is computed in that model. A redshift of  $z = 4.8$  is highlighted by the dashed line.

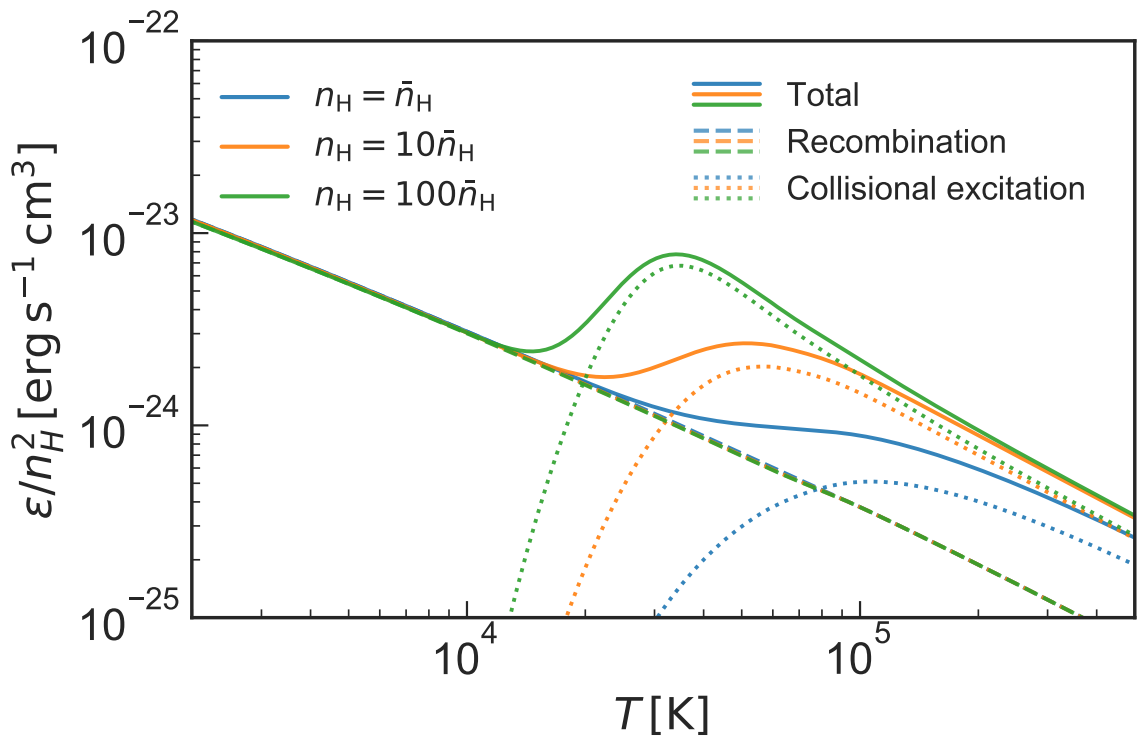


**Figure 1.2** Normalised emissivity (units are  $\text{erg s}^{-1} \text{cm}^3$ ) of the Ly $\alpha$  line in a cloud of primordial gas at  $z = 4.8$  as a result of recombination and collisional excitation processes as a function of temperature. There are three values of density, corresponding to overdensities of 1, 10, and 100, respectively; the mean cosmological hydrogen density corresponds to  $\bar{n}_H = 3.69 \cdot 10^{-5} \text{ cm}^{-3}$  at this redshift. The dashed and dotted lines show the contribution from just recombination and collisional excitation, respectively.

### Mirror limit

In the absence of local ionising UV sources and significant collisional ionisation, the recombination contribution to Ly $\alpha$  emission should not exceed the SB expected from fully absorbing the external UVB at the boundaries of self-shielded regions and fluorescently re-emitting a corresponding number of Ly $\alpha$  photons, hence ‘mirroring’ the external UVB. In calculating the recombination contribution to Ly $\alpha$  emission, unless mentioned otherwise, we employed this mirror assumption as an upper limit. More precisely, we placed an upper SB limit at the value expected when 65% of the ionising UVB is reprocessed as Ly $\alpha$  photons (e.g. [Gould & Weinberg, 1996](#); [Cantalupo et al., 2005](#)), equal to  $\text{SB} \simeq 3.29 \cdot 10^{-21} \text{ erg s}^{-1} \text{ cm}^{-2} \text{ arcsec}^{-2}$  for a [HM12](#) UVB at  $z = 4.8$ . Fig. 1.1 shows the mirror limit for two different UVBs from [HM12](#) and [Puchwein et al. \(2019\)](#); ; [P19](#) hereafter).

In reality, local ionising sources can boost the recombination emission above the mirror limit. Predicting this reliably is, however, extremely challenging because it involves modelling the ionising source populations in galaxies and the escape of ionising radiation from galaxies in full detail. Our recombination contribution to Ly $\alpha$  emission computed assuming the mirror limit should hence be considered only as a robust lower limit.

#### 1.2.2 Ly $\alpha$ emission through collisional excitation

##### Emissivity

For collisional excitation, the Ly $\alpha$  luminosity density has a similar form ([Scholz et al., 1990](#); [Scholz & Walters, 1991](#); [Dijkstra, 2014](#); [Silva et al., 2016](#)) given by

$$\epsilon_{\text{exc}}(T) = \gamma_{1s2p}(T) n_e n_{\text{HI}} E_{\text{Ly}\alpha}, \quad (1.2)$$

where  $n_{\text{HI}}$  denotes the number density of neutral hydrogen. We used the fitting functions for the collisional excitation coefficient  $\gamma_{1s2p}$  given by [Scholz et al. \(1990\)](#) and [Scholz & Walters \(1991\)](#). These fitting functions are valid in the temperature range  $2 \cdot 10^3 \text{ K} \leq T \leq 1 \cdot 10^8 \text{ K}$  (cf. Sect. A.1). The rates are not identical to those applied in the cosmological hydrodynamical simulation (see Sect. 1.2.4) as these are only given as an ensemble rather than for the specific  $2p \rightarrow 1s$  transition in which Ly $\alpha$  is emitted, but in the relevant temperature regime deviate so little that gas cooling equilibrium would not be appreciably violated.

##### Density limits

When computing the Ly $\alpha$  luminosity due to collisional excitation, we only considered gas well below the critical self-shielding density that is derived for the appropriate UVB (the [HM12](#) UVB, unless mentioned otherwise). We made use of the critical self-shielding hydrogen number density at  $T = 10^4 \text{ K}$  given in Eq. (13) in [Rahmati et al. \(2013\)](#) for this purpose (shown in the

bottom panel of Fig. 1.1 as a density contrast), but since this is based on the column density distribution of neutral hydrogen and for the purpose of absorption instead of emission processes, we chose a conservative default density threshold at half this value.

As shown in Fig. 1.1, the critical self-shielding overdensity is  $\Delta_{\text{crit}} \simeq 100$  at  $z = 4.8$ . We note that the density contrast,  $\Delta_{\text{crit}}$ , decreases towards higher redshift, meaning gas starts to be affected by self-shielding at a lower overdensity at higher redshift. By focussing on gas with densities below this critical threshold, we additionally ensure at this redshift that we do not enter the realm of gas densities strongly affected by the detailed baryonic physics of galaxy formation, such as feedback processes. For this reason, most of the results presented in this work are chosen to be at  $z = 4.8$  and are again a robust lower limit.

### 1.2.3 Emissivity

Fig. 1.2 shows the Ly $\alpha$  luminosity density at  $z = 4.8$  as a function of gas temperature for a gas of primordial composition at three different overdensities of 1, 10, and 100; the mean cosmological hydrogen density corresponds to  $\bar{n}_{\text{H}} = 3.69 \cdot 10^{-5} \text{ cm}^{-3}$  at this redshift. To derive the corresponding neutral hydrogen densities, we assume that hydrogen is in ionisation equilibrium with the HM12 UVB at  $z = 4.8$ . Fig. 1.2 also shows the recombination and collisional excitation components of the total Ly $\alpha$  emission. We find that collisional excitation dominates at high temperatures ( $T \gtrsim 2 \times 10^4 \text{ K}$ ).

### 1.2.4 Cosmological hydrodynamical simulation

To estimate the cosmological Ly $\alpha$  signal with the theoretical framework above, we made use of a simulation that builds upon the Sherwood simulation project (Bolton et al., 2017). The simulation is performed with the energy- and entropy-conserving TreePM smoothed particle hydrodynamics (SPH) code P-GADGET-3, which is an updated version of the publicly available GADGET-2 code (Springel et al., 2001; Springel, 2005). In this work, we used the same volume as in the 40–1024 simulation of the Sherwood suite. A periodic, cubic volume  $40 h^{-1} \text{ cMpc}$  long was simulated, employing a softening length of  $l_{\text{soft}} = 1.56 h^{-1} \text{ ckpc}$ , and  $1024^3$  dark matter and gas particles. Initial conditions were set up at redshift  $z = 99$  and the simulation was evolved down to  $z = 2$ . In order to speed up the simulation, star formation was simplified using the implementation of Viel et al. (2004) in P-GADGET-3; this method converts gas particles, with temperatures less than  $10^5 \text{ K}$  and densities of more than a thousand times the mean baryon density, to collisionless stars. This approximation is appropriate for this work as we do not consider the Ly $\alpha$  emission from the interstellar medium of galaxies, where a complex set of Ly $\alpha$  radiative transfer processes need to be accounted for. The ionisation and thermal state of the gas in the simulation is derived by solving for the ionisation fractions under the assumption of an equilibrium with the metagalactic UVB modelled according to HM12. A small modification to this UVB is applied at  $z < 3.4$  (see Bolton et al., 2017) to result in IGM temperatures that

agree with measurements by [Becker et al. \(2011\)](#). We also accounted for self-shielding of dense gas with an on-the-fly self-shielding prescription based on [Rahmati et al. \(2013\)](#). For each SPH particle and each time step, our modified P-GADGET-3 version computes a suppression factor for the UVB due to self-shielding that is based on the local gas density and uses the parameters given in the first line of table A1 of [Rahmati et al. \(2013\)](#). This factor is applied to photoionisation and heating rates before they are used in the chemistry and cooling solver. The solver follows photoionisation, collisional ionisation, recombination, and photoheating for gas of a primordial composition of hydrogen and helium, as well as further radiative cooling processes such as collisional excitation, Bremsstrahlung (see [Katz et al. 1996](#) for the relevant equations), and inverse Compton cooling off the cosmic microwave background ([Ikeuchi & Ostriker, 1986](#)). Metal enrichment and its effect on cooling rates are ignored. We identify dark matter halos in the output snapshots using a friends-of-friends algorithm.

### Narrowband images

When calculating the SB, we constructed mock narrowband images of the simulations, which are images that replicate the result of the process of capturing a narrowband image with a telescope, by taking a thin slice of the simulation in a direction parallel to a face of the simulation box and converting the emissivity in the simulation to arrive at a SB map; this is discussed in more detail below. The slice thickness corresponds to an observed wavelength width  $\Delta\lambda_{\text{obs}}$  of the narrowband. Its redshift range is given by

$$\Delta z = \frac{\Delta\lambda_{\text{obs}}}{\lambda_{\text{Ly}\alpha}}, \quad (1.3)$$

which corresponds to a comoving distance

$$\Delta d = \frac{c}{H_0} \int_z^{z+\Delta z} \frac{1}{\sqrt{\Omega_m (1+z')^3 + \Omega_\Lambda}} dz'. \quad (1.4)$$

As a reference value for the observed narrowband width, we used  $\Delta\lambda_{\text{obs}} = 8.75$ , the median value of narrowband widths in the study by [Wisotzki et al. \(2016\)](#); this corresponds to 7 spectral pixels of the VLT/MUSE instrument (Sect. 1.3.3 describes narrowband imaging in more detail). At a redshift of  $z = 4.8$ , this results in a comoving line-of-sight distance of  $\sim 2.7 h^{-1}$  cMpc (see Sect. 1.2.2 for an elaboration on the choice of this particular redshift), corresponding to only a small fraction of the total size of the simulation volume. We discuss the effect of varying the narrowband width on the detectability of Ly $\alpha$  further in Sect. 1.3.4.

Using the temperature, density, and ionisation fraction, an emissivity for each individual simulation particle within the narrowband slice can be computed. These emissivities were then converted to luminosities and projected onto a two-dimensional plane using the SPH kernel

of the simulation particles, turning them into a luminosity per unit area, which in turn is converted to a SB.

### Radiative transfer effects

In the predictions made in this work, Ly $\alpha$  propagation is always treated in the optically thin limit. For the constructed mock narrowband images, it is assumed that Ly $\alpha$  photons are emitted in an isotropic manner and reach the observer without any scattering. The exact effects that scattering would have are difficult to accurately predict given for example that the effects of dust are poorly constrained. But it is expected that for the filamentary IGM, the difference between our simulations and a model with a physically accurate treatment of radiative transfer is mostly influenced by two competing effects. First, there might be a broadening of the filamentary structure due to scattering in the nearby IGM, causing the signal to become fainter. Second, however, filaments may also be illuminated by Ly $\alpha$  radiation coming from nearby dense structures (where additional radiation is likely to be produced in galaxies) that is scattered in the filament, which would cause the filaments to appear brighter. Simulations including radiative transfer show a mixture of these two effects, where the SB of filaments generally is not affected much or is even boosted (private communication, Weinberger, 2019). As the effects of radiative transfer on this work are expected to be moderate, they are assumed not to affect our main findings in a major way; a more detailed discussion on the optical depth of Ly $\alpha$  is included in Sect. A.2. Future work can detail the precise effects of radiative transfer.

We limit the maximum SB from recombinations to what is expected from purely reprocessing or mirroring the UVB at the boundaries of self-shielded regions (see Sect. 1.2.1). This also mitigates the effect where the absence of radiative transfer can bias the SB upwards in cases in which a sightline crosses several dense structures. In reality, however, with the presence of local ionising sources in such dense regions, an amplification with respect to the reprocessed UVB would likely be present as well. This is also suggested by a comparison of our simulation with a post-processing radiative transfer simulation of the same volume using a local source population similar to that described in Kulkarni et al. (2019a). Still, even with an accurate treatment of radiative transfer, the precise effects in the densest regions may rely considerably on the exact baryonic feedback mechanisms that are operating in these regions.

## 1.3 Results

### 1.3.1 Luminosity density

Fig. 1.3 shows the redshift evolution of the comoving Ly $\alpha$  luminosity density in our simulation down to  $z = 2$ . The total luminosity of gas within the entire simulation at densities below half the critical self-shielding density, corresponding to an overdensity  $\rho/\bar{\rho} \lesssim 50$  at  $z = 4.8$  (see

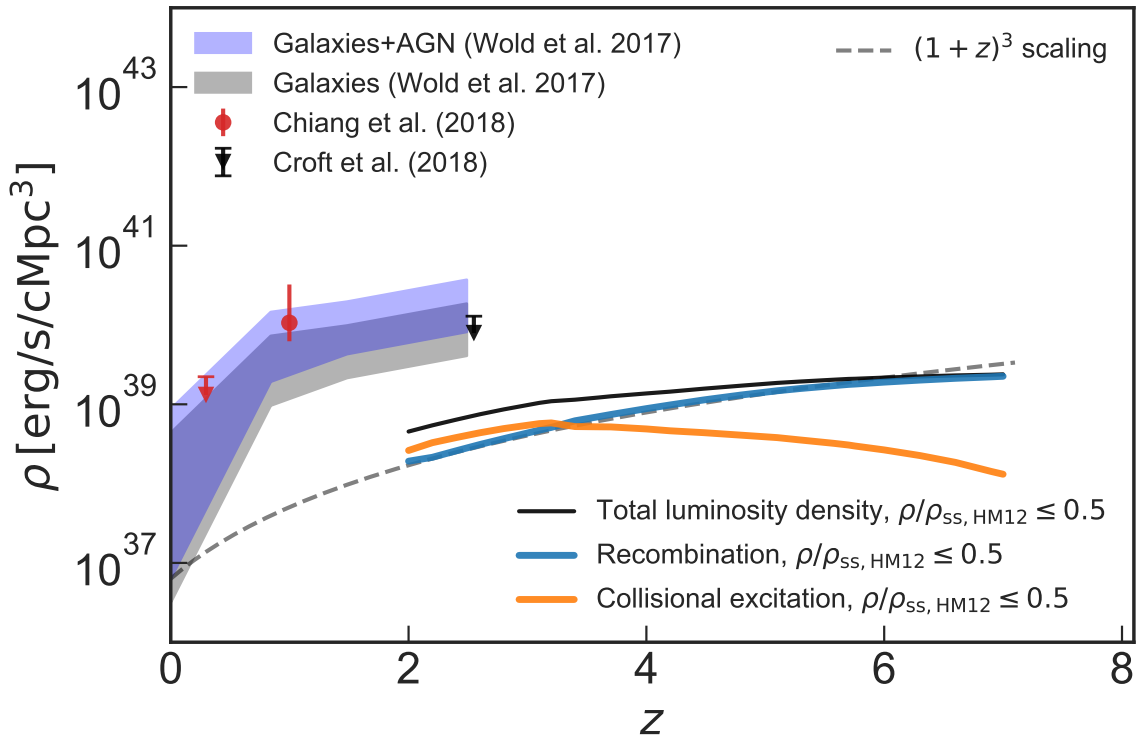


**Figure 1.3** Redshift evolution of the comoving Ly $\alpha$  luminosity density. The blue and orange lines show the results for recombination and collisional excitation emission for gas at densities below half the critical self-shielding density roughly corresponding to the IGM at an overdensity  $\Delta \equiv \rho/\bar{\rho} \lesssim 50$  at  $z = 4.8$  (see Sect. 1.2.2). The black line shows the total luminosity density for gas below this density threshold; all these follow from the simulation run with a box size of  $40 h^{-1}$  cMpc and resolution of  $2 \times 1024^3$  particles (see Sect. 1.2.4 for more details on the simulation). Observational measurements at low redshift ( $z < 3$ ), as presented in Chiang et al. (2019), have been included as a reference. These consist of luminosity densities of just galaxies and the contribution of galaxies and AGN (shown as the grey and blue shaded areas, respectively) inferred by Chiang et al. (2019) from the intrinsic luminosity density presented in Wold et al. (2017); the measurement and upper limit from Chiang et al. (2019) are shown in red, and the upper limit from Croft et al. (2018) (converted to a luminosity density by Chiang et al., 2019) is shown in black (see text for details). Data points are shown as circles, upper limits as downward triangles. Also shown is the  $(1+z)^3$  scaling relation for recombination emission discussed in the text.

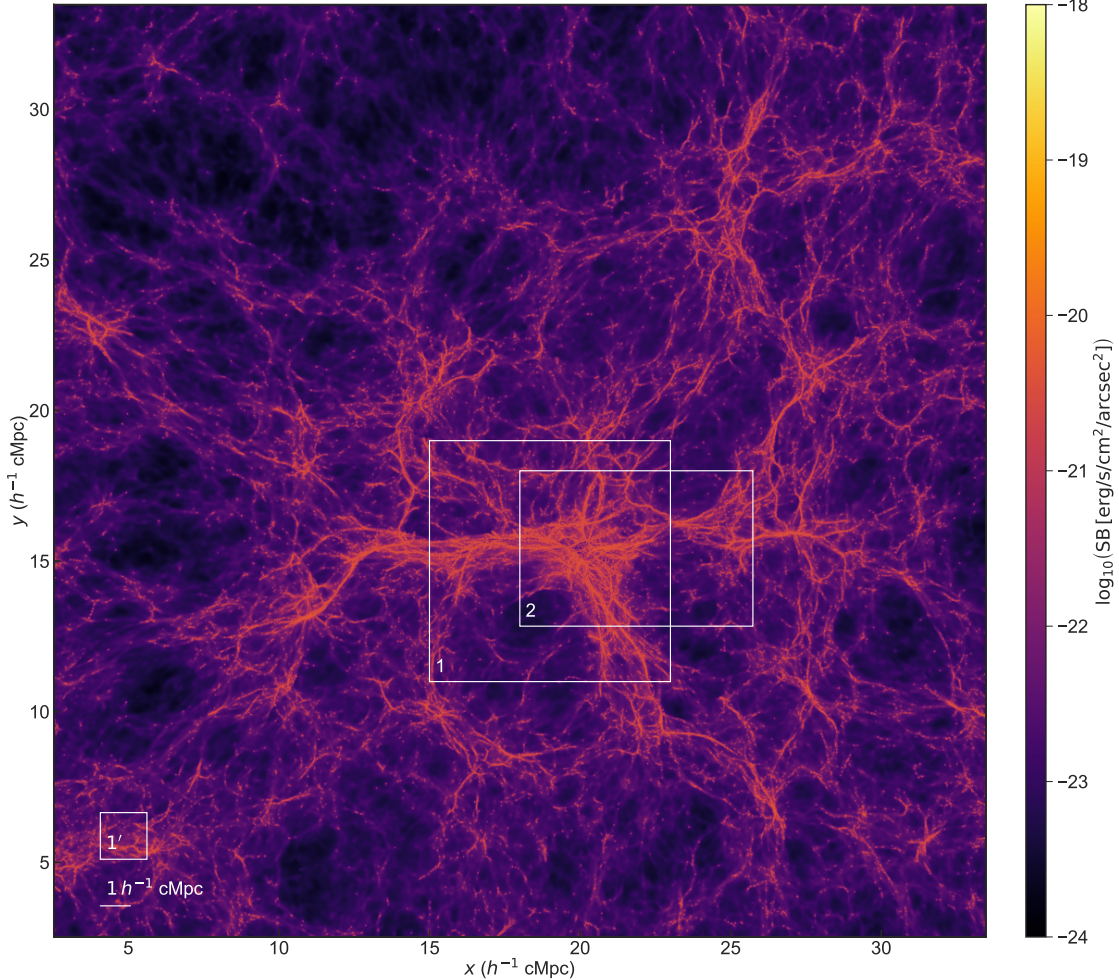


**Figure 1.4** Ly $\alpha$  SB resulting from the combination of recombination emission (of all gas in the simulation) below the mirror limit and collisional excitation of gas below half the critical self-shielding density, covering an area of  $20 \times 20$  arcmin $^2$ , or  $31.0 \times 31.0 h^{-2}$  cMpc $^2$ , in a narrowband with  $\Delta\lambda_{\text{obs}} = 8.75$  (corresponding to  $\sim 2.7 h^{-1}$  cMpc) in a simulation snapshot at  $z = 4.8$ . The images are made by the projection method (Sect. 1.2.4) onto a pixel grid of  $6000 \times 6000$ ; this is the same pixel size as MUSE, making this image the equivalent of a mosaic of  $20 \times 20$  MUSE pointings (more details on MUSE follow in Sect. 1.3.3). Regions 1 and 2, indicated by the white rectangles, will be studied in more detail later. Also shown in the bottom left corner are the scales of the MUSE FOV ( $1 \times 1$  arcmin $^2$ ) and  $1 h^{-1}$  cMpc.

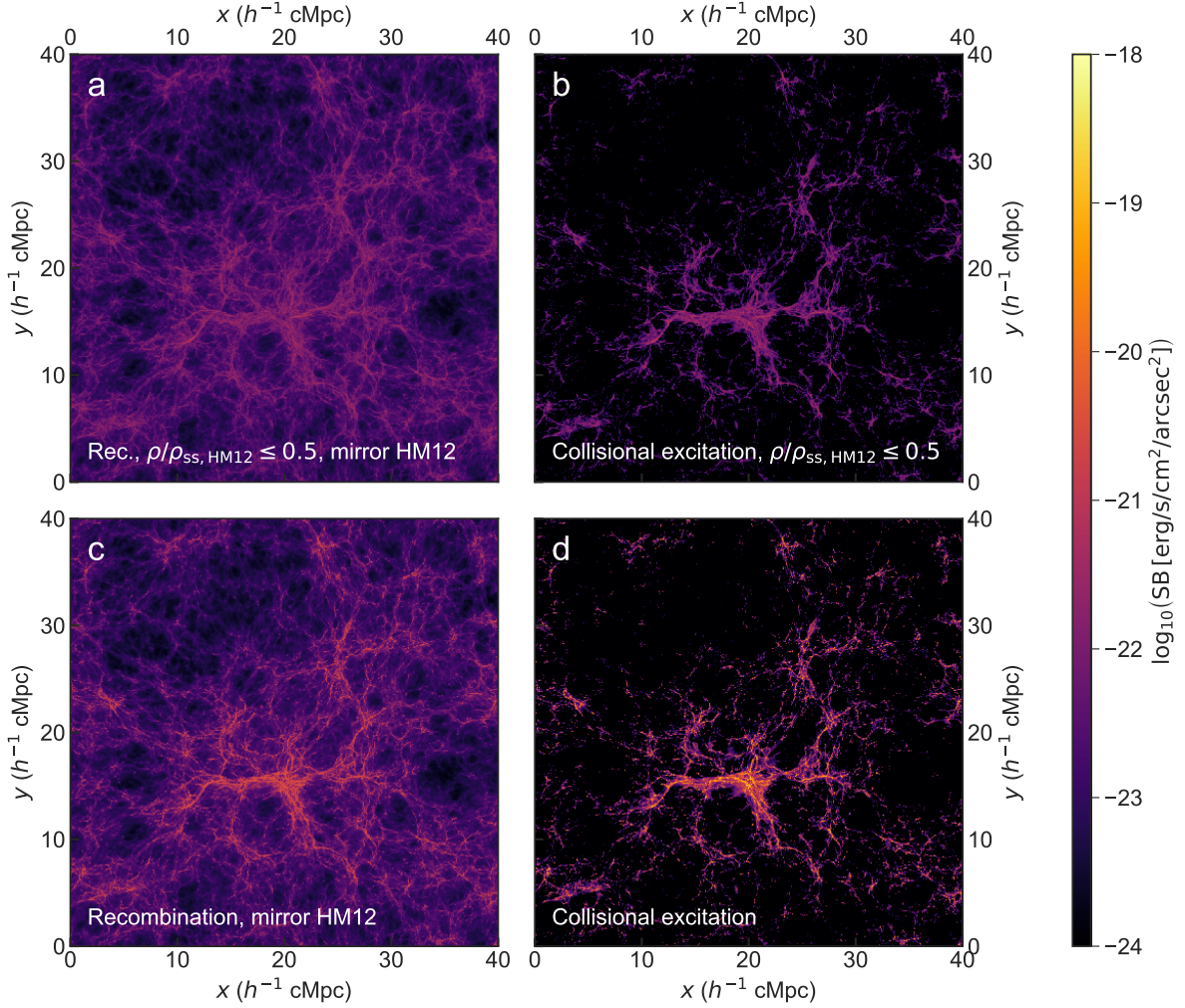


**Figure 1.5** Ly $\alpha$  SB of recombination (panel **a**) and collisional excitation (panel **b**) processes in a simulation snapshot at  $z = 4.8$ , for the gas at densities below half the critical self-shielding density in a narrowband with  $\Delta\lambda_{\text{obs}} = 8.75$ , or  $\sim 2.7 h^{-1} \text{ cMpc}$ ; the projections are made with pixel grid sizes of  $1024 \times 1024$ . These images show the entire (two-dimensional) spatial extent of the simulation,  $40 \times 40 h^{-2} \text{ cMpc}^2$  ( $25.8 \times 25.8 \text{ arcmin}^2$ ). Panels **c** and **d** show the same maps, but without a density cut-off.

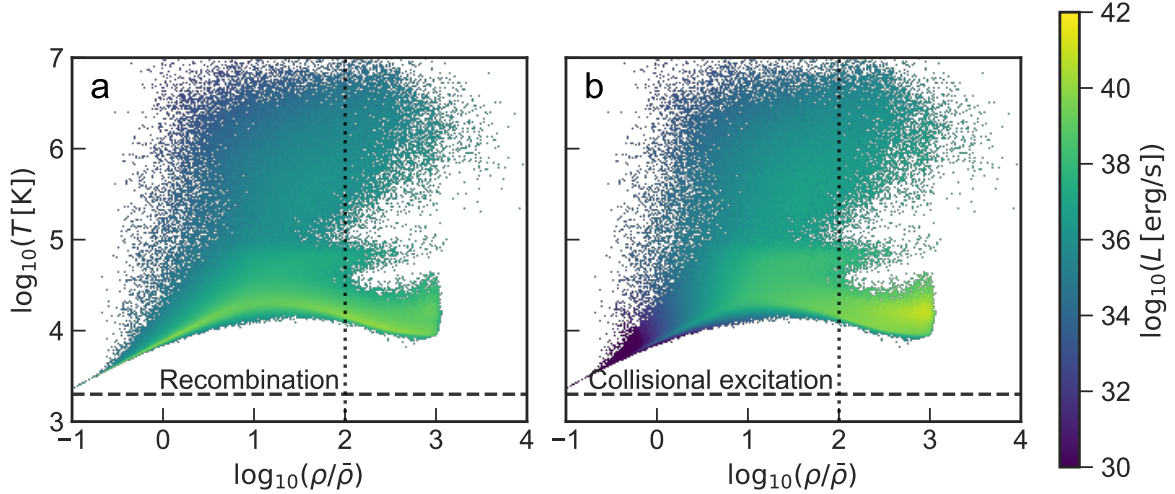


**Figure 1.6** Histogram of Ly $\alpha$  luminosities of recombination (panel **a**) and collisional excitation (panel **b**) processes in the same region as shown in Fig. 1.5 (a narrowband with  $\Delta\lambda_{\text{obs}} = 8.75$ , equivalent to  $\sim 2.7 h^{-1} \text{ cMpc}$ ) in a simulation snapshot at  $z = 4.8$  in phase space. The colour represents the total luminosity in the simulation per histogram bin. The horizontal dashed line corresponds to the lower limit above which the fitting function of Scholz et al. (1990) and Scholz & Walters (1991) for collisionally excited Ly $\alpha$  emission is valid; the upper limit lies above the plotted range. The vertical dotted line shows the critical self-shielding density threshold at this redshift for the HM12 UVB (from Eq. (13) in Rahmati et al., 2013). Densities above the threshold are also more strongly affected by modelling uncertainties.

Sect. 1.2.2), roughly corresponding to the IGM, is computed. This is also done separately for the recombination and collisional excitation contributions. We then divide by the (comoving) simulation volume to convert the luminosity to a comoving luminosity density.

Observational measurements at low redshift ( $z < 3$ ), as compiled by Chiang et al. (2019), are included as reference. We note that these data points should not be directly compared to our predictions as we consider only emission from the low-density gas in the IGM. The data consist of estimates of the luminosity density of Ly $\alpha$  emission from galaxies and AGN inferred by Wold et al. (2017) based on a flux-limited sample of LAEs from GALEX data and scaling the H $\alpha$  galaxy luminosity function measurements (Sobral et al., 2013) out to  $z = 2$ . Chiang et al. (2019) obtain a measurement on the total Ly $\alpha$  luminosity density from galaxies and AGN as well as an upper limit on the diffuse IGM contribution by cross-correlating the GALEX UV intensity maps with spectroscopic objects in SDSS. A comparison of the measurements from Chiang et al. (2019) and Wold et al. (2017) indicates that, at least at  $z \lesssim 1$ , most Ly $\alpha$  emission originates in galaxies and AGN. The upper limit from Croft et al. (2018, ; converted to a luminosity density by Chiang et al. 2019) is shown in black in Fig. 1.3. Croft et al. (2018) fit model spectra to luminous red galaxies in BOSS and cross-correlate the residual Ly $\alpha$  emission with the Ly $\alpha$  forest in BOSS quasars to obtain the upper limit from a non-detection shown in

Fig. 1.3. As such, this procedure places a limit on the component of diffuse Ly $\alpha$  emission that correlates with the matter distribution (Croft et al., 2018).<sup>1</sup>

Going from redshift  $z = 2$  to  $z = 7$ , the comoving Ly $\alpha$  luminosity density increases by just under an order of magnitude (see Sect. A.3 for a further discussion of the redshift evolution of SB). As can be seen in the figure, this is mostly due to the increase in recombination emission. Under the simple assumption that the emissivity is produced at a fixed overdensity its emissivity increases like the square of the mean density, which would correspond to a scaling of

$$\begin{aligned}\epsilon_{\text{rec}} &\sim \Delta^2(1+z)^6 \text{ (physical luminosity density) or} \\ \epsilon_{\text{rec}} &\sim \Delta^2(1+z)^3 \text{ (comoving luminosity density),}\end{aligned}\quad (1.5)$$

where  $\epsilon_{\text{rec}}$  is the recombination emissivity and  $\Delta \equiv \rho/\bar{\rho}$  the overdensity. As shown by the dashed line in Fig. 1.3, the simple scaling for recombination emission in Eq. (1.5) explains the simulated luminosity density very well at all redshifts shown.

For collisional excitation, there should be two relevant effects: in the optically thin limit, the neutral fraction in ionisation equilibrium increases proportional to the density, hence  $n_{\text{HI}} \sim n_{\text{H}}^2$ ; consequently, the emissivity scales as  $\epsilon_{\text{exc}} \sim n_{\text{HI}}n_{\text{e}} \sim n_{\text{H}}^3$ . If the emission were again produced at fixed overdensity, and if there is little evolution in the photoionisation rate, this would hence scale as

$$\begin{aligned}\epsilon_{\text{rec}} &\sim \Delta^3(1+z)^9 \text{ (physical luminosity density) or} \\ \epsilon_{\text{rec}} &\sim \Delta^3(1+z)^6 \text{ (comoving luminosity density),}\end{aligned}\quad (1.6)$$

where  $\epsilon_{\text{exc}}$  is the emissivity from collisional excitation. However, collisional excitation does not follow the predicted  $(1+z)^6$  scaling in Eq. (1.6) (and hence is not shown), even decreasing with redshift at  $z \gtrsim 3$ . This suggests that it is dominated by emission near the critical self-shielding density (see also Sect. 1.3.2) and is hence more strongly affected by the density limit at half the critical self-shielding density, which decreases with increasing redshift more strongly than the mean density (i.e. the critical self-shielding overdensity decreases towards higher redshift, see Sect. 1.2.2). Still, we note that, depending on the precise distribution of self-shielded regions, which is dictated by local ionising sources on a small scale, collisional excitation from dense gas could account for an additional increase of the comoving luminosity density that surpasses the cosmic SB dimming effect, which itself scales as  $(1+z)^4$ .

---

<sup>1</sup>An additional measurement, arising from a cross-correlation with BOSS quasars, is restricted to scales within  $15 h^{-1} \text{ cMpc}$  of a quasar (equivalent to only  $\sim 3\%$  of space, see Croft et al., 2018) and is therefore not included as a global luminosity density in this work.

### 1.3.2 Surface brightness maps

Fig. 1.4 shows a SB map that is the combination of recombination emission (of all gas in the simulation) below the mirror limit and collisional excitation of gas below half the critical self-shielding density in a simulation snapshot at  $z = 4.8$ , for a narrowband with  $\Delta\lambda_{\text{obs}} = 8.75$  (at this redshift coinciding with a thickness of the slice of  $\sim 2.7 h^{-1} \text{ cMpc}$ ). The map shows a region corresponding to  $20 \times 20 \text{ arcmin}^2$ . Also shown in the bottom left corner is the size of the MUSE field of view (FOV;  $1 \times 1 \text{ arcmin}^2$  – see Sect. 1.3.3 for more details). Regions 1 and 2, indicated by the white rectangles, will be studied in more detail later. The values of the SB for this narrowband width are of the order of  $\text{SB} \lesssim 10^{-23} \text{ erg s}^{-1} \text{ cm}^{-2} \text{ arcsec}^{-2}$  for the void regions, increasing to typically  $\sim 10^{-21} \text{ erg s}^{-1} \text{ cm}^{-2} \text{ arcsec}^{-2}$  for the IGM filaments. The denser regions have intensity peaks that typically show SB values of  $\sim 10^{-20} \text{ erg s}^{-1} \text{ cm}^{-2} \text{ arcsec}^{-2}$ .

Fig. 1.5 shows the same narrowband slice as in Fig. 1.4 (now for the full spatial extent of the simulation box,  $40 \times 40 h^{-2} \text{ cMpc}^2$  or  $25.8 \times 25.8 \text{ arcmin}^2$ ) split into contributions from recombination and collisional excitation processes in the gas. These maps were all made by projection onto a grid of  $1024 \times 1024$  pixels. As before, a narrowband slice with  $\Delta\lambda_{\text{obs}} = 8.75$  ( $\sim 2.7 h^{-1} \text{ cMpc}$ ) was chosen. Panels a and b show gas at densities below half the critical self-shielding density, while panels c and d show all gas. The mirror limit was applied to both panels showing recombination emission (a and c). In this large-scale narrowband image, the total luminosity of recombination processes below half the critical self-shielding density – that is the total in panel a before imposing the mirror limit (although no pixels are in fact above the limit in this panel) – is  $\sim 1.75 \cdot 10^{43} \text{ erg s}^{-1}$ . For collisional excitation (the total in panel b), this is  $\sim 5.45 \cdot 10^{42} \text{ erg s}^{-1}$ . Including all gas, the total luminosity is  $\sim 5.02 \cdot 10^{43} \text{ erg s}^{-1}$  for recombination (panel c), again before imposing the mirror limit (now only 0.37% of pixels are above the limit); the total value is  $\sim 2.21 \cdot 10^{44} \text{ erg s}^{-1}$  for collisional excitations (panel d). We note that while collisional excitations dominate over recombinations at high densities, the two processes contribute more equally at the lower densities prevalent in large-scale-structure filaments; recombination prevails slightly over collisional excitation below our adopted threshold. Moreover, gas near or somewhat above the critical self-shielding density contributes significantly to the maximum SB that is reached for both channels. We conclude that the recombination prediction including all gas while the mirror limit is imposed should yield at least a robust lower limit, while the collisional excitation prediction for gas at higher densities is more uncertain, thereby motivating our conservative density limit (Sect. 1.2.2).

While overall these SB maps exhibit the same structure as Fig. 1.4, the spatial distribution of emission coming from collisional and recombination processes is different. The degree of clustering in the emission is lower for the emission produced by recombination processes than it is for the contribution of collisional excitation. Recombination and collisional excitation depend differently on temperature and density, as discussed in Sect. 1.3.1. In particular, at fixed temperature and photoionisation rate, recombinations are proportional to the square of

the density,  $\sim \rho^2$ , while in ionisation equilibrium collisional excitations are proportional to  $\sim \rho^3$ . As a consequence, recombinations are more equally spread across the volume, while collisional excitations are clearly more important at higher densities, thus reflecting the filamentary structure of the cosmic web better and leaving darker voids in between. To understand this in more detail, we now turn to the phase-space distribution of the gas in the simulation.

In Fig. 1.6, the luminosity in the simulation is shown at the same redshift and the same region as in Fig. 1.5 (also in the identical narrowband slice of  $\Delta\lambda_{\text{obs}} = 8.75$ , or  $\sim 2.7 h^{-1} \text{ cMpc}$ ), now as a luminosity-weighted, two-dimensional histogram in temperature and density. This illustrates what was discussed in Sect. 1.3.1 and shown in Fig. 1.5: collisional excitation is not effective at lower densities and the most luminous gas particles are located in the upper part of the very high-density cooling branch. Recombination emission, on the other hand, exhibits luminosities that are more comparable at lower and higher densities.

From the phase-space distribution in Fig. 1.6, it is clear that very little gas has temperatures outside of the temperature range of  $2 \cdot 10^3 \text{ K} \leq T \leq 1 \cdot 10^8 \text{ K}$ , for which our fitting function for collisionally excited Ly $\alpha$  is valid. The lower limit of this fitting function is indicated by the horizontal dashed line; the upper limit lies above the plotted range and almost all of the gas in the simulation.<sup>2</sup> The contribution from gas outside of this temperature range will be very small and we thus neglect it here.

The vertical dotted line shows the critical self-shielding density threshold at this redshift for the HM12 UVB (from Eq. (13) in Rahmati et al., 2013), illustrating the limiting density below which gas is not strongly affected by the details of modelling self-shielding.

### 1.3.3 Observing facilities

In Table 1.1, an overview of a selection of current and future instruments that could potentially detect Ly $\alpha$  emission from IGM filaments is shown along with their wavelength and redshift range, FOV, and resolving power ( $R$ ). Most ground- and space-based instruments that may be considered for detection of the diffuse IGM naturally observe in the visible spectrum and the ultraviolet, respectively, given the limitations of ground-based observations owing to absorption by Earth’s atmosphere. This necessarily restricts the redshift range in which these instruments could observe Ly $\alpha$ . For ground-based observations, the typical redshift is  $z \gtrsim 2.5$ , whereas space-based telescopes observing in the UV can detect Ly $\alpha$  at lower redshifts. In principle, satellites carrying UV detectors could observe Ly $\alpha$  from  $z \sim 0$  up to about  $z \sim 1.5$ .

IFU spectrographs arguably have the best instrument design for directly detecting emission from the cosmic web, owing to the flexibility in extracting pseudo-narrowband images over a wide range of bandwidths and central wavelengths and thereby resolving structures both spatially and spectrally over a large cosmic volume at once. The typical narrowband width extracted from IFU spectrographs to observe Ly $\alpha$  emission is  $< 10$  (e.g. Wisotzki et al., 2016,

---

<sup>2</sup>This is the case for the entire relevant redshift range.

## Prospects for observing the low-density cosmic web in Lyman- $\alpha$ emission

---

**Table 1.1** Overview of a selection of current and future instruments that might be most promising for detecting IGM filaments. Fields left blank indicate currently unknown or undecided values. All current instruments presented are IFU spectrographs, upcoming and/or proposed instruments include several IFU spectrographs and space telescopes (two UV satellites and one IR spectrophotometer). Future experiments are in the development stage, unless marked with an asterisk.

Name	Wavelength range $\lambda$ (Å)	Redshift range $z_{\text{Ly}\alpha}$	Field of view	Resolution
<i>Current IFU instrumentation</i>				
KCWI-Blue (Keck)	3500-5600	1.9-3.6	$20 \times 33 \text{ arcsec}^2$	1000-2000
MUSE (VLT)	4650-9300	2.8-6.7	$1 \times 1 \text{ arcmin}^2$	1770-2000
KMOS (VLT)	8000-25000	5.6-19.6	$65 \times 43 \text{ arcsec}$	2000-2500
OSIRIS (Keck)	10000-24500	7.2-19.1	$4.8 \times 6.4 \text{ arcsec}^2$	2000-2500
SINFONI (VLT)	11000-24500	8.0-19.1	$8 \times 8 \text{ arcsec}^2$	2000-2500
<i>Upcoming IFU instrumentation</i>				
KCRM (KCWI-Red, Keck)	5300-10500	3.4-7.6	$20 \times 33 \text{ arcsec}^2$	1000-2000
HARMONI (ELT)	4700-24500	2.9-19.1	$6.4 \times 9.1 \text{ arcsec}^2$	3000-4000
BlueMUSE (VLT)	3500-6000	1.9-3.9	$1.4 \times 1.4 \text{ arcmin}^2$	$\sim 3000$
<i>Upcoming and/or proposed space missions</i>				
SPHEREx*	7500-50000	5.2-40.1	$3.5 \times 11.3 \text{ deg}^2$	41-100
MESSIER*	$\sim 2000$ -7000	$\sim 0.5$ -4	$2 \times 2 \text{ deg}^2$	...
WSO-UV	1150-3200	$\sim 0$ -1.5	$70 \times 75 \text{ arcsec}^2$	$\sim 5$

2018). This value is almost an order of magnitude smaller than that obtained from photometric narrowband imaging with typical bandwidths of  $\sim 80$ -100 (Steidel et al., 2011; Ouchi et al., 2018). This significantly improves the contrast of IFU emission line maps for observations limited by sky noise. Despite the limited contrast for individual images, photometric narrowband studies still have detected large-scale Ly $\alpha$  emission in stacking analyses (e.g. Steidel et al., 2011; Matsuda et al., 2012; Kakuma et al., 2019), enabled by the wide FOV and large number of sources collected by such cameras. In particular, the recently installed Hyper Suprime-Cam on Subaru is currently obtaining  $26 \text{ deg}^2$  narrowband imaging from redshift  $z = 2.2$ -6.6 as part of the Hyper Suprime-Cam Subaru Strategic Program (e.g. Ouchi et al., 2018). However, for this work, we focus on instruments that are most likely to obtain individual detections of Ly $\alpha$  emission from the cosmic web. Before the appearance of IFU imaging, another spectroscopic method used was long-slit spectroscopy (as in e.g. Rauch et al., 2008). But with the arrival of integral field spectroscopy, the volume probed by deep observations targeting Ly $\alpha$  emission could be dramatically increased, rendering long-slit spectroscopy a non-competitive alternative for this purpose.

The Very Large Telescope (VLT) has the widest range of IFU spectrographs. The current near-IR instruments at this facility are the Spectrograph for INtegral Field Observations in the Near Infrared (SINFONI, see Eisenhauer et al., 2003; Bonnet et al., 2004) and the K-band Multi Object Spectrograph (KMOS, see Sharples et al., 2013). Owing to their spectral range,

### 1.3 Results

---

these instruments are only able to observe Ly $\alpha$  at very high redshifts, respectively,  $z > 8.0$  and  $z > 5.6$ , where the partly neutral IGM is expected to absorb most Ly $\alpha$  emission. The Multi Unit Spectroscopic Explorer (MUSE), an IFU spectrograph operating in the visible wavelength range (see [Bacon et al., 2010](#)), was most recently installed on the VLT. The combination of its relatively large FOV ( $1 \times 1 \text{ arcmin}^2$ ) and spectral coverage (4650-9300 ), while maintaining good spectral resolution (ranging between 1770-3590), currently makes this instrument one of the most promising candidates for the purpose of imaging the cosmic web in Ly $\alpha$ . BlueMUSE ([Richard et al., 2019](#)) is a proposed second MUSE instrument that will be optimised for the blue end of the visible wavelength range. Future instruments at the successor of the VLT, the ELT, include the High Angular Resolution Monolithic Optical and Near-infrared Integral field spectrograph (HARMONI, see [Thatte et al., 2014](#)), which is expected to be operational in 2025.

The blue channel of the Keck Cosmic Web Imager (KCWI, see [Morrissey et al., 2018](#)) is an instrument similar to VLT/MUSE at the Keck II telescope. This instrument offers a slightly better spectral sampling, although the FOV and spatial resolution are smaller and lower ( $20 \times 33 \text{ arcsec}^2$  and  $1.4 \text{ arcsec}$ ), respectively. However, since it has only become operational in 2018, no deep-field imaging such as the MUSE observations of the *Hubble* Deep Field South and *Hubble* Ultra-Deep Field ([Bacon et al., 2015, 2017](#)) has been released publicly yet. The red channel to KCWI, the Keck Cosmic Reionization Mapper (KCRM), is currently under construction and will complement the blue channel to cover the full wavelength range of 3500-10500 ( $3.4 < z_{\text{Ly}\alpha} < 7.6$ ). Similar to SINFONI on the VLT, Keck currently has a near-infrared IFU spectrograph, OSIRIS. This instrument has a small FOV that can target Ly $\alpha$  only above  $z > 7.2$ , where the considerably neutral IGM is expected to absorb most emission.

For completeness, we also mention several promising space-based experiments: the World Space Observatory-Ultraviolet (WSO-UV, see [Sachkov et al., 2018](#)), and MESSIER ([Valls-Gabaud & MESSIER Collaboration, 2017](#)), two proposed UV satellites. These satellites are proposed to have large FOVs and high sensitivities, but are limited to the lower redshift range ( $z < 1.5$ ). In this work, we instead focus our attention on the high-redshift regime ( $z > 3$ ). In February 2019, SPHEREx ([Doré et al., 2018](#)) was selected as the next medium-class explorer mission by NASA and is targeted for launch in 2023. The SPHEREx mission will survey the entire sky with a spectrophotometer at very low spectral resolution, sensitive to diffuse Ly $\alpha$  emission at  $z > 5.2$ .

Out of the current instruments, MUSE arguably offers the best compromise of resolution, spectral coverage, and volume surveyed. The combination of its FOV of  $1 \times 1 \text{ arcmin}^2$  and spectral resolution make it a promising instrument to observe the cosmic web in Ly $\alpha$  emission. As a representative example of what has already been achieved, we now discuss in more detail the MUSE *Hubble* Deep Field South (HDFS; see [Bacon et al., 2015](#)). This is a 27h integration of the HDFS, reaching a  $1\sigma$  SB limit of  $1 \cdot 10^{-19} \text{ erg s}^{-1} \text{ cm}^{-2} \text{ arcsec}^{-2}$  for emission lines. In Fig. 1.7, we show the wavelength dependence of the inferred noise from the MUSE HDFS in

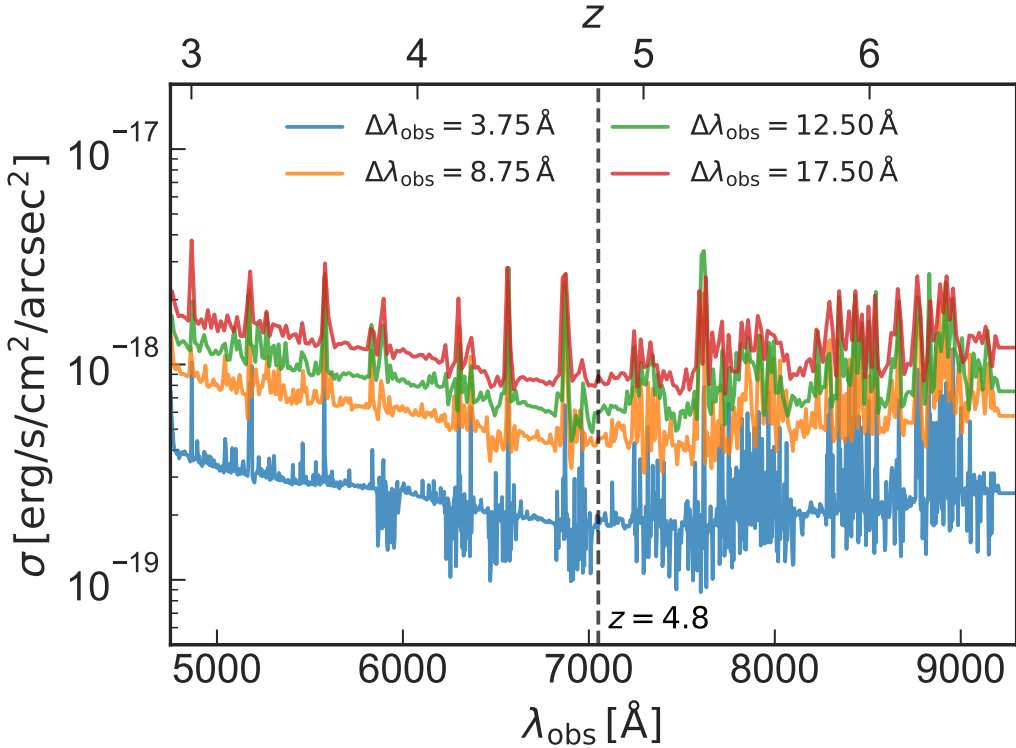


**Figure 1.7** Inferred noise in the MUSE HDFS observation as a function of observed wavelength or redshift for different pseudo-narrowband widths:  $\Delta\lambda_{\text{obs}} = 3.75$ ,  $\Delta\lambda_{\text{obs}} = 8.75$ ,  $\Delta\lambda_{\text{obs}} = 12.50$ , and  $\Delta\lambda_{\text{obs}} = 17.50$ . Skyline result in increased noise in some spectral ranges. The vertical dashed line indicates the position of Ly $\alpha$  at  $z = 4.8$ , which is located in a spectral window with lower noise. The throughput of MUSE is at its maximum of  $\sim 40\%$  at  $\sim 7200$  (e.g. [Richard et al., 2019](#)).

pseudo-narrowbands of different widths for reference. We discuss the consideration of different narrowband widths in more detail in Sect. 1.3.4.

With MUSE, the Ly $\alpha$  emission can be observed over the redshift range of 2.8–6.7 (see Table 1.1). Hereafter, a redshift of  $z = 4.8$  is specifically chosen for a more detailed study of our simulations. As already hinted at in Fig. 1.3, the diffuse gas in the IGM appears to be denser and potentially intrinsically more luminous in Ly $\alpha$  at higher redshifts; however, there are negating effects imposed by self-shielding because the critical self-shielding overdensity and the mirror limit steadily decrease towards higher redshifts (Sects. 1.2.1 and 1.2.2). We chose a redshift of 4.8 that seems to offer a reasonable compromise between these two effects, while also ensuring the results are not significantly affected by the details of feedback (Sect. 1.2.2). Finally, there is an additional component of emission from filaments due to halos and galaxies embedded within these filaments, the exact redshift dependence of which is difficult to predict.

The following section describes more fully the outlook on observations of primarily the diffuse gas with a MUSE-like instrument. Specifically, we focus on such a wide-field integral field spectrograph on an ELT-class telescope to explore the most far-reaching observational prospects in the near future, discussing sensitivity limits, the overall redshift evolution, and optimal observing strategies.

To allow for a more realistic comparison between simulations and observations, some of the SB images hereafter (Figs. 1.9 and 1.10) are convolved with a Gaussian point spread function (PSF), to mimic the effect of seeing. The PSF full width at half maximum (FWHM) is chosen to be 0.75 arcsec, corresponding to the most conservative estimate for the MUSE HDFS ([Bacon et al., 2015](#)). In addition, these figures include noise that is added to the signal predicted from the simulations.

### 1.3.4 Simulated observations

#### Cosmic variance and narrowband widths

Before we look in more detail at observational strategies, we introduce two indicators of overdensity in the ‘observed’ simulation volume. The reason we introduce these specific characterisations of environment is to provide a quantitative way to distinguish different regions according to the level of their overall overdensity as could be characterised observationally. The first criterium to characterise environment, the baryonic overdensity,  $\Delta_{\text{baryon}}$ , is computed by the ratio of baryonic density in the relevant region and the mean baryonic density at the redshift of the simulation. As a second criterion, we use the halo overdensity,  $\Delta_{\text{halo}}$ , which is similar but instead of baryons uses halos with halo mass  $M_h > 10^{9.5} M_\odot$ : the amount of mass contained in these halos divided by the simulated (sub)volume as a fraction of their mean density, which is found by dividing the total mass of all halos with  $M_h > 10^{9.5} M_\odot$  in the simulation box by its total volume.<sup>3</sup> This particular mass cut-off has been chosen as this is near the resolution limit of the simulation.

Now turning our attention to a MUSE-like instrument specifically, Fig. 1.8 shows several different SB images of the simulation at  $z = 4.8$ . The region of panel a has already been shown in Fig. 1.4 as region 1, while the other three images (panels b-d) are the angular size of  $1 \times 1 \text{ arcmin}^2$  and have a grid size of  $300 \times 300$  pixels (corresponding to the FOV of the current MUSE instrument). In panels b-d, halos with halo mass of  $M_h > 10^{9.5} M_\odot$  are shown as circles. Their size indicates their projected virial radii,  $R_{\text{vir}, 200}$ , which is the radius within which their mass would result in a mean halo density of 200 times the mean density. Furthermore, the

<sup>3</sup>Throughout this work, quoted halo masses are the dark matter mass of halos identified in the output snapshots of the simulation by a friends-of-friends algorithm with linking length 0.2, roughly corresponding to masses measured in spherical regions with a density of  $\Delta = 200$  times the mean density of the Universe, that is  $M_{200m}$  (see e.g. [Tinker et al., 2008](#)).

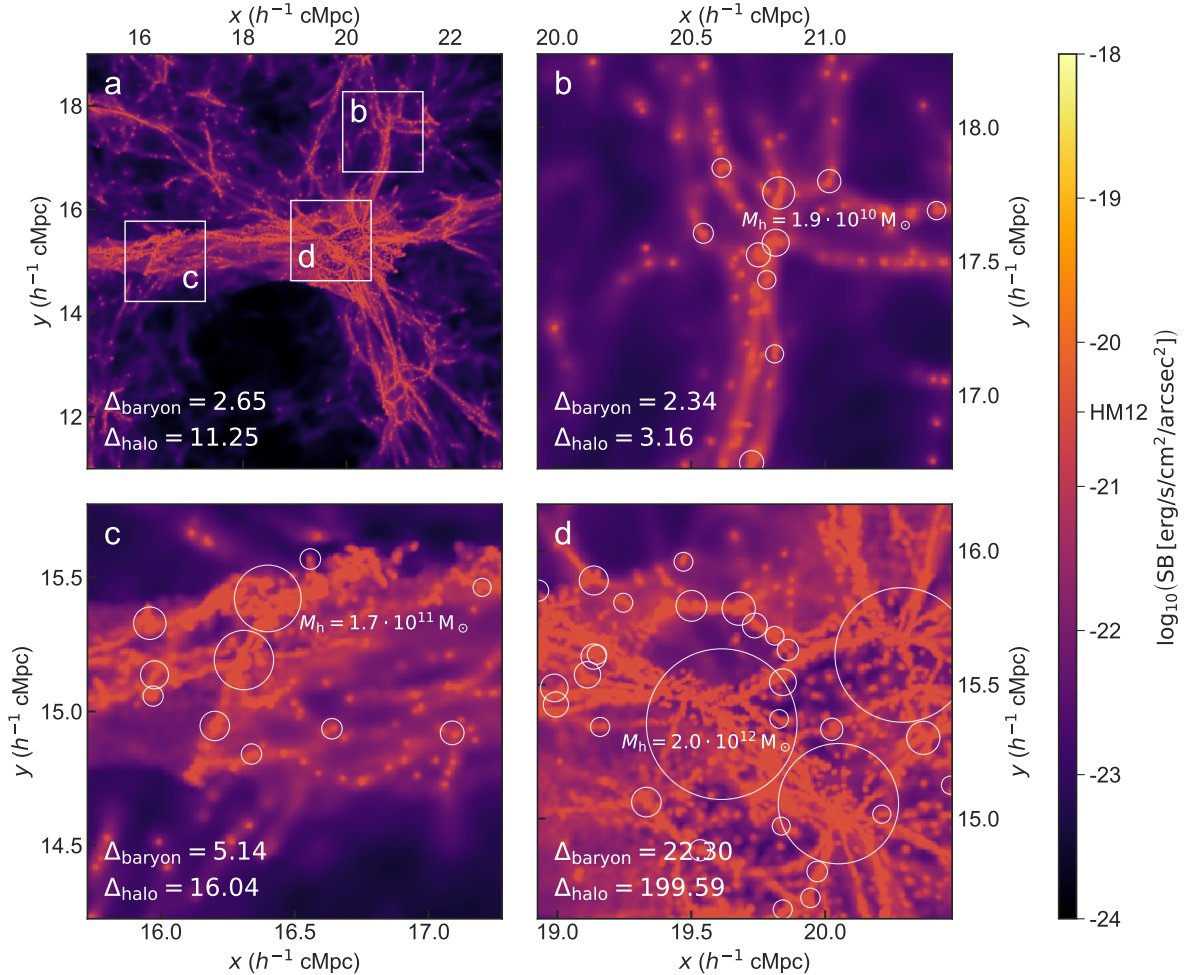


**Figure 1.8** Ly $\alpha$  SB for a narrowband with a smaller value of  $\Delta\lambda_{\text{obs}} = 3.75$  (i.e.  $\sim 1.19 h^{-1} \text{cMpc}$ ) in a simulation snapshot at  $z = 4.8$ . As in Fig. 1.8, the SB shown is a combination of recombination emission (of all gas in the simulation) below the mirror limit (indicated on the colour bar as HM12), and collisional excitation of gas below half the critical self-shielding density. Panel **a** shows an overview narrowband image that corresponds to region 1 in Fig. 1.4. This is centred on the same comoving coordinates both spatially and spectrally, but now less extended in wavelength range as the narrowband width has been decreased. This panel shows a region of  $8 \times 8 h^{-2} \text{cMpc}^2$  ( $5.2 \times 5.2 \text{arcmin}^2$ ) on a pixel grid of  $1024 \times 1024$ . Panels **b-d** show Ly $\alpha$  narrowband images the size of  $1 \times 1 \text{arcmin}^2$  consisting of  $300 \times 300$  pixels (as the FOV of MUSE). The volume probed by one of these narrowband images at this redshift is  $2.84 h^{-3} \text{cMpc}^3$ . The areas covered by these maps are indicated by the white squares in the overview panel **a**. Halos with halo mass of  $M_h > 10^{9.5} M_\odot$  are shown as circles, their size indicating their projected virial radius (see text). The most massive halo in each panel is annotated. In the bottom left corner of each panel, two different measures of the overdensity of the region are shown (see text for more details). The baryonic overdensity is calculated taking all gas into account, even though only gas below a certain density contributes to the collisional excitation.

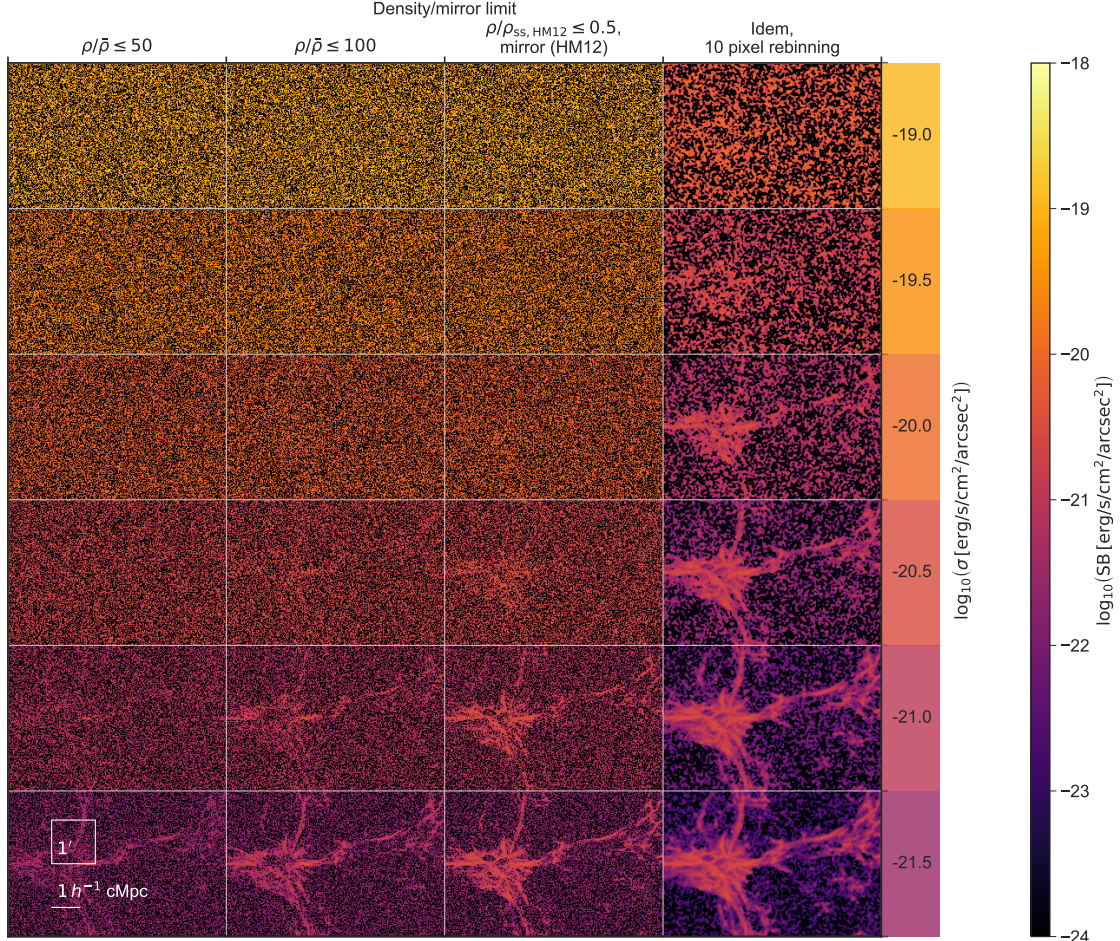


**Figure 1.9** Repeated view of region 2 of the  $z = 4.8$  SB map in Fig. 1.4 for different noise levels and assumptions on various limits. The SB map has a narrowband with  $\Delta\lambda_{\text{obs}} = 3.75$  ( $\sim 1.19 h^{-1} \text{cMpc}$ ) and is convolved with a Gaussian kernel with a FWHM of 0.75 arcsec before adding noise (as in the HDFS observation, see Bacon et al., 2015). The spatial extent of each panel is  $5 \times 3.3 \text{ arcmin}^2$ , or  $7.8 \times 5.2 h^{-2} \text{ cMpc}^2$ . The  $1\sigma$  levels of the Gaussian noise applied per pixel (before rebinning) to each panel in the entire row are indicated directly to the right of the mosaic, coloured according to the colour bar on the very right, while the density cut-off and mirror limit (if applied) for each column is shown above the mosaic (see text for details). The final column is identical to the column next to it, but has a smoothing of  $10 \times 10$  pixels or  $2 \times 2 \text{ arcsec}^2$  applied (see text). Scales of  $1 \times 1 \text{ arcmin}^2$  (the MUSE FOV) and  $1 h^{-1} \text{ cMpc}$  are indicated on the bottom left. Each panel in the image has  $1500 \times 1000$  pixels, again making the pixel size equal to that of MUSE (0.2 arcsec per pixel).

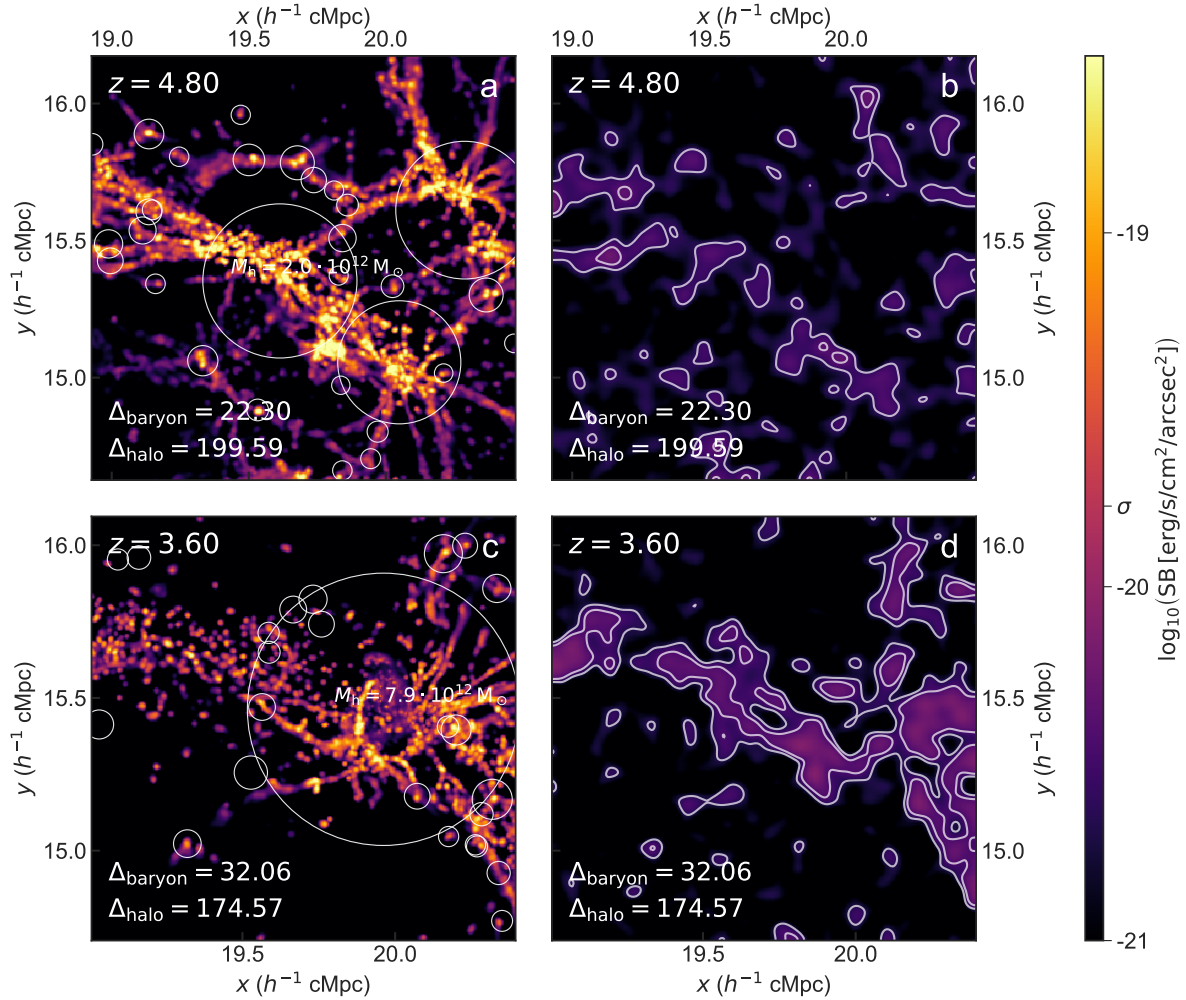


**Figure 1.10** Mock observations for a MUSE-like wide-field IFU instrument on the ELT covering the same region as panel d in Fig. 1.8 at two different redshifts ( $z = 4.8$  and  $z = 3.6$  on the top and bottom row, respectively) with no limits imposed and no observational effects vs. with mirror and density limits and modelled noise and seeing applied (left and right column, respectively; see text for details). The smaller narrowband with  $\Delta\lambda_{\text{obs}} = 3.75$  (i.e.  $\sim 1.19 h^{-1} \text{ cMpc}$ ) has been used again. These images have a different dynamical range than all other figures to accentuate the observable Ly $\alpha$  signal. In panels b and d, a rebinning of  $10 \times 10$  pixels ( $2 \times 2 \text{ arcsec}^2$ ) was applied, after which the image was smoothed on the same scale to recover the signal on larger scales. The white contours indicate measured  $3\sigma$  and  $5\sigma$  levels. The Ly $\alpha$  emission of IGM filaments can (marginally) be recovered in such an extremely deep observation and seems more feasible at low redshift when considering the robust lower limits (i.e. the mirror limit for recombinations and density threshold for collisional excitation; panel d); however, the predicted full intrinsic luminosity of filaments is notably higher at higher redshift (cf. panel a and c; see text for further discussion) but very dependent on the details of the modelling.

overdensity in each region shown is indicated in the bottom left corner of each panel in Fig. 1.8 according to the two different measures that have been introduced above.

Panels b–d show the signal as predicted from the simulation for three different ‘IFU pointings’. The volume probed by each of these images at this redshift is  $2.84 h^{-3} \text{ cMpc}^3$ . We note that we have chosen a smaller narrowband with  $\Delta\lambda_{\text{obs}} = 3.75$  or  $\sim 1.19 h^{-1} \text{ cMpc}$  at this redshift (equivalent to three spectral pixels of MUSE). Filamentary structures are still encapsulated in this width, while a smaller narrowband allows the signal to stand out more clearly from the noise: a wider narrowband, having more pixels in the spectral dimension, increases the overall noise level. The initial value of  $\Delta\lambda_{\text{obs}} = 8.75$ , which we adopted from [Wisotzki et al. \(2016\)](#), was chosen for the observation of Ly $\alpha$  halos. Since Ly $\alpha$  scattering occurs increasingly in high-density regions and in the high-velocity outflowing gas near galaxies (e.g. [Verhamme et al., 2006](#)), these structures of high density and high gas velocities cause the Ly $\alpha$  signal to be spread out over a larger wavelength range.

Filamentary structures, however, have lower densities and peculiar velocities; hence, they are contained in a narrower wavelength range. Therefore, while on average more individual filaments are present when the chosen narrowband width is larger, the signal from a given filament tends to get lost in the noise, as illustrated by Fig. 1.7. Fig. 1.8 indicates that individual filaments are still abundantly contained within these thin narrowband images with  $\Delta\lambda_{\text{obs}} = 3.75$ , which is getting near the limit of the typical spectral resolution ( $\Delta\lambda \approx 2.5$  for MUSE, see [Bacon et al. 2010](#)). The precise spectral line width is determined by the details of radiative transfer, since Ly $\alpha$  photons are scattered away from the resonance frequency, depending on the kinematics of the scattering medium (see Sect. A.2); however,  $\Delta\lambda_{\text{obs}} = 3.75$  covers a velocity range of  $\Delta v = 160 \text{ km/s}$ , which should be large enough to cover the line width for the modest optical depths in filaments (e.g. Eq. (21) in [Dijkstra, 2014](#)).

As expected, regions with a higher signal (see two bottom panels in Fig. 1.8) contain more high-mass ( $M_h > 10^{9.5} M_\odot$ ) halos compared to low-density regions (e.g. panel b) and are found to have a higher overdensity, in both our proxies for environment,  $\Delta_{\text{baryon}}$  and  $\Delta_{\text{halo}}$ . The Ly $\alpha$  emission is mainly originating from in and around the virial radii of these halos, but filamentary structures can be seen to extend between them, up to comoving megaparsec scales in panel d. We note that the panel c and d are probably the optimal pointings in the entire region shown in panel a, indicating that with a randomly chosen field, there is only a rather modest chance of observing a filamentary structure with this relatively high SB. Fig. 1.8 therefore highlights the importance of cosmic variance in detecting the filamentary structure of the IGM in Ly $\alpha$  emission. We conclude that both the instrument pointing and narrowband width chosen are essential to efficiently map the IGM in Ly $\alpha$  emission.

In practice, such overdensity candidates at  $z \sim 4$  are readily identified at an on-sky number density of  $\sim 1 \text{ deg}^{-2}$  in broadband surveys (e.g. [Toshikawa et al. 2016, 2018](#); the latter study identified  $\sim 180$  protocluster candidates over  $121 \text{ deg}^2$  at  $z \sim 4$ ). These still require spectroscopic

follow-up observations of several individual member galaxies, however, to exclude the possibility of multiple overlapping structures in projection. The feasibility of such campaigns was for example demonstrated by [Toshikawa et al. \(2016\)](#). These authors confirm three out of four candidate protoclusters over a  $\sim 4 \text{ deg}^2$  area at  $z \sim 3\text{-}4$  (in excellent agreement with the expected fraction of true positives from cosmological simulations of more than 76%) using just over  $\sim 1 \text{ h}$  of spectroscopic observations with Subaru/FOCAS per protocluster candidate, thereby reaching a spectral resolution of  $\Delta\lambda_{\text{obs}} \sim 2.5$ .

We note that while a small narrowband width ( $\Delta\lambda_{\text{obs}} = 3.75$  or  $\Delta z \sim 0.003$  as in Fig. 1.10) is optimal for a subsequent deep imaging campaign of extended, filamentary Ly $\alpha$  emission with a wide-field IFU, not all protocluster members necessarily need to be contained within such a narrow redshift range, since an IFU flexibly allows for the extraction of multiple pseudo-narrowbands along redshift space. Moreover, the IFU observation simultaneously provides the spectroscopic redshift of several galaxies in the protocluster through their Ly $\alpha$  emission or even fainter UV metal absorption or emission lines, if the exposure is sufficiently deep; this result can help guide the placement of such pseudo-narrowbands.

These recent studies furthermore give rise to a promising outlook for the search of protocluster candidates with extragalactic surveys in the near future. Just over two years into its main survey, the Vera Rubin Observatory has already reached a limiting  $i$ -band AB-magnitude of  $\sim 26$  ([Ivezić et al., 2019](#)), a depth similar to that of the survey used in [Toshikawa et al. \(2018\)](#), while the full 10-year survey (reaching 26.8 mag) will even approach the depth of the  $\sim 4 \text{ deg}^2$  field considered by [Toshikawa et al. \(2016\)](#).

### Sensitivity analysis

In Fig. 1.9, in all panels, a similar, small section of the main SB map at  $z = 4.8$  (region 2 in Fig. 1.4) is shown in the same narrowband with  $\Delta\lambda_{\text{obs}} = 3.75$  (i.e.  $\sim 1.19 h^{-1} \text{ cMpc}$ ), now with a Gaussian smoothing (FWHM of 0.75 arcsec). The columns show different assumptions on various limits (e.g. the signal from gas below 50 and 100 times the mean baryonic density,  $\bar{\rho}$ ), while the overlaid Gaussian noise varies per row. Noise levels quoted are their values per pixel (before rebinning, discussed below). The pixels agree in size with those of MUSE (0.2 arcsec). Apart from the different gas density thresholds, the two columns on the right show the expectation in the mirror assumption, where, in addition to the collisional excitation luminosity of gas below a density of half the critical self-shielding density, we calculate the recombination luminosity arising from gas at all densities, but with the SB limited from above by the mirror value (see Sect. 1.2.1). At this redshift, the limit is equal to  $\text{SB} \simeq 3.29 \cdot 10^{-21} \text{ erg s}^{-1} \text{ cm}^{-2} \text{ arcsec}^{-2}$  for a [HM12](#) UVB. Finally, the last column is rebinned on a scale of  $10 \times 10$  pixels ( $2 \times 2 \text{ arcsec}^2$ ) and subsequently convolved with a Gaussian with FWHM of equal size.

This particular region, chosen for its juxtaposition of both an under- and overdense region, shows that Ly $\alpha$  emission arising from the less dense components of filamentary structures can

only be detected with very high sensitivities (of  $\lesssim 10^{-20.5} \text{ erg s}^{-1} \text{ cm}^{-2} \text{ arcsec}^{-2}$  for overdensities of  $\rho/\bar{\rho} \leq 100$ ). Still, with image analysis techniques (e.g. rebinning pixels), the signal of these filaments can stand out at a noise level of  $\sigma \sim 10^{-19.5} \text{ erg s}^{-1} \text{ cm}^{-2} \text{ arcsec}^{-2}$ . Considering that the sensitivity in recent observations reaches a limiting SB of  $\sim 10^{-19} \text{ erg s}^{-1} \text{ cm}^{-2} \text{ arcsec}^{-2}$  (e.g. Bacon et al., 2015, 2017, 2021) or for median-stacked radial profiles even down to  $\text{SB} \sim 4 \cdot 10^{-21} \text{ erg s}^{-1} \text{ cm}^{-2} \text{ arcsec}^{-2}$  (or  $\log_{10} \text{SB} \simeq -20.4$ ; see Wisotzki et al. 2018), this suggests that the very deepest observations are getting close to the detection of such filamentary structures.

Returning to the region shown in panel d of Fig. 1.8, we construct mock observations for a MUSE-like, wide-field integral-field spectrograph on the ELT at two different redshifts,  $z = 4.8$  and  $z = 3.6$ , in Fig. 1.10. The left panels show emission from all gas without any limits, while the right panels show the combination of recombination emission of all gas in the simulation below the mirror limit, and collisional excitation of gas below half the critical self-shielding density, as before. The panels on the right are convolved with a Gaussian PSF corresponding to a FWHM of 0.75 arcsec (as in the HDFS observation, see Bacon et al., 2015) and include modelled noise. The noise level has been inferred from a continuum-subtracted pseudo-narrowband image (with the same width) constructed from the 27h MUSE HDFS observation (Bacon et al., 2015) at  $\sim 7200$ , where the throughput of MUSE is at its maximum of  $\sim 40\%$  (e.g. Richard et al., 2019, ; but see also Fig. 1.7); the  $1\sigma$  level of the inferred noise in this case is  $\sigma = 1.72 \cdot 10^{-19} \text{ erg s}^{-1} \text{ cm}^{-2} \text{ arcsec}^{-2}$ . Subsequently, the noise level is adjusted to correspond to a MUSE-like instrument on the ELT by scaling the sensitivity by the square root of the ratio of collecting areas between the VLT and ELT ( $52 \text{ m}^2$  and  $978 \text{ m}^2$ , respectively<sup>4</sup>) and an increased integration time of  $t = 150 \text{ h}$  (again assuming a  $1/\sqrt{N}$  scaling of the noise level with  $N$  the number of collected photons, resulting in a factor  $\sqrt{150/27} \simeq 2.36$  lower noise in this case). The resulting noise level is  $\sigma = 1.68 \cdot 10^{-20} \text{ erg s}^{-1} \text{ cm}^{-2} \text{ arcsec}^{-2}$  (indicated on the colour bar).

There are two different evolutions in redshift at play in Fig. 1.10. First of all, we conclude that without conservative limits (not imposing the mirror limit and including gas at higher densities), the Ly $\alpha$  emission along filaments, originating from dense gas in halos and galaxies embedded in these filaments, is significantly brighter at higher redshift. This is clear from the comparison of the left panels between the two redshifts,  $z = 4.8$  and  $z = 3.6$  (panels a and c) and is an illustration of the cosmic density evolution winning over the increased SB dimming, as discussed in Sect. 1.3.1. The modelling of the dense gas dominating the emission is, however, very uncertain. A robust prediction can be obtained for low-density filamentary gas, for which we find that it can only be marginally detected in an extremely deep observation with an ELT-class telescope (panels b and d). In our most robust predictions, excluding emission from the dense (and complicated) central regions of halos, Ly $\alpha$  emission appears brighter at

<sup>4</sup>See for example <https://www.eso.org/sci/facilities/paranal/telescopes/ut/m1unit.html> and <https://www.eso.org/public/teles-instr/elt/numbers/>.

low redshift, where the mirror limit is less affected by SB dimming and self-shielding effects only start to play a role at higher overdensities (SB maps for a larger range of redshifts are shown in Sect. A.3). Future work that includes models with more detailed galaxy formation physics, simultaneously capturing the effects of self-shielding and baryonic feedback processes on high-density gas, is needed to investigate how precisely these two effects compete at different redshifts. An accurate treatment of the high-density gas is needed to point out the optimal redshift to observe gas in different environments.

## 1.4 Conclusions

We have presented simulation predictions on the properties of Ly $\alpha$  emission from low-density gas in the IGM at redshifts  $2 < z < 7$ . Based on our simulations we predict the Ly $\alpha$  emissivity due to recombinations and collisional excitations in the gas, carefully considering the relevant physical processes. We employed an on-the-fly self-shielding mechanism and neglected the effect of Ly $\alpha$  scattering, which is expected to be moderate in the low-density IGM. We impose the mirror limit for recombination emission and primarily focus on the regime that is not affected strongly by self-shielding for emission produced by collisional excitation by only considering gas that is well below the self-shielding critical density ( $\rho/\bar{\rho} \sim 100$  at  $z = 4.8$ ).

We found recombination to dominate at lower densities, while collisional excitation becomes the main emission process at higher densities. Recombination and collisional excitation contribute approximately equally for the regime we focus on, below half the self-shielding critical overdensity ( $\rho/\bar{\rho} \lesssim 50$  at  $z = 4.8$ ). Gas near or somewhat above the critical self-shielding density contributes significantly to luminosity produced through both channels. We show that our prediction of recombination emission including all gas, while having the mirror limit imposed, combined with collisional excitation emission of low-density gas, should yield a robust lower limit. The prediction for Ly $\alpha$  emission of collisionally excited gas at higher densities is more uncertain, and we therefore leave this task to future work.

Our predicted values of the SB at  $z = 4.8$  for narrowband images with  $\Delta\lambda_{\text{obs}} = 8.75$  are of the order of  $\text{SB} \lesssim 10^{-23} \text{ erg s}^{-1} \text{ cm}^{-2} \text{ arcsec}^{-2}$  for the void regions, increasing to  $\sim 10^{-21} \text{ erg s}^{-1} \text{ cm}^{-2} \text{ arcsec}^{-2}$  for the diffuse gas in filaments. Denser gas within (the halos of) galaxies embedded in the filaments can reach higher values and likely dominates the total emission from filaments. The modelling of this component is, however, very challenging as it depends on the details of the radiative transfer and feedback processes.

We briefly discussed the prospects of targeting diffuse Ly $\alpha$  emission with various spectrographs at different telescopes. At this moment, VLT/MUSE is arguably the best option for imaging the Ly $\alpha$  emission from gas in the filamentary structure of the cosmic web owing to its comparably large FOV ( $1 \times 1 \text{ arcmin}^2$ ) and spectral coverage (4650-9300, and thus accessible redshift range of 2.8-6.7 for Ly $\alpha$ ), while maintaining a high spatial resolution (0.2 arcsec sam-

pling) and good spectral resolution (ranging between 1770–3590). Recent deep observations reaching a limiting Ly $\alpha$  SB of  $\sim 10^{-19}$  erg s $^{-1}$  cm $^{-2}$  arcsec $^{-2}$  (e.g. [Bacon et al., 2015, 2017, 2021](#)), or for median-stacked radial profiles even down to SB  $\sim 4 \cdot 10^{-21}$  erg s $^{-1}$  cm $^{-2}$  arcsec $^{-2}$  (or  $\log_{10}$  SB  $\simeq -20.4$ ; see [Wisotzki et al. 2018](#)), suggest that the deepest current observations are already beginning to probe the extended Ly $\alpha$  radiation emitted by low-density gas ( $\rho/\bar{\rho} \lesssim 100$ ) associated with filamentary structures; this observed emission, however, is likely dominated by dense gas in halos and galaxies embedded in them.

In our most conservative predictions, which should be considered as a lower limit, we exclude emission from the dense (and complicated) central regions of halos. In those predictions, the Ly $\alpha$  emission appears brighter at low redshift, where the mirror limit is less affected by SB dimming and self-shielding effects only start to play a role at relatively high overdensities. Our mock observations, which aim to simulate observations of regions at different overdensities, show a large amount of variance between fields. This variance makes densely populated protoclusters more promising targets for detecting the IGM in Ly $\alpha$  emission. Our findings suggest an observing strategy exploiting a targeted search of such a distant protocluster could potentially allow deep observations with a wide-field IFU instrument on an ELT-class telescope, a successor to MUSE, to directly map the intergalactic, low-density gas in Ly $\alpha$  emission in detail.



## CHAPTER 2

### ASSESSING THE SOURCES OF REIONISATION: A SPECTROSCOPIC CASE STUDY OF A 30 $\times$ LENSED GALAXY AT $z \sim 5$ WITH Ly $\alpha$ , CIV, Mg II, AND [Ne III]

---

#### 2.1 Introduction

Space-based observatories such as *Hubble Space Telescope (HST)* and *Spitzer* and ground-based 8 m-class telescopes have transformed our view of galaxy evolution in the high-redshift Universe, identifying statistically substantial samples of distant galaxies in deep imaging surveys beyond  $z > 4$  (Madau & Dickinson, 2014). At this epoch, covering the first  $\sim 10\%$  of the current age of the Universe, the physical properties of galaxies were likely to be very different to those today, with metal-poor stellar populations, low stellar masses, and hard radiation fields. These conditions are favourable to strong nebular emission, despite the weak stellar continuum (e.g. Stark, 2016). Equally, this suggests the faint galaxy population in the Epoch of Reionisation (EoR) can contribute significantly to reionisation (e.g. Bouwens et al., 2015).

This picture has mainly emerged from spectroscopic follow-up observations of individual distant sources selected in deep photometric surveys, although this poses several challenges. From the ground, near-infrared (NIR) spectrometers are restricted by Earth's atmosphere to observe key rest-frame optical emission line features, such as H $\alpha$ , [O III]  $\lambda 5008$ , and [O II]  $\lambda 3727, 3730$  (simply [O II] hereafter) out to redshifts of about 2.5, 3.6, and 5.2, respectively. The much-anticipated *James Webb Space Telescope (JWST)* will explore the rest-frame optical spectra of more distant objects ( $z \sim 4\text{--}12$ ), which will enable the use of many emission line diagnostics that are carefully calibrated with the wealth of data for more nearby galaxies, like the optical classification schemes that distinguish spectra of star-forming galaxies shaped by nebular emission from H II regions from those dominated by emission of the narrow-line region of Active Galactic Nuclei (AGN; Baldwin, Phillips & Terlevich 1981, BPT hereafter; Veilleux & Osterbrock 1987).

Meanwhile, several new methods have been explored, which even as *JWST* is launched will prove valuable in the era of Extremely Large Telescopes (i.e. ELT, GMT, and TMT).

For example, alternative classification schemes to the BPT classification have been proposed, targeting the rest-frame ultraviolet (UV) instead: these use highly ionised gas lines such as C III]  $\lambda 1907$ , [C III]  $\lambda 1909$  (C III collectively), C IV  $\lambda 1548, 1551$  (C IV), and He II  $\lambda 1640$  (He II) to separate star-forming galaxies from AGN (e.g. [Feltre et al., 2016](#)). These lines are much brighter in the composite spectra of  $z \sim 3$  Lyman-break galaxies than observed in the local Universe (e.g. [Shapley et al., 2003](#)). Another pressing challenge is to find a reliable method to uncover the sources responsible for reionisation by indirectly identifying Lyman-continuum (LyC) leakage in the EoR, where LyC and H I Lyman- $\alpha$  (Ly $\alpha$ ) becomes inaccessible due to absorption by the neutral IGM. Methods aimed at characterising EoR galaxies, such as the UV classification schemes and indirect proxies of LyC escape, can be tested at (slightly) lower redshift where features are readily observable with current instrumentation, ideally with analogues of high-redshift galaxies.

In this work, we present one such case study, investigating in detail the emission line properties of RCS0224z5, a strongly lensed galaxy at redshift  $z \simeq 4.88$  in the background of the RCS 0224–0002 cluster. RCS 0224–0002, a galaxy cluster at  $z = 0.773$ , was discovered in the Red-Sequence Cluster Survey (RCS; [Gladders et al., 2002](#)). Several arc-like structures were found in this study, among which an arc consisting of four images of a gravitationally lensed background galaxy at  $z \simeq 4.88$ , identified via its Ly $\alpha$  emission. The magnification of the four images ranges from  $\mu = 1.30$  to  $\mu \sim 140$ , making this only one of three known sources at  $z \gtrsim 5$  with a comparably high magnification ([Franx et al., 1997](#); [Swinbank et al., 2009](#); [Khullar et al., 2021](#)) – and placing this galaxy at less than 300 Myr after the end of reionisation. Follow-up observations with VLT/MUSE have furthermore revealed spatially widespread and narrow (FWHM  $\simeq 156$  km/s) C IV emission with a high equivalent width (EW) of  $\sim 10$  in the rest frame ([Smit et al., 2017](#)), similar to what is being observed in an increasing number of  $z \sim 6$ -8 galaxies ([Stark et al., 2015](#); [Mainali et al., 2017](#); [Laporte et al., 2017](#)), but rarely seen in the local Universe ([Berg et al., 2019a](#); [Senchyna et al., 2019](#)).

We present new VLT/X-shooter observations that constrain the rest-frame UV emission line diagnostics that are inaccessible within the MUSE wavelength range. Unlike sources at higher redshift, where no rest-frame optical features are accessible from the ground, [Swinbank et al. \(2007\)](#) presented widespread [O II] detected in deep SINFONI observations. We present the additional detection of [Ne III]  $\lambda 3870$  emission and corresponding new measurement of the [Ne III]/[O II] line diagnostic to place this system in the context of the local galaxy population, in order to gain insight into the origin of high-EW C IV emission in the early Universe. Finally, we report the detection of Mg II  $\lambda 2796$  in emission: a remarkable finding, as this is in stark contrast with the local galaxy population, where it is mostly observed in absorption (e.g. [Kinney et al., 1993](#)). Being a resonant transition like Ly $\alpha$ , it has the potential to be an indirect tracer of LyC escape (e.g. [Henry et al., 2018](#)).

## 2.2 Observations

---

**Table 2.1** Overview of the observed emission lines in the X-shooter and SINFONI spectra. For non-detections, upper limits are given (see Sect. 2.3.1 for details).

Instrument	Image(s) <sup>a</sup>	Feature	$\lambda_{\text{vac}} (\text{\AA})^b$	$\Delta v (\text{km/s})^c$	Flux ( $10^{-18} \text{ erg s}^{-1} \text{ cm}^{-2}$ ) <sup>d</sup>	EW () <sup>e</sup>
<i>X-shooter</i>	1	Ly $\alpha$	1215.67	$156 \pm 52$	$440.4 \pm 5.9$	$143.3 \pm 12.9$
		C IV	1548.19	$104 \pm 53$	$12.7 \pm 3.1$	$11.9 \pm 3.2$
		C IV	1550.77	$104 \pm 53$	$6.18 \pm 3.48$	$5.78 \pm 3.34$
		He II	1640.42	...	$< 6.11$	$< 6.21$
		[C III]	1906.68	...	$< 26.7$	$< 35.2$
		[C III]	1908.73	...	$< 46.0^f$	$< 25.4^f$
		Mg II	2796.35	$52 \pm 54$	$5.00 \pm 1.49$	$16.2 \pm 5.1$
<i>SINFONI</i>	2 and 3	[O II]	3727.09	$0 \pm 13$	$60.5 \pm 4.5$	...
		[O II]	3729.88	$0 \pm 13$	$71.4 \pm 4.5$	...
		[Ne III]	3869.85	$0 \pm 13$	$60.4 \pm 12.6$	...

<sup>a</sup> Lensed image(s) from which the spectroscopic measurements were taken (see Sects. 2.2.1 and 2.2.2 for details).

<sup>b</sup> Vacuum rest-frame wavelength.

<sup>c</sup> Velocity offset with respect to the systemic redshift as measured by the relevant instrument (X-shooter:  $z_{\text{sys}} = 4.8737$ , SINFONI:  $z_{\text{sys}} = 4.8754$ ). Uncertainty in the velocity offsets includes the uncertainty in determining the systemic redshift (see Sect. 2.3).

<sup>d</sup> Observed fluxes, uncorrected for the lensing magnification factor of  $\mu = 29_{-11}^{+9}$  of image 1, observed by X-shooter (Sect. 2.2.1), and  $\mu = 21_{-8}^{+12}$  and  $\mu = 138_{-74}^{+7}$  of image 2 and 3 respectively, observed collectively by SINFONI (Sect. 2.2.2).

<sup>e</sup> Rest-frame equivalent width (EW; positive values indicating a feature is observed in emission). Note that EWs are independent of lensing magnification.

<sup>f</sup> Upper limits inferred under the assumption of a minimum ratio of  $F_{1907}/F_{1909} \approx 1.39$  for  $n_e \leq 10^3 \text{ cm}^{-3}$  (see Sect. 2.3.1).

The outline of this paper is as follows. In Sect. 2.2, we describe the observations, and in Sect. 2.3 we present the results. In Sect. 2.4 we discuss the outcomes, and we finally summarise our findings in Sect. 2.5. In our analysis, we adopt the cosmological parameters  $\Omega_m = 0.3$ ,  $\Omega_\Lambda = 0.7$ , and  $H_0 = 70 \text{ km s}^{-1} \text{ Mpc}^{-1}$  throughout (implying an angular scale of 6.4 kpc/arcsec at  $z = 4.88$ ), to ease comparison with previous studies. All magnitudes are in the AB system (Oke & Gunn, 1983).

## 2.2 Observations

### 2.2.1 X-shooter spectroscopy

Observations of the lensed image 1 of RCS0224z5, amplified by  $\mu = 29_{-11}^{+9}$  (luminosity-weighted; see Smit et al., 2017), were taken with the VLT/X-shooter (Vernet et al., 2011) on 11, 14, and 16 October 2018 with a total on-source time of 3.5 h, under ESO programme ID 0102.A-0704(A) (PI: Smit); the slit was centred at  $\alpha = 02:24:33.83$ ,  $\delta = -00:02:17.91$  (Fig. 2.1) and using slit

**Assessing the sources of reionisation: a spectroscopic case study of a  $30\times$  lensed galaxy at  $z \sim 5$  with Ly $\alpha$ , C IV, Mg II, and [Ne III]**

---

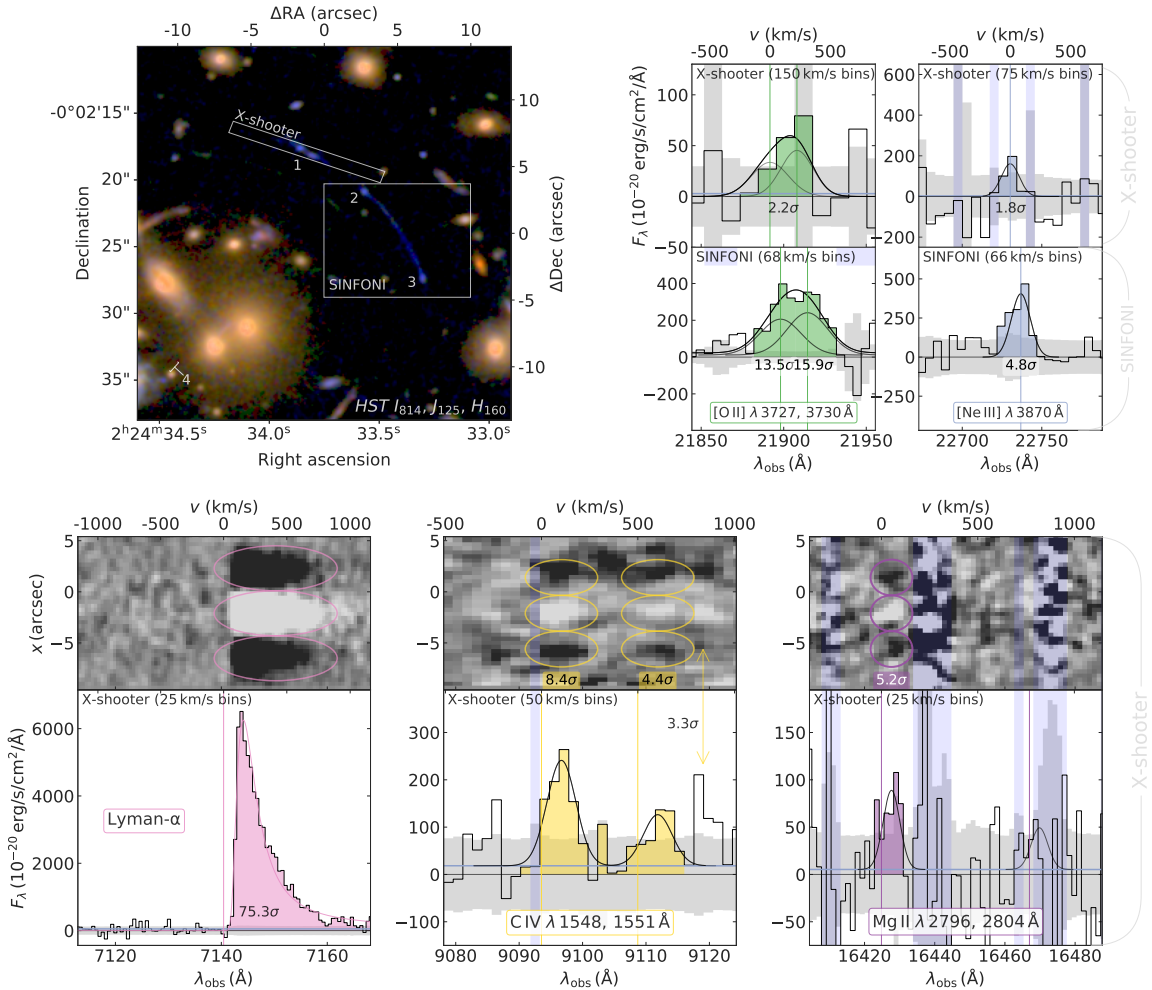


**Figure 2.1** Overview of the observations discussed in Sects. 2.2.1 to 2.2.3. *Top left:* HST false-colour  $I_{814}$ ,  $J_{125}$ , and  $H_{160}$  image of RCS 0224-0002, indicating the lensed galaxy images 1–4 and the FOV of the observations covering the arc of RCS0224z5. *Top right:* [O II] and [Ne III] in both X-shooter and SINFONI spectra. *Bottom row:* spectra of Ly $\alpha$ , C IV, and Mg II emission lines observed with VLT/X-shooter. An arrow marks a tentative  $\sim 3\sigma$  redshifted component of C IV, see Sect. 2.3.1. In two-dimensional X-shooter spectra, the dark-light-dark signature of detected lines are highlighted with coloured ellipses (Sect. 2.2.1). Labels indicate the significance of each detection measured in a SNR-optimised aperture (larger for Ly $\alpha$ , smaller for C IV and Mg II), while all one-dimensional spectra shown are extracted from a larger aperture to capture the entire flux as reported in Table 2.1 (see Sect. 2.3.1 for details). The grey filled-in area shows the  $1\sigma$  uncertainty level. The rest-frame UV continuum fit is shown with a blue line. Velocities are based on the corresponding systemic redshift of [O II] (Sect. 2.3) and are centred on the brightest line for doublets.

widths of  $1.2''$  and  $0.9''$  in the visible (VIS) and near infrared (NIR), resulting in a spectral resolution  $R \equiv \lambda/\Delta\lambda \approx 6500$  and  $R \approx 5600$ , respectively, in the two arms. Observations were taken with AB nodding with an offset of  $3.8''$  and individual exposures were 383 s in the VIS and 230 s NIR arm. Observations were taken with an average airmass of 1.14 and seeing of  $0.8''$ . Data reduction was performed using the standard ESOREFLEX X-shooter pipeline (Freudling et al., 2013). We apply the nodding-mode reduction, as well as stare-mode reduction with a manual algorithm to combine frames from the ‘ABBA’ nodding pattern, depending on which yields the best results; the manual stare-mode reduction is used throughout, except for the C IV line. Individual OBs were separately corrected for telluric absorption in the VIS and NIR arms using MOLECFIT (Smette et al., 2015; Kausch et al., 2015).

### 2.2.2 SINFONI spectroscopy

Reduction of the SINFONI IFU spectroscopy is described in Swinbank et al. (2007). In short, IFU spectroscopy was performed for a total of 12 h on source with VLT/SINFONI (Eisenhauer et al., 2003; Bonnet et al., 2004) under ESO programme ID 075.B-0636(B). The data were taken in the HK grating, resulting in a spectral resolution of  $R \approx 1700$ , with a  $\sim 8 \times 8$  arcsec $^2$  field of view (at a spatial sampling of 0.25 arcsec/pixel), covering the lensed images 2 and 3 of RCS0224z5 (luminosity-weighted amplifications of  $\mu = 21_{-8}^{+12}$  and  $\mu = 138_{-74}^{+7}$ , respectively; Smit et al. 2017). Lensed image 3 has a particularly high amplification (and corresponding uncertainty), as the arc crosses the lensing critical curve. We note that the source plane image of the galaxy is fully recovered by lensed image 1, but only partially in images 2 and 3: out of the two clumps seen in image 1, the one in north east is not reproduced in 2 and 3 (see Smit et al., 2017, for details).

### 2.2.3 HST imaging

*HST* imaging of RCS 0224–0002 is available on the Space Telescope Science Institute data archive<sup>1</sup> (GO 14497, PI: Smit; see Smit et al., 2017). Observations were performed with the Advanced Camera for Surveys (ACS) using the F814W ( $I_{814}$ ) filter (2.2 ks exposure), and with the Wide Field Camera 3 (WFC3) using the F125W ( $J_{125}$ ) and F160W ( $H_{160}$ ) filters (both 2.6 ks exposures). The resulting images reach a depth of 26.3 mag, 26.8 mag, and 26.7 mag in the  $I_{814}$ ,  $J_{125}$ , and  $H_{160}$  bands ( $5\sigma$  for a  $0.5''$ -diameter aperture). A false-colour image of these three bands is shown in the bottom left of Fig. 2.1.

---

<sup>1</sup>Data may be obtained from the MAST at [10.17909/T9-9KG5-HG27](https://doi.org/10.17909/T9-9KG5-HG27).

## 2.3 Results

In this study, we are mainly interested in line diagnostics using Ly $\alpha$ , C IV, He II, the C III doublet, Mg II  $\lambda 2796, 2804$  (Mg II), [O II], and [Ne III]  $\lambda 3870$  ([Ne III]).<sup>2</sup> The measured velocity offsets, line fluxes, and rest-frame EWs (or upper limits) of these lines presented in Fig. 2.1 are summarised in Table 2.1. In the following paragraphs, we will discuss the results for the X-shooter and SINFONI data sets individually.

We derive the systemic redshift from the [O II]  $\lambda 3727, 3730$  doublet in combination with the [Ne III]  $\lambda 3870$  line for increased precision; for X-shooter, this is measured to be  $z_{\text{sys}} = 4.8737 \pm 0.0010$  (uncorrected for a negligible barycentric velocity of 5–7 km/s), while for SINFONI it is  $z_{\text{sys}} = 4.8754 \pm 0.0003$  (again not corrected for a barycentric velocity of up to 27 km/s or  $\Delta z = 0.0005$ , but consistent with  $z_{[\text{O II}]} = 4.8757 \pm 0.0005$  measured by [Swinbank et al. 2007](#)), leaving a difference of  $\Delta z = 0.0017$ . In both cases, we simultaneously fit the [O II] and [Ne III] lines while fixing the [O II] line ratio, due to limited spectral resolution and signal to noise. We adopt a ratio of  $F_{3730}/F_{3727} = 1.18$ , the median of  $z \sim 2.3$  star-forming galaxies reported by [Sanders et al. \(2016\)](#), corresponding to an electron density  $\sim 10^2 \text{ cm}^{-3}$ . Importantly, the [O II] flux, and hence the [Ne III]/[O II] line ratio, are practically invariant when fitting with a freely varying [O II] line ratio. For X-shooter, the fit was performed on spectra rebinned to 150 km/s and 75 km/s for [O II] and [Ne III] respectively, using the intrinsic line widths obtained from the fit to the SINFONI spectrum. The  $\sim 2\sigma$  discrepancy between the systemic redshifts determined by X-shooter and SINFONI, equivalent to  $88 \pm 52$  km/s, may be a calibration problem (exceeding barycentric velocity corrections); or, given that the two spectra probe different images (see Fig. 2.1), the velocity difference can be a consequence of real kinematic differences between the two components. In the following, we measure offsets from the systemic redshift using the consistent measurement in the same image, and by the same instrument. We include the uncertainty in determining the systemic redshift (i.e. 52 km/s for X-shooter) in the uncertainty on all velocity offsets.

For all line flux measurements, we fit Gaussian profiles to the one-dimensional spectra. The uncertainty is estimated by scaling the flux uncertainty of a single spectral channel,  $F_\lambda \Delta\lambda$ , by the square root of the number of spectral bins where line flux is detected (coloured channels in Fig. 2.1).

### 2.3.1 X-shooter

The relevant X-shooter data are presented in the bottom row of Fig. 2.1, which shows one-dimensional spectra extracted from a  $2.4''$  aperture for all lines except Ly $\alpha$ , where we use a  $3.2''$  aperture. These spectra are used to measure the velocity offsets and total fluxes (Table 2.1).

<sup>2</sup>In this work, we use vacuum wavelengths throughout (see Table 2.1); emission line labels reflect vacuum wavelengths, rounded to the nearest integer.

## 2.3 Results

---

The annotated labels show the signal-to-noise ratio (SNR) measured in a smaller  $1.4''$  aperture, again except for Ly $\alpha$  where the extended aperture yields a higher SNR. We detect strong Ly $\alpha$  emission (at  $\sim 80\sigma$  in a  $3.2''$  aperture or  $\sim 50\sigma$  in a  $1.4''$  aperture; in the  $1.4''$  aperture, the Ly $\alpha$  EW decreases to  $78$ ), as well as the C IV doublet, at  $8.4\sigma$  and  $4.4\sigma$ . Finally, we detect the Mg II  $\lambda 2796$  line at  $5.2\sigma$  (see Sect. B.1 for more details on the significance of this detection). This makes RCS0224z5 the highest redshift galaxy for which Mg II emission has been detected. After Ly $\alpha$ , the Mg II  $\lambda 2796$  line has the highest EW out of all emission features detected in the rest-frame UV, even though the other line of the doublet, Mg II  $\lambda 2804$ , is undetected due to skylines. We show the expected signal for Mg II  $\lambda 2804$  in Fig. 2.1 assuming a typical flux ratio of  $F_{2796}/F_{2804} \approx 1.9$  between the Mg II lines at 2796 and 2804 (e.g. Henry et al., 2018), which is indeed below the estimated uncertainty level.

The blue line in the C IV doublet, C IV  $\lambda 1551$ , appears to have a weak second redshifted component ( $\sim 3\sigma$ ), although the negative signature in the two-dimensional spectrum seems mostly absent, which is why we do not include it in our analysis. At the current sensitivity and spectral resolution, we cannot confidently explain the nature of this feature; however, note that if this emission feature is included in the C IV flux and EW, this would not affect our conclusions in Sect. 2.4.1 regarding the origin of highly ionised emission.

With X-shooter, we detect the [O II] doublet and [Ne III] at  $2.2\sigma$  and  $1.8\sigma$  by rebinning to  $150\text{ km/s}$  and  $75\text{ km/s}$ , respectively (both in a  $1.4''$  aperture to maximise SNR). In our analysis, however, we will adopt the measurements of SINFONI at higher significance (see Sect. 2.3.2). Furthermore, as shown in Table 2.1, we obtain upper limits on emission from the He II line and the C III doublet. Since both lines of the C III doublet fall directly on skylines, instead of a  $2\sigma$  limit from the noise as for He II, we take the integrated flux measured within  $-100\text{ km/s} < v < 100\text{ km/s}$  of the expected line centre of the 1907 line (which is slightly less affected by telluric absorption and skylines; see also Sect. B.1). We obtain an upper limit for the total flux of the doublet using the lowest physically attainable value of  $F_{1907}/F_{1909} \approx 1.39$  for  $n_e \leq 10^3\text{ cm}^{-3}$  (Kewley et al., 2019). If we take a ratio of  $\sim 0.34$  for  $n_e \leq 10^5\text{ cm}^{-3}$ , the resulting C IV/C III ratio we measure shifts by 0.36 dex, leaving our findings unaffected (Sect. 2.4.1). The O III]  $\lambda 1661, 1666$  doublet also remains undetected: the brightest line of the two, at 1666, falls on a skyline, and the second line at 1661 is too faint to provide useful upper limits on the doublet.

By rebinning to a lower spectral resolution (in bins of  $\Delta\lambda_{\text{obs}} = 200$ , masking skylines prior to rebinning), we detect the rest-frame UV continuum and assuming  $F_\lambda \propto \lambda^\beta$ , we measure a UV-continuum slope  $\beta = -2.36 \pm 0.28$ , in good agreement with  $\beta = -2.19 \pm 0.14$  as measured from the *HST*  $J_{125} - H_{160}$  colour (Smit et al., 2017). This continuum fit is shown in all X-shooter spectra in Fig. 2.1 with a blue line. Using this fit, we deduce the equivalent widths (or upper limits thereof) of observed lines.

### 2.3.2 SINFONI

In addition to the previously reported observation of the [O II] doublet with SINFONI ([O II]; [Swinbank et al., 2007](#)), at  $13.5\sigma$  and  $15.9\sigma$  respectively, we present a new  $4.8\sigma$  detection of the [Ne III] line (see Fig. 2.1), the highest redshift detection of this line to date. The [Ne III] feature is not confidently detected with X-shooter, likely due to the shorter exposure time (3.5 h versus 12 h).

Conversely, even though the SINFONI observations cover the wavelength of Mg II, it was not detected due to the lower spectral resolution of SINFONI ( $R \approx 1700$  or  $\Delta\lambda_{\text{obs}} \approx 10$  at the observed wavelength of Mg II, 16426) blending the signal with the strong skyline feature at 16435.

## 2.4 Discussion

### 2.4.1 C IV: driven by star formation or AGN activity?

The high equivalent width emission of C IV observed in RCS0224z5 ( $\sim 20$ ) suggests the presence of a source producing ionising photons above the ionisation potential of C III, 47.9 eV (e.g. [Berg et al., 2019b](#)), as well as a high production efficiency of LyC photons,  $\xi_{\text{ion}}$  (e.g. [Stark et al., 2015](#)). In determining the origin of such ionising radiation – star formation (SF) or AGN activity – comparisons between observations and predictions from photoionisation models (e.g. CLOUDY, see [Ferland et al. 2013](#); MAPPINGS, see [Dopita et al. 2013](#)) are now widely used (e.g. [Kewley et al., 2001](#); [Gutkin et al., 2016](#); [Feltre et al., 2016](#); [Maiolino & Mannucci, 2019](#)).

Fig. 2.2 examines the origin of the hard radiation field in RCS0224z5 with our constraints on the rest-frame UV line fluxes. The top panel of Fig. 2.2 shows the C IV/C III and C IV/He II line ratios (a SF vs. AGN diagnostic proposed by [Feltre et al., 2016](#)). We place lower limits on both ratios using the C IV detection and upper limits on C III and He II. For comparison we show grids and lines for modelled nebular emission and narrow-line region AGN emission coloured according to their metallicity (see legend; assuming a solar metallicity of  $Z = 0.01524$ , [Bressan et al., 2012](#)). The SF models are from [Gutkin et al. \(2016\)](#), which are based on the latest version of the [Bruzual & Charlot \(2003\)](#) stellar population synthesis models, while the AGN models are drawn from [Feltre et al. \(2016\)](#). All models have a fixed hydrogen density ( $n_{\text{H}}$ ; in this case  $10^3 \text{ cm}^{-3}$  for AGN and  $10^2 \text{ cm}^{-3}$  for SF models) and dust-to-heavy-element mass ratio (here,  $\xi_{\text{d}} = 0.3$ ). The SF models are shown for different values of ionisation parameter  $U$ ,  $\log_{10} U \in \{-4, -3, -2, -1\}$ , while the grids of narrow-line region AGN emission shown also have a varying  $\alpha$  (ranging from  $-2.0$  to  $-1.2$ ), the power-law index of the specific luminosity  $S_{\nu} \propto \nu^{\alpha}$  at rest-frame UV wavelengths,  $\lambda_{\text{emit}} \leq 2500$ . We note that the results do not change significantly under different combinations of parameters  $n_{\text{H}}$ ,  $\xi_{\text{d}}$ . The same is true for our assumption about the maximum electron density to establish the C III doublet flux (see

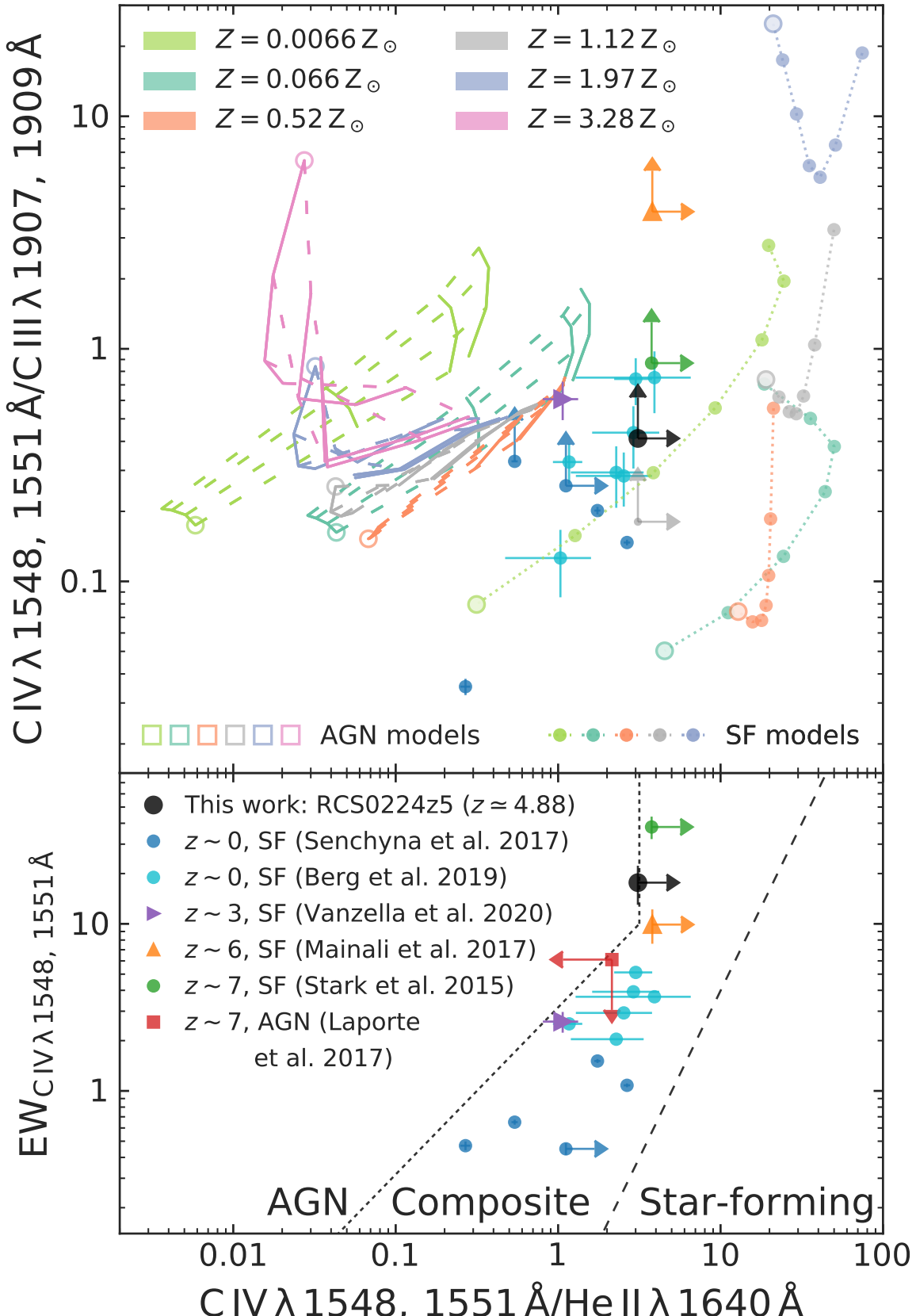


**Figure 2.2** Top panel: line ratio of  $CIV/CIII$  versus  $CIV/HeII$ . The photoionisation models show predictions for nebular emission (indicated as star-forming or SF; models from Gutkin et al., 2016) and narrow-line region AGN emission (models from Feltre et al., 2016); for both, see the description in the text for details. The black and grey measurements show upper limits on the line ratios for RCS0224z5 assuming a maximum electron density of  $n_e \leq 10^3 \text{ cm}^{-3}$  and  $10^5 \text{ cm}^{-3}$  respectively (shifting the ratio by 0.36 dex, see Sect. 2.3.1), both strongly rejecting AGN model predictions. Bottom panel: a UV diagnostic comparison of the rest-frame EW of  $CIV$  with the  $CIV/CIII$  ratio (from Hirschmann et al., 2016).

Sect. 2.3.1), as shown by the light grey measurement (reflecting a maximum of  $n_e \leq 10^5 \text{ cm}^{-3}$  instead of  $10^3 \text{ cm}^{-3}$ ; see Sect. 2.3.1).

A confirmed LyC-emitting galaxy at  $z \simeq 3.21$ , Ion2, is shown for comparison (de Barros et al., 2016; Vanzella et al., 2016, 2020); interestingly, its line ratios indicate a composite nature even though its spectral features in the UV have been attributed to young, massive stars (Vanzella et al., 2020). Also shown are two additional galaxies, at redshifts 6.11 (Stark et al., 2015) and 7.045 (Mainali et al., 2017) which are presumably similar to RCS0224z5, with low mass and a hard ionising radiation field found to be more likely originating from a metal-poor stellar population instead of an AGN. For these galaxies, and for RCS0224z5, the  $2\sigma$  upper limits strongly reject all possibilities of pure AGN models.

The photoionisation models by Gutkin et al. (2016) and Feltre et al. (2016) are coupled to cosmological simulations by Hirschmann et al. (2019) to design BPT-like UV diagnostics to differentiate star-forming galaxies from AGN. These diagnostics are specifically designed to provide an accurate classification over a wide range of redshifts ( $0 < z \lesssim 6$ ). Their diagnostic mapping the EW of C IV against the C IV/He II ratio is shown in the bottom panel of Fig. 2.2. We compare our measurement with local star-forming galaxies with extreme emission lines, that can therefore be seen as analogues of high-redshift galaxies: a sample selected through He II  $\lambda 4687$  emission (implying a hard ionising spectrum; see Senchyna et al., 2017), and a sample of galaxies selected for high-EW [O III]  $\lambda 5008$  emission (among other criteria; Berg et al., 2019a). We show the high-redshift star-forming galaxies and mentioned above and, in contrast, a  $z = 7.149$  galaxy showing evidence for AGN activity (Laporte et al., 2017). The constraints on these high-redshift galaxies are in agreement with respectively the star formation and AGN models. However, there is a noticeable difference in their line ratios relative to the combined sample of low-redshift ‘analogues’.

From these diagnostics, we conclude that there is no strong AGN activity present in RCS0224z5 and the emission is likely produced in H II regions. This finding agrees with Smit et al. (2017), who concluded that the C IV emission is likely nebular in origin, based on the ‘clumpy’ C IV morphology (as opposed to centrally concentrated emission). Instead, a young (1-3 Myr), metal-poor stellar population likely has to account for the hard radiation field required for the C IV emission, providing a considerable contribution of photons reaching energies of at least 47.9 eV. This fits into the picture of the prevalence of extreme line emitters in the early Universe – both more common and more extreme than any known local analogues – and accompanying hard radiation fields that has emerged recently (e.g. Smit et al., 2014, 2015; Stark et al., 2015; Mainali et al., 2017; Hutchison et al., 2019).

### 2.4.2 The $[\text{Ne III}]/[\text{O II}]$ line ratio as an ionisation and metallicity diagnostic alternative to $[\text{O III}]/[\text{O II}]$

Neon is an  $\alpha$  element, produced by heavy stars ( $M \gtrsim 8 M_{\odot}$ ) in their carbon burning cycle and ultimately type II supernovae, and therefore tightly matches oxygen in abundance (Maiolino & Mannucci, 2019, , and references therein). Moreover,  $[\text{Ne III}]$  and its isoelectronic equivalent  $[\text{O III}] \lambda 5008$  ( $[\text{O III}]$ ) have a similarly high ionisation potential (41.0 and 35.1 eV, respectively), meaning the luminosity ratio of  $[\text{Ne III}]$  and the low-ionisation  $[\text{O II}] \lambda 3727, 3730$  doublet ( $[\text{O II}]$ ) is a powerful diagnostic of the ionisation parameter, similar to  $[\text{O III}]/[\text{O II}]$  (Pérez-Montero et al., 2007; Levesque & Richardson, 2014; Maiolino & Mannucci, 2019). The observed relationship between metallicity and ionisation parameter also makes it a metallicity diagnostic, albeit indirectly (causing it to exhibit a significant amount of scatter; see Nagao et al., 2006; Maiolino et al., 2008): metal-poor systems are expected to have a high  $[\text{Ne III}]/[\text{O II}]$  ratio.

The fact that  $[\text{Ne III}]$  and  $[\text{O II}]$  have both similar and short wavelengths gives the  $[\text{Ne III}]/[\text{O II}]$  diagnostic two distinct advantages over the widely used  $[\text{O III}]/[\text{O II}]$  ratio: it is practically insensitive to dust attenuation, and it can be detected at higher redshifts with ground-based near-infrared instruments (Levesque & Richardson, 2014). The former has long been exploited (e.g. Hicks et al., 2002), and indeed,  $[\text{Ne III}]$  has been detected several times at  $z \gtrsim 3$ , in combination with  $[\text{O II}]$ : in particular, we will consider here the galaxies Ion2 at  $z \simeq 3.21$ , a confirmed LyC-emitting galaxy (as discussed in Sect. 2.4.1; de Barros et al., 2016; Vanzella et al., 2016, 2020), SMACS J2031.8-4036 at  $z \simeq 3.51$  (Christensen et al., 2012a,b; Patrício et al., 2016), GOODSN-17940 at  $z \simeq 4.41$  (Shapley et al., 2017), and LnA1689-2 at  $z \simeq 4.87$  (Troncoso et al., 2014).

#### $[\text{Ne III}]/[\text{O II}]$ evolution over stellar mass and cosmic time

The emission line ratio  $[\text{Ne III}]/[\text{O II}] = 0.46 \pm 0.10$  for RCS0224z5 is shown as a function of stellar mass in Fig. 2.3. To find the stellar mass for images 2 and 3 independent of magnification uncertainties, we follow the derivation of Swinbank et al. (2007), who reported a dynamical mass estimate of  $M_{\text{dyn}} \sim 10^{10} M_{\odot}$  based on the  $[\text{O II}]$  velocity dispersion (via Equation (1) in Erb et al., 2006). We assume a fiducial  $C = 3 \pm 2$  (with high uncertainty to reflect the range of possible values depending on mass distribution and velocity field, see Erb et al., 2006), and our measured  $[\text{O II}]$  line width of  $\sigma_{[\text{O II}]} = 151 \pm 30$  km/s within  $r = 2$  kpc (following Swinbank et al., 2007). We then take the typical stellar mass fraction of  $z \sim 1$ -2 star-forming galaxies of  $27 \pm 5\%$ , reflecting the range 22-32% reported by Stott et al. (2016, ; see also Wuyts et al. 2016), to derive a stellar mass of  $(9 \pm 7) \times 10^9 M_{\odot}$ . We note that with *HST* photometry of image 1 (high magnification uncertainties prevent us from using the incomplete images 2 and 3), we derive a stellar mass of  $4_{-3}^{+14} \times 10^8 M_{\odot}$ , using the FAST code (Kriek et al., 2009), assuming a constant star formation rate (SFR), a Chabrier (2003) IMF, a minimum age of  $10^7$  yr (the

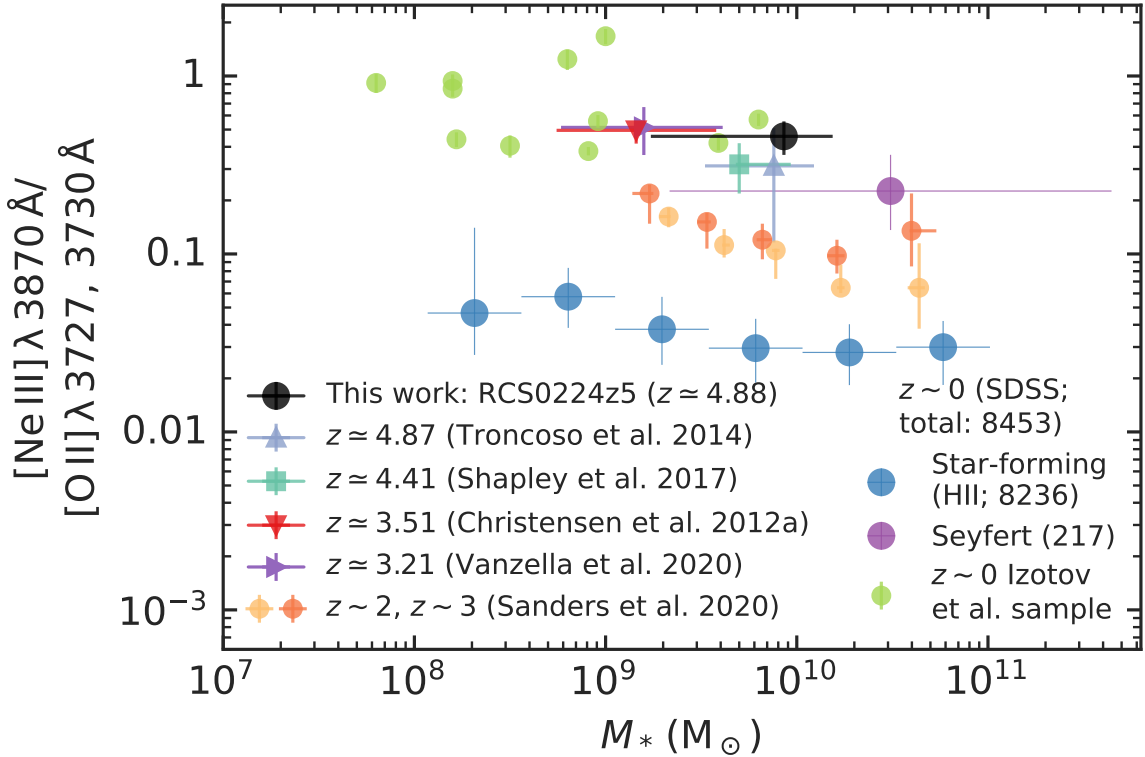


**Figure 2.3** [Ne III]/[O II] ratio of selected SDSS galaxies in bins of stellar mass (star-forming galaxies in blue, Seyfert in purple), as well as measurements of local LyC leakers (Izotov et al. sample). Binned samples at  $z = 2.3$  and  $z = 3.3$  from the MOSDEF survey (Sanders et al., 2021) and the LyC-leaking galaxy Ion2 at  $z \approx 3.21$  (Vanzella et al., 2020) are shown as a reference at intermediate redshift. At the very highest redshift for which measurements of [Ne III]/[O II] are currently possible, we include three star-forming galaxies, at  $z \approx 3.51$ ,  $z \approx 4.41$  and  $z \approx 4.87$  (Christensen et al., 2012a; Shapley et al., 2017; Troncoso et al., 2014, , respectively; see text), and RCS0224z5. A tentative trend emerges, spanning nearly two orders of magnitude in the [Ne III]/[O II] ratio. Star-forming galaxies at  $z \sim 0$  have a ratio of  $\sim 0.01$  (with little scatter), whereas the ratio is significantly increased at higher redshift,  $\sim 0.1$  at  $z \sim 2$ - $3$ . The trend culminates at  $z \sim 5$ : the ratio of RCS0224z5 ( $\sim 0.6$ ), seemingly typical based on this trend, is comparable to that of local LyC leakers, which are clear outliers compared to the general  $z \sim 0$  galaxy population.

maximum age equal to the age of the universe at  $z = 4.88$ ), an SMC dust law, the [Bruzual & Charlot \(2003\)](#) stellar libraries, and a metallicity of  $Z = 0.2 \text{ Z}_\odot$ . This estimate is marginally lower, but consistent within the uncertainty of the stellar mass obtained from the dynamical mass estimate.

Furthermore, the  $\text{SFR}_{[\text{O II}]}$  of  $12 \pm 2 \text{ M}_\odot \text{ yr}^{-1}$  measured for image 2 and 3 by [Swinbank et al. \(2007\)](#) – combined with the stellar mass estimated from the dynamical mass – places RCS0224z5 just under on the main sequence at its redshift (e.g. [Salmon et al., 2015](#), ; a lower stellar mass, as suggested by the SED modelling, would shift it onto the main sequence). This supports the hypothesis that RCS0224z5 is a typical  $z \sim 5$  star-forming galaxy.

To put our measurements of the near-UV [Ne III] and [O II] lines into perspective, we turn to a large observational sample of nearby galaxies from the Sloan Digital Sky Survey Data Release 7 (SDSS DR7; [Abazajian et al., 2009](#)), retrieving line fluxes from the MPA-JHU emission line catalogue for 827,640 unique sources.<sup>3</sup> A detailed description of the selection procedure for the galaxies used here is given in Sect. B.2. The [Ne III]/[O II] ratio of these nearby galaxies are shown in bins of stellar mass (for bins with at least 25 galaxies), for the two main classes (star-forming and Seyfert; see Sect. B.2). Additionally, we compare these to local LyC-leaking galaxies; in particular, we will consider a sample compiled from [Izotov et al. \(2016a,b, 2018a,b\)](#); [Gazagnes et al. \(2020\)](#); [Guseva et al. \(2020\)](#), together simply the [Izotov et al.](#) sample hereafter. Finally, individual measurements of the aforementioned high-redshift galaxies at  $z \simeq 3.21, 3.51, 4.41, 4.87$  ([Vanzella et al., 2020](#); [Christensen et al., 2012a](#); [Shapley et al., 2017](#); [Troncoso et al., 2014](#), , respectively) are shown.

Fig. 2.3 illustrates that RCS0224z5 has a [Ne III]/[O II] ratio consistent with LyC leakers (both those at low redshift and Ion2 at  $z \simeq 3.21$ ), and nearly two orders of magnitude higher than local star forming galaxies with the same mass. This agrees with recent findings of enhanced [Ne III]/[O II] ratios in star-forming galaxies at  $z \sim 2$  ([Zeimann et al., 2015](#); [Jeong et al., 2020](#)). Moreover, this is in agreement with the expectation that [Ne III]/[O II] is a proxy of [O III]/[O II], and that RCS0224z5 might have a high LyC escape fraction, as discussed further below (Sect. 2.4.3).

### [Ne iii]/[O ii] as a proxy for the ionisation state of the ISM

As evidenced by its tight correlation with [O III]/[O II] in local galaxies (e.g. [Jeong et al., 2020](#)), the [Ne III]/[O II] ratio is a robust tracer of the ionisation parameter. Previous studies have proved the strong similarity between the [Ne III]/[O II] and [O III]/[O II] ratios theoretically; however, their quantitative predictions did not quite match observations, which is thought to be due to the modelled ionising spectra being insufficiently hard ([Levesque & Richardson, 2014](#)). We therefore construct an empirical relationship here by exploiting the statistics of

---

<sup>3</sup>The catalogue is available at <https://www.mpa-garching.mpg.de/SDSS/DR7/>, while a description of the relevant methods used to compile it can be found in [Tremonti et al. \(2004\)](#).

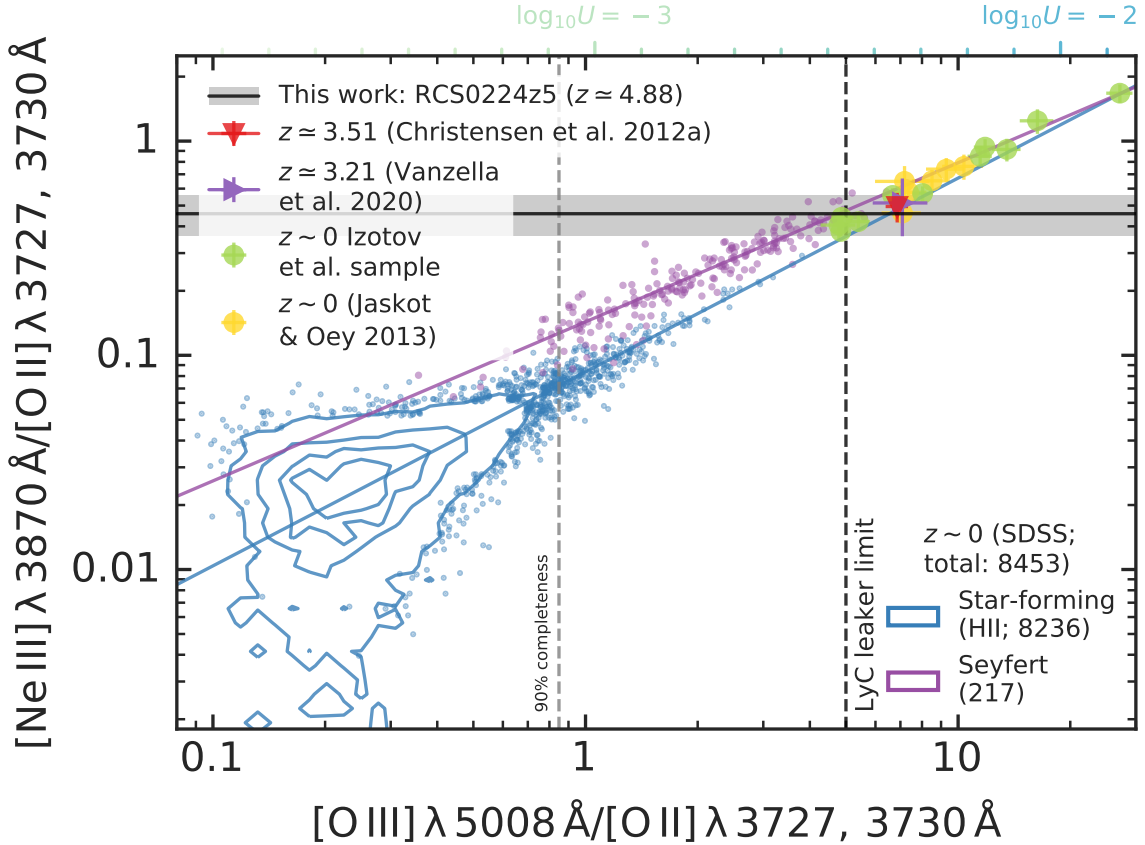


**Figure 2.4** Correlation between the [Ne III]/[O II] and [O III]/[O II] line ratios of SDSS galaxies (star-forming galaxies in blue, Seyfert in purple). Also shown are Ion2 at  $z \approx 3.21$  (Vanzella et al., 2020), SMACS J2031.8-4036 at  $z \approx 3.51$  (Christensen et al., 2012a), the LyC leakers from the Izotov et al. sample, as well as 6 extreme “Green Pea” galaxies from Jaskot & Oey (2013). The vertical grey dashed line shows the completeness limit of 90%, while the fiducial limit ratio of  $[O\text{ III}]/[O\text{ II}] \geq 5$  used to characterise LyC leakers is shown by the vertical black dashed line (see text for details on both). Ionisation parameter values of  $\log_{10} U = -3, -2$  are indicated by vertical blue lines (see Eq. (2.2), derived by Díaz et al., 2000). Direct measurements of Ion2 and SMACS J2031.8-4036 suggest the correlation between [Ne III]/[O II] and [O III]/[O II] seen in local galaxies holds well at higher redshift. Both these sources and RCS0224z5, shown by the black line with grey uncertainty, have a high ionisation parameter compared to local galaxies, similar to that of LyC-leaking systems, but may very well be typical examples at high redshift as they do not seem to be as extreme outliers compared to their contemporaries (Fig. 2.3).

## 2.4 Discussion

---

SDSS. In Fig. 2.4, the distributions of  $[\text{Ne III}]/[\text{O II}]$  and  $[\text{O III}]/[\text{O II}]$  line ratios are shown for two classes of SDSS galaxies (star-forming and Seyfert; see Sect. B.2). The LyC leakers from the Izotov et al. sample are again shown for comparison, along with six other local galaxies selected for extreme  $[\text{O III}]$  emission (“Green Peas”, or GPs; Jaskot & Oey, 2013), as well as the high-redshift galaxies Ion2 and SMACS J2031.8-4036 (Vanzella et al., 2020; Christensen et al., 2012a, , respectively). The fiducial limiting ratio of  $[\text{O III}]/[\text{O II}] \geq 5$  used to characterise LyC leakers is shown by a vertical dashed black line.

To fit the relationship from the SDSS sample, we first define the completeness of a given  $[\text{O III}]/[\text{O II}]$  bin to be the fraction of galaxies contained in that bin with a  $[\text{Ne III}]$  SNR higher than 5. At values of  $[\text{O III}]/[\text{O II}] \lesssim 1$ , this completeness drops significantly. Since we require a highly significant  $[\text{O II}]$  detection ( $\text{SNR} > 30$ , see Sect. B.2), the uncertainty on the  $[\text{Ne III}]/[\text{O II}]$  ratio is dominated by that of  $[\text{Ne III}]$ , explaining the scattered cloud of points in contrast to the tight correlation seen at  $[\text{O III}]/[\text{O II}] > 1$ . As  $[\text{Ne III}]$  is the weakest out of the three lines considered here (Maiolino & Mannucci, 2019), we fit the relation taking into account uncertainties on the  $[\text{Ne III}]/[\text{O II}]$  ratio only. For star-forming galaxies we exclude points in the region where the completeness fails to meet 90% ( $[\text{O III}]/[\text{O II}] < 0.849$ ; grey dashed line in Fig. 2.4). For the remaining 272 points, we find a Spearman’s rank correlation coefficient (measured in log-log space) of  $\rho_S = 0.87$ , indicating a strong positive correlation. Moreover, the resulting fit captures the behaviour at both the low and high  $[\text{O III}]/[\text{O II}]$  ratios well: extrapolating to lower  $[\text{O III}]/[\text{O II}]$  ratios the low-SNR SDSS data are scattered around the relation symmetrically, while extrapolating to higher  $[\text{O III}]/[\text{O II}]$  ratios the extreme ratios of GP galaxies (not included in the fit) are consistent with this trend. The fit for star-forming galaxies is given by

$$\log_{10} \left( \frac{[\text{Ne III}]}{[\text{O II}]} \right) = 0.9051 \log_{10} \left( \frac{[\text{O III}]}{[\text{O II}]} \right) - 1.078 \quad (2.1)$$

For example, the proposed line ratio above which a significant fraction of sources might be leaking LyC photons,  $[\text{O III}]/[\text{O II}] \geq 5$ , (e.g. Izotov et al., 2016b,a) corresponds to  $[\text{Ne III}]/[\text{O II}] \geq 0.36$ . Furthermore, with this empirical relationship, we can translate diagnostics based on the  $[\text{O III}]/[\text{O II}]$  ratio, e.g. a diagnostic for the ionisation parameter (derived from single-star photoionisation models, see Díaz et al., 2000),

$$\log_{10} U = 0.80 \log_{10} \left( \frac{[\text{O III}]}{[\text{O II}]} \right) - 3.02 \quad (2.2)$$

Vertical blue lines indicate values of  $\log_{10} U = -3, -2$  in Fig. 2.4. Combining Eqs. (2.1) and (2.2), we derive

$$\begin{aligned}\log_{10} U &= 0.80 \frac{\log_{10} ([\text{Ne III}]/[\text{O II}]) + 1.078}{0.9051} - 3.02 \\ &= 0.884 \log_{10} \left( \frac{[\text{Ne III}]}{[\text{O II}]} \right) - 2.07\end{aligned}\quad (2.3)$$

In the case of RCS0224z5, we find an ionisation parameter of  $\log_{10} U = -2.37 \pm 0.08$ . Given its derivation from the [Ne III]/[O II] ratio, we again note this is likely not an extreme case at its redshift (Fig. 2.3, and see similar estimates of  $U$  at  $z \sim 7\text{-}8$  in Stark et al., 2017), but a high ionisation parameter compared to local galaxies, similar to that of LyC-leaking systems (the limit of  $[\text{O III}]/[\text{O II}] \geq 5$  translates to  $\log_{10} U = -2.46$ ).

However, the [Ne III]/[O II] ratio is also an indirect tracer of the gas metallicity (being mostly anti-correlated with metallicity). The fact that RCS0224z5 (along with GOODSN-17940) has [Ne III]/[O II] much higher than local galaxies, and hence much lower metallicity, is also likely linked to the redshift evolution of the mass-metallicity relation (MZR). This is illustrated in Fig. 2.3 where binned samples are shown at intermediate redshifts,  $z = 2.3$  and  $z = 3.3$  (measurements from the MOSDEF survey; Sanders et al., 2021). The tentative evolutionary trend of the [Ne III]/[O II] ratio with redshift seen in Fig. 2.3 has indeed been verified to approximately reproduce the MZR as observed with a variety of metallicity tracers (e.g. Maiolino et al., 2008). The next section will discuss the diagnosticity of [Ne III]/[O II] specifically regarding metallicity in further detail.

### Tracing metallicity with [Ne iii]/[O ii]

By virtue of its correlation with the ionisation parameter, the [Ne III]/[O II] ratio is also an indirect tracer of the metallicity. In the following we discuss the former aspect in greater detail, albeit with the caveat that the ratio is a more robust diagnostic for the ionisation parameter than for metallicity.

By using the metallicity diagnostic relation for [Ne III]/[O II] from Bian et al. (2018), calibrated with local analogues of high-redshift galaxies, we obtain  $12 + \log (\text{O/H}) = 8.01^{+0.21}_{-0.21}$  for RCS0224z5, where we have included a 0.2 dex systematic calibration uncertainty (see e.g. Nagao et al. 2006). This corresponds to roughly 20% of the solar metallicity:  $Z = 0.21^{+0.13}_{-0.08} Z_\odot$ .<sup>4</sup> The galaxies at  $z \sim 4\text{-}5$  with [Ne III] and [O II] measurements are clearly characterised by significantly higher line ratios (Fig. 2.3), and hence higher ionisation parameters than  $z \sim 3.5$  galaxies. Using the (uncertain) strong-line calibration, we can indirectly infer they have lower metallicities too, which would confirm that they do follow the general redshift evolution of metallicity.

---

<sup>4</sup>We adopt a solar oxygen abundance of  $12 + \log (\text{O/H})_\odot = 8.69$  (Asplund et al., 2009).

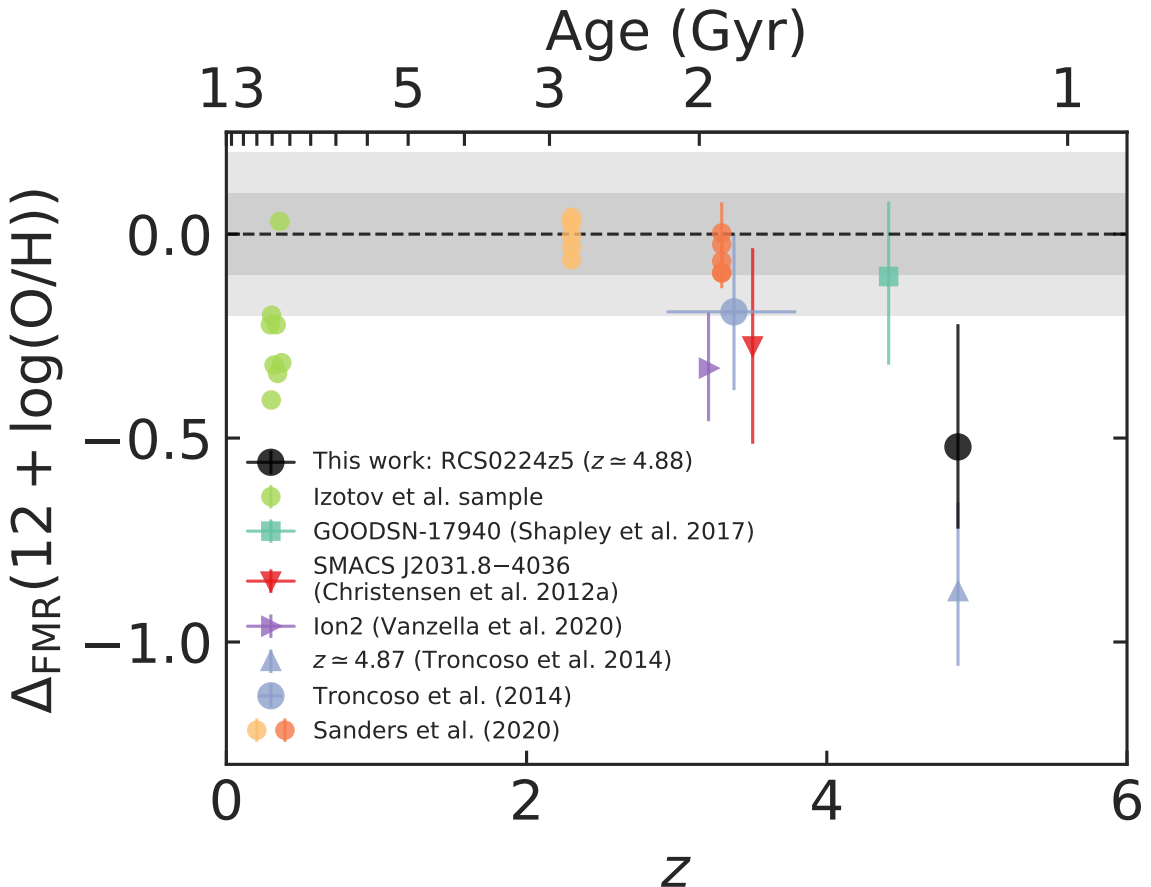


**Figure 2.5** Offsets from the Fundamental Metallicity Relation (FMR), given by the inferred metallicity minus the one derived from the FMR. Intrinsic uncertainty of the FMR (which varies with both stellar mass and SFR) is indicated by the grey shaded regions, the darker region typical for galaxies at high mass and low SFR, the lighter region for galaxies at low mass and high SFR (for details, see Curti et al., 2020). At low redshift, the LyC leakers from the Izotov et al. sample are shown. Samples binned by stellar mass at  $z = 2.3$  and  $z = 3.3$  from the MOSDEF survey (Sanders et al., 2021) are shown, as well as a binned sample of 31 galaxies at  $z \sim 3\text{--}4$  from the AMAZE and LSD surveys, presented in Troncoso et al. (2014). LnA1689-2 is excluded from the latter and instead shown individually at  $z \simeq 4.87$ , as are Ion2 at  $z \simeq 3.21$  (Vanzella et al., 2020), SMACS J2031.8-4036 at  $z \simeq 3.51$  (Christensen et al., 2012a), GOODSN-17940 at  $z \simeq 4.41$  (Shapley et al., 2017). Galaxies at the highest redshift seem to show a trend towards negative differences, i.e. metallicities smaller than expected from the FMR.

However, one should take into account that the metallicity of star-forming galaxies also shows a secondary dependence on SFR that, together with the primary dependence on mass, is dubbed Fundamental Metallicity Relation (FMR, see e.g. [Mannucci et al. 2010](#); see also a review in [Maiolino & Mannucci 2019](#)). This secondary dependence is thought to result from a more fundamental relation with the gas content ([Bothwell et al., 2013, 2016a,b](#)) and ascribed primarily to the accretion of near-pristine (or low-metallicity) gas which increases the gas content and dilutes the metallicity; the increased gas content also results into an increased SFR through the Kennicutt–Schmidt relation, which gives the observed anti-correlation between SFR and metallicity. Once this secondary dependence is taken into account then the redshift evolution of the metallicity is essentially absent, at least out to  $z\sim 2.5$  ([Mannucci et al., 2010](#); [Cresci et al., 2019](#)). Some deviation from the FMR was claimed at  $z>3$  ([Troncoso et al., 2014](#)), but more recently [Sanders et al. \(2021\)](#) have shown that their sample at  $z\sim 3$  follows the same FMR as local galaxies if metallicities are measured through the [Bian et al. \(2018\)](#) calibration.

We assess whether RCS0224z5 and other high-redshift galaxies, as well as the local LyC leakers from the [Izotov et al.](#) sample, follow the FMR, carefully revisiting all measurements in a consistent way, as discussed in the following. At high redshift, we consider galaxies at  $z>2$  from [Sanders et al. \(2021\)](#) and [Troncoso et al. \(2014\)](#), as well as the three galaxies at  $z>4$  with detections of [Ne III] and [O II] already discussed in the previous section. For RCS0224z5 we use the stellar mass of images 2 and 3 obtained from the dynamical mass,  $(9\pm7)\times10^9 M_\odot$  (including uncertainties on  $C$ , the stellar mass fraction, and  $\sigma_{[O\,II]}$ , discussed in Sect. 2.4.2), and the SFR of images 2 and 3,  $12\pm2 M_\odot\,\text{yr}^{-1}$ , as reported by [Swinbank et al. \(2007\)](#). We also include the two individual galaxies at  $z\sim 3$  with [Ne III] and [O II] measurements discussed in the previous section. We use the same high-redshift calibration from [Bian et al. \(2018\)](#) for all high-redshift galaxies. We then consider  $\Delta_{\text{FMR}}(12+\log(\text{O/H}))$ , the deviation of the measured metallicity from the local FMR, defined as

$$\begin{aligned}\Delta_{\text{FMR}}(12+\log(\text{O/H})) = & 12+\log(\text{O/H}) \\ & - (12+\log(\text{O/H}))_{\text{FMR}}.\end{aligned}$$

Here, we describe the metallicity predicted by the local FMR,  $(12+\log(\text{O/H}))_{\text{FMR}}$ , as a function of stellar mass and SFR through Equation (5) in [Curti et al. \(2020\)](#). The best-fit parameters obtained by [Curti et al.](#) adopt  $T_e$ -based metallicity calibrations (as [Bian et al., 2018](#), , but based on the full SDSS dataset). Uncertainties are estimated by independently varying the input variables ( $M_*$ , SFR) within the  $1\sigma$  uncertainty range and adding the resulting deviations in quadrature. For LyC leakers in the [Izotov et al.](#) sample, we calculate the FMR offset if the metallicity has been reported. We show the resulting deviations from the FMR in Fig. 2.5.

While at  $z\sim 2$  galaxies are fully consistent with the local FMR, at  $z>3$  galaxies start having a larger scatter and tend to be distributed towards lower metallicities with respect to

## 2.4 Discussion

---

the FMR, also depending on the sample. Although the uncertainties are large, RCS0224z5 also shows some mild tension with respect to the local FMR, being more metal poor. Interestingly, the nearby LyC-leaking galaxies exhibit a significant offset in a similar direction. The other galaxy at nearly the same redshift, LnA1689-2 from the [Troncoso et al.](#) sample, likewise deviates from the FMR. Since the FMR is considered a relation describing the smooth evolution of galaxies in near-equilibrium between the inflow and outflow of gas and star formation, these findings may suggest that such young galaxies at  $z \sim 5$  are in an early stage of evolution in which they have not yet reached a steady equilibrium as the more evolved galaxies at lower redshifts, possibly as a consequence of an excess in gas accretion, which results in additional dilution of metals. However, these results should be confirmed with a larger sample of galaxies at  $z > 4$  and by using additional metallicity diagnostics, which will certainly be feasible with *JWST*.

Finally, we note that the estimated metallicity obtained through the  $[\text{Ne III}]/[\text{O II}]$  ratio is significantly higher than the values required in stellar population synthesis models to reproduce the observed C IV EW ( $Z < 0.05 Z_{\odot}$ , as shown in [Smit et al. 2017](#)). This indicates the hardness of the ionising spectrum may currently be underestimated in such models. The lack of ionising photons above 47.9 eV could be accounted for by physics currently not captured in models (e.g. stars stripped in binaries, [Götberg et al., 2019](#)), or it may be explained by a lower stellar iron abundance than derived using the nebular oxygen abundance and assuming solar oxygen-to-iron ratios (O/Fe). A higher oxygen-to-iron is expected in the early Universe compared to local galaxies, given that AGB stars have lifetimes of only a few gigayears and metal enrichment is dominated by supernovae ([Maiolino & Mannucci, 2019](#)). In particular, the discrepancy seems to agree well with the findings of [Steidel et al. \(2016\)](#), who demonstrate that the oxygen-to-iron ratio of their sample of star-forming galaxies at  $z \sim 2.4$  is elevated by a factor of  $\sim 4$  relative to the solar value (i.e. virtually the same enhancement as the ratio between the metallicities discussed here, 20% and 5% solar). While RCS0224z5 appears moderately metal-enriched as measured indirectly with  $[\text{Ne III}]/[\text{O II}]$  (probing the nebular oxygen abundance), stellar atmospheres could be significantly more iron-poor than expected when assuming a solar O/Fe ratio, resulting in an ionising spectrum sufficiently hard to explain the observed C IV EW.

More generally, these results show the potential of  $[\text{Ne III}]$  as a powerful diagnostic, specifically for the study of high-redshift galaxies. Note, however, that the  $[\text{Ne III}]$  line can blend with  $\text{He I } \lambda 3890$ , separated by  $\sim 1500$  km/s, in low-resolution spectra ( $R \lesssim 200$ ). This effect becomes more prominent when the lines are broadened, for example with a significant contribution from the broad-line region of an AGN (e.g. [Malkan et al., 2017](#)) – this will not be the case, however, for star-forming systems dominated by narrow nebular emission lines.

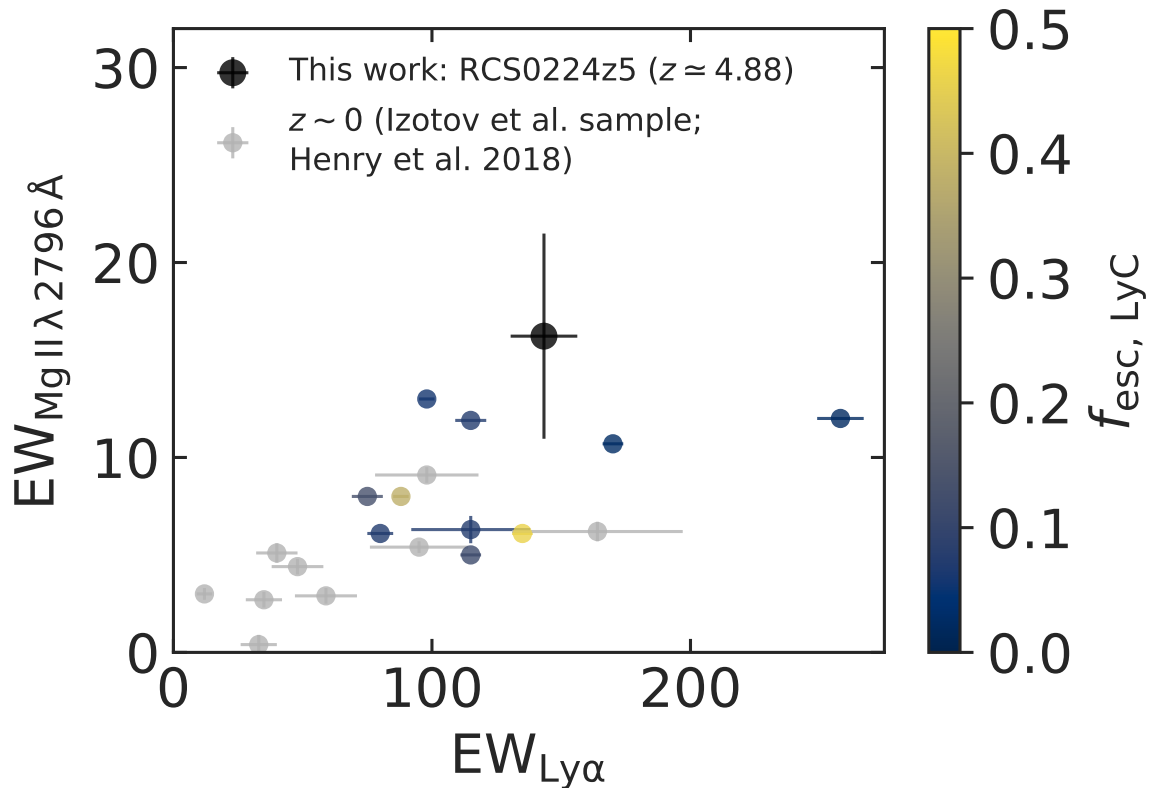


**Figure 2.6** Equivalent widths of Ly $\alpha$  and Mg II  $\lambda$  2796 of RCS0224z5, compared to local extreme emission line galaxies, among which ten LyC-emitting sources (the Izotov et al. sample and Henry et al., 2018, , coloured according to the escape fraction of LyC, if known). The correlation between Ly $\alpha$  and Mg II EWs is one of the indicators that the escape mechanisms of Ly $\alpha$  and Mg II are similar. Moreover, relatively high EWs imply that both Ly $\alpha$  and Mg II escape is comparatively high in RCS0224z5.

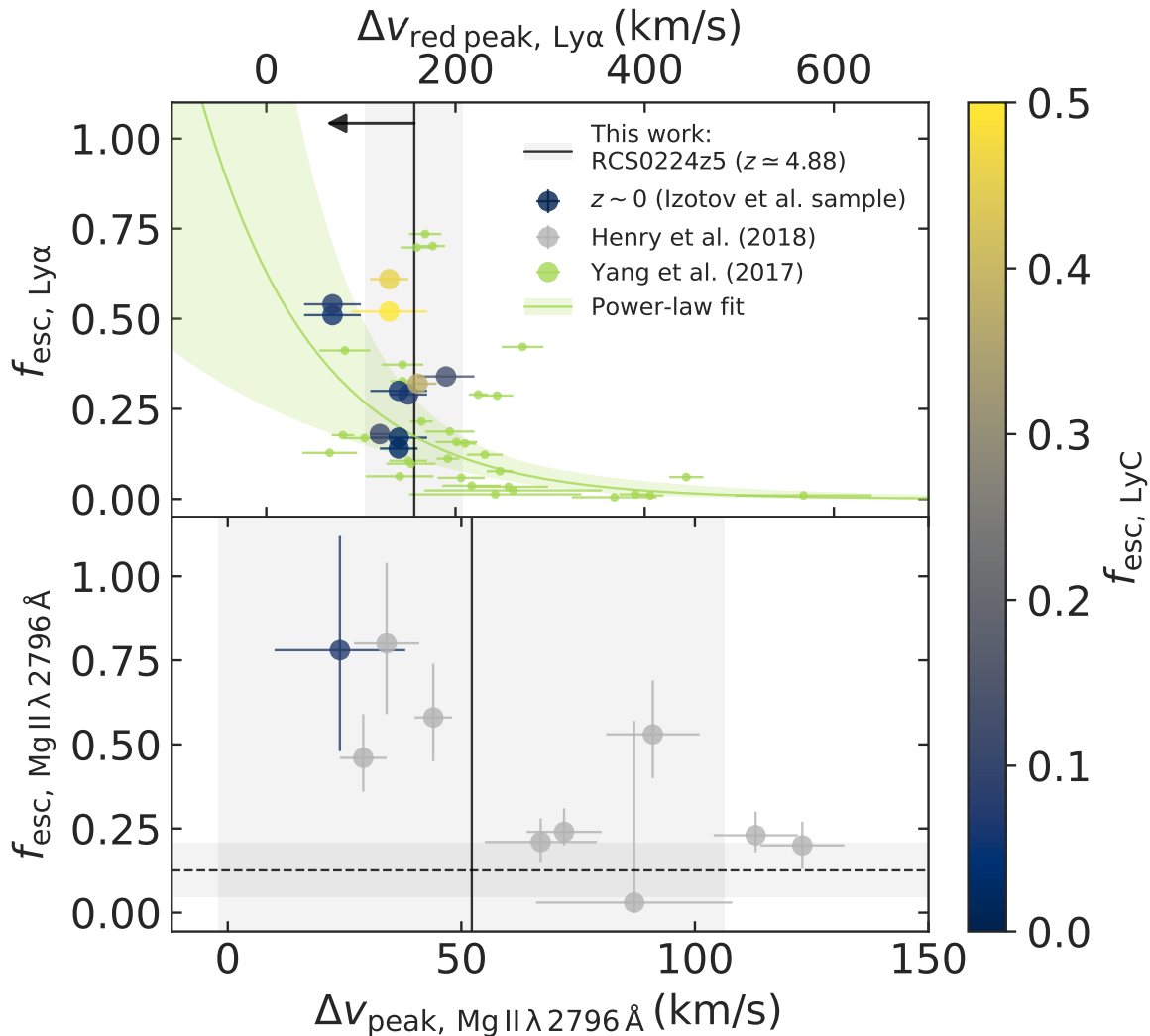


**Figure 2.7** Escape fractions of Ly $\alpha$  radiation (top) and Mg II  $\lambda 2796$  (bottom) compared to the corresponding velocity offsets of Ly $\alpha$  (its red peak; top) and the peak of Mg II  $\lambda 2796$  (bottom), compared to local extreme emission line galaxies. Among these are ten LyC-emitting sources (the Izotov et al. sample and Henry et al., 2018, , coloured according to the escape fraction of LyC, if known). In the top panel, a sample of Green Pea galaxies from Yang et al. (2016, 2017) is shown (the sample consists of 43 galaxies, among which 5 are already contained in the Izotov et al. sample), with a simple power-law fit. Both panels show a similar trend (though with considerable scatter), where a small velocity offset indicates a large escape fraction. The measured velocity offsets of RCS0224z5 (effectively an upper limit in the case of Ly $\alpha$  due to IGM absorption) again suggest relatively high escape fractions, which is supported by the predicted escape fraction of Mg II  $\lambda 2796$  (the horizontal dashed line; see text for details).

### 2.4.3 LyC escape traced by Ly $\alpha$ and Mg II emission

#### Velocity offsets of Ly $\alpha$ and Mg II

Using spatially resolved MUSE spectroscopy, Smit et al. (2017) demonstrated the presence of extended, high-EW Ly $\alpha$  emission, with a narrow, red peak emerging very close to the systemic redshift (defined by [O II]), regardless of position within the Ly $\alpha$  halo. X-shooter has a higher spectral resolution than MUSE at  $\sim 7000$  ( $R \sim 6500$  versus  $R \sim 2700$ , respectively). We fit an asymmetric Gaussian line profile (see e.g. Shibuya et al., 2014) to the Ly $\alpha$  observed in image 1 by X-shooter (see Fig. 2.1). We find a velocity offset of  $\Delta v_{\text{peak}} = 156 \pm 52$  km/s from the systemic redshift (in agreement with Smit et al., 2017), FWHM of  $207 \pm 6$  km/s, and asymmetry factor  $a_{\text{asym}} = 0.32 \pm 0.01$ , indicating a skewed profile with a red wing. The asymmetric Gaussian provides an overall good fit, but does show non-vanishing residuals, particularly at the line peak, as well as the regions around 400 and 1000 km/s. As we lack sufficient angular resolution in the spectrum to study the Ly $\alpha$  line shape in depth, we will not focus on possible interpretations here and instead refer to the extensive discussion in Smit et al. (2017).

The determination of the peak offset can provide interesting constraints on properties of the neutral ISM. In particular, the peak *separation* in a double-peaked Ly $\alpha$  profile (peak offset being the closest alternative to peak separation in the absence of a blue peak<sup>5</sup> in the observed spectrum as a result of absorption in the intervening neutral IGM) is an indicator of resonant scattering of escaping Ly $\alpha$  photons: a higher column density of neutral hydrogen along the path of escape means more scattering, affecting the line profile shape to have its peak appear increasingly further from the systemic velocity at which the photons were produced: only photons far away from resonance (in frequency space), with a resulting low cross section, are able to escape (e.g. Verhamme et al., 2017). In the context of the escape of LyC, which is itself governed by the same distribution of neutral hydrogen, the peak separation has proven to be a solid predictor of LyC escape fractions (Verhamme et al., 2017; Izotov et al., 2018b; Gazagnes et al., 2020). There are other indirect probes of LyC escape, though, which become necessary for application in the EoR, where Ly $\alpha$  (including the red peak) can be fully absorbed, as a result of the broad damping wing (e.g. Dijkstra, 2014). Within this context, Mg II, also a resonant transition in the near UV, presents promising features for high-redshift studies.

We detect Mg II  $\lambda 2796$  as a narrow emission line close to the systemic redshift ( $\sim 52$  km/s, see Fig. 2.1 and Table 2.1), while this feature is commonly seen in absorption in the spectra of local galaxies. Mg II P-Cygni profiles with blueshifted absorption and redshifted emission have been discovered in more distant ( $z \gtrsim 0.5$ ) galaxies, however, where it has been exploited to study galactic outflows (e.g. Weiner et al., 2009; Rubin et al., 2010, 2011; Giavalisco et al., 2011; Erb et al., 2012; Kornei et al., 2013; Bordoloi et al., 2016; Finley et al., 2017). Previous studies of gravitationally lensed galaxies at  $z \sim 1.5$ -2 have also demonstrated several cases of Mg II

---

<sup>5</sup>The velocity offset of the blue peak actually offers the best predictive power (Verhamme et al., 2017).

emission, seen without P-Cygni profiles or evidence for a redshift from the systemic velocity (Pettini et al., 2010; Rigby et al., 2014; Karman et al., 2016).

Nebular emission from H II regions or resonant scattering (of either Mg II or continuum photons) are both plausible sources of Mg II emission. The former scenario is supported by comparing observed Mg II profiles to photoionisation models, while their variety, ranging from narrow, systemic emission to P-Cygni and pure absorption, provides evidence for the latter (Rubin et al., 2010; Erb et al., 2012; Feltre et al., 2018). For RCS0224z5, its narrow line profile observed close to the systemic redshift suggests a nebular origin of the Mg II line and an ISM where little scattering takes place along the line of sight (e.g. due to a very high filling factor of ionised gas).

### The predictive power of Ly $\alpha$ and Mg ii emission for unseen LyC escape processes

Considering the resonant nature of Mg II (and the low ionisation energies of magnesium that make Mg II mainly a tracer of the neutral ISM), various studies have pointed out the resemblance to Ly $\alpha$  (e.g. Henry et al., 2018; Feltre et al., 2018). As a result, Mg II might provide a new way to indirectly but effectively identify sources emitting both Ly $\alpha$  (commonly used as a probe for measuring the conditions of the IGM, see Dijkstra, 2014) and LyC radiation at  $z \gtrsim 6$ , before reionisation is completed (McGreer et al., 2015), where neither may be directly observable as a result of absorption by the neutral IGM. Indeed, Mg II emission has been reported in ten local LyC leakers (Izotov et al., 2016a,b, 2018a,b; Guseva et al., 2020), and in a sample of Green Pea (GP, see also Sect. 2.4.2) galaxies (Henry et al., 2018). In the latter, a correlation between the escape fractions of Mg II and Ly $\alpha$  has been found, which suggests a tentative correlation between the escape fractions of Mg II and LyC. If well established (promising first results have been reported, Chisholm et al., 2020; Matthee et al., 2021), this correlation could allow *JWST* and the generation of Extremely Large Telescopes to reveal the sources beyond (and behind) reionisation, given they can detect a Mg II signal from sources in the EoR. Moreover, Mg II would provide a tool to predict the intrinsic properties of Ly $\alpha$  within galaxies, in order to improve the constraints on the neutral fraction in the IGM derived from the Ly $\alpha$  prevalence in reionisation-era sources (e.g. Schenker et al., 2014; Mason et al., 2018; Pentericci et al., 2018).

Using the measured EW of Mg II  $\lambda 2796$  we compare RCS0224z5 to local LyC leakers and GPs from the Izotov et al. and Henry et al. samples in Fig. 2.6. This figure illustrates the correlation between Ly $\alpha$  and Mg II EWs (although lacking an evident direct relation with LyC escape fraction shown by the colourbar), as would be expected for correlated escape fractions of the two lines.

As discussed in Sect. 2.4.3, the velocity offsets of a resonant emission line can be a proxy for the fraction of escaping photons (i.e. both Ly $\alpha$  and Mg II). Fig. 2.7 therefore compares escape fractions with velocity offsets, respectively Ly $\alpha$  escape as a function of the velocity offset of its red peak, and Mg II  $\lambda 2796$  escape as a function of peak velocity offset of that same line. In the

case of Ly $\alpha$ , an additional sample of Green Pea galaxies from Yang et al. (2016, 2017) is shown for reference (the sample consists of 43 galaxies, among which 5 are already contained in the Izotov et al. sample). The data points show a significant amount of scatter, but the velocity offsets are negatively correlated with the escape fractions. We fit a simple power-law of the form

$$\log_{10} (f_{\text{esc}, \text{Ly}\alpha}) = a\Delta v_{\text{red peak, Ly}\alpha} + b \quad (2.4)$$

where  $a = -0.004^{+0.002}_{-0.002}$  and  $b = -0.20^{+0.40}_{-0.39}$ . For RCS0224z5 specifically, the Ly $\alpha$  velocity offset would result in a corresponding escape fraction of  $f_{\text{esc}, \text{Ly}\alpha} = 0.17^{+0.11}_{-0.07}$ . Since absorption by the intervening IGM could bias the Ly $\alpha$  peak offset redwards, we note its measured velocity offset (and hence the implied Ly $\alpha$  escape fraction) should be considered as an upper (lower) limit. Similarly, the measured velocity offset of Mg II implies a relatively high escape fraction. Even though the offset from the systemic redshift measured with X-shooter is somewhat uncertain (see Sect. 2.3), Mg II is  $\sim 100$  km/s bluewards of Ly $\alpha$ , and  $\sim 40$  km/s bluewards of C IV (all measured on the same X-shooter spectrum), which suggests very little scattering (resulting in P-Cygni profiles) can have taken place, indicating that both Ly $\alpha$  and Mg II escape easily.

Independently, we can estimate the Mg II  $\lambda 2796$  escape fraction. Henry et al. (2018) have demonstrated a tight sequence between the [O III]/[O II] ratio and the intrinsic line flux of Mg II  $\lambda 2796$  relative to [O III]  $\lambda 5008$ . Although [O III] has not been observed directly, we can infer its flux (and the [O III]/[O II] ratio) through the observed [Ne III] and [O II] lines, as discussed in Sect. 2.4.2.

We start with Eq. (2.1), from which we derive an [O III]/[O II] ratio of  $6.6 \pm 1.6$  and hence  $F_{[\text{O III}]} = (8.6 \pm 2.1) \cdot 10^{-16} \text{ erg s}^{-1} \text{ cm}^{-2}$  for RCS0224z5. Again using Eq. (2.1), we can rewrite Equation (1) in Henry et al. (2018) in terms of the [Ne III]/[O II] ratio:

$$\begin{aligned} R_{2796} &= \log_{10} \left( \frac{\text{Mg II } \lambda 2796}{[\text{O III}] \lambda 5008} \right) \\ &= 0.079\omega^2 - 1.04\omega - 0.54 \\ &= 0.0964\nu^2 - 0.941\nu - 1.67, \end{aligned} \quad (2.5)$$

where

$$\omega = \log_{10} \left( \frac{[\text{O III}]}{[\text{O II}]} \right), \nu = \log_{10} \left( \frac{[\text{Ne III}]}{[\text{O II}]} \right).$$

The first two lines of Eq. (2.5) give the definition of  $R_{2796}$  and its fitted dependence on the [O III]/[O II] ratio given in Equations (1) and (3) in Henry et al. (2018). The final line follows from inserting Eq. (2.1) in this work.

For RCS0224z5, we find  $R_{2796} = -1.34 \pm 0.22$ , taking into account a  $\sim 0.2$  dex scatter in Eq. (2.5) (see Henry et al., 2018), which translates to a predicted intrinsic Mg II  $\lambda 2796$  flux of  $(5.0 \pm 1.5) \cdot 10^{-18} \text{ erg s}^{-1} \text{ cm}^{-2}$ . The predicted escape fraction is then  $f_{\text{esc}, \text{Mg II } \lambda 2796} = 0.13 \pm 0.08$ , as indicated by the horizontal dashed line in Fig. 2.7. We furthermore note  $R_{2796}$  can also be

translated to the ratio of Mg II  $\lambda 2796$  over [O II],  $R'_{2796}$  (which however will likely have a larger intrinsic scatter):

$$\begin{aligned} R'_{2796} &= R_{2796} + \omega = \log_{10} \left( \frac{\text{Mg II } \lambda 2796}{[\text{O II}] \lambda 3727, 3730} \right) \\ &= 0.079\omega^2 - 0.04\omega - 0.54 \\ &= 0.0964\nu^2 - 0.164\nu - 0.476. \end{aligned} \quad (2.6)$$

Finally, we will briefly discuss the feasibility of observing Mg II in EoR sources. Simulations<sup>6</sup> of the near-infrared spectrograph on *JWST* (NIRSpec), point out that for an (intrinsically) relatively faint object like RCS0224z5, whose UV continuum would be observed as  $m_{\text{UV}} \sim 27.4$  mag at  $z = 7$ , detecting Mg II spectroscopically would be challenging (see Sect. B.3 for a detailed description). Low-resolution ( $R \sim 100$ ) *JWST*/NIRSpec observations will not resolve the doublet or provide velocity offset information. Only a very deep ( $\sim 10$  h) exposure with *JWST*/NIRSpec at medium spectral resolution would likely yield a significant detection at sufficient spectral resolution to resolve the doublet for typical  $z \sim 7$  EoR galaxies, unless the observed Mg II flux is substantially enhanced (either intrinsically, e.g. by a luminous starbursting galaxy, or externally by gravitational lensing). In addition, spectroscopic observations of Mg II could be performed with Extremely Large Telescopes out to redshift  $z \lesssim 7$  in the *K*-band, in order to unlock the potential of Mg II not only for spectroscopic redshift confirmation, but also as an indirect tracer of Ly $\alpha$  and LyC properties of galaxies in the EoR.

## 2.5 Summary

We have presented new X-shooter and SINFONI observations of a  $30\times$  magnified galaxy at  $z \simeq 4.88$ , RCS0224z5. Only three sources at  $z \gtrsim 5$  are known with this lensing magnification, and at the same time its redshift places RCS0224z5 just below the observational limit for accessing the bluest rest-frame optical emission lines from the ground ([O II] and [Ne III], other lines have already shifted into the mid-infrared). This particular source has been shown to exhibit widespread, high equivalent width C IV  $\lambda 1549$  emission, suggesting it is a unique example of a metal-poor galaxy, with a hard radiation field and high LyC production efficiency  $\xi_{\text{ion}}$ , likely representing the galaxy population that is responsible for cosmic reionisation. By virtue of its lensing magnification and redshift, RCS0224z5 is thus a unique “Rosetta Stone” object that could help bridge the gap in our understanding between galaxies in the local and very early Universe. We summarise our findings as follows:

- We rule out the presence of strong AGN activity in the source, based on UV BPT-like diagnostics. Instead, a young (1-3 Myr), metal-poor stellar population is likely responsible

---

<sup>6</sup> *JWST* Exposure Time Calculator: <https://jwst.etc.stsci.edu>.

for the hard radiation field required for the C IV emission, providing a considerable contribution of photons reaching energies of at least 47.9 eV.

- We present the detection of [Ne III] (the highest redshift this line has been observed at) and discuss the potential of the [Ne III]/[O II] line ratio as a high-redshift diagnostic for the ionisation parameter (and metallicity, albeit indirect). The measured ratio of RCS0224z5,  $[\text{Ne III}]/[\text{O II}] = 0.46 \pm 0.10$ , corresponding to a likely ionisation parameter of  $\log_{10} U = -2.37 \pm 0.08$ , is similar to local galaxies that have been confirmed to be leaking LyC radiation, and about an order of magnitude higher than local star-forming galaxies.
- When using [Ne III]/[O II] as metallicity tracer – indirectly, since the line ratio principally correlates with the ionisation parameter – we estimate that RCS0224z5 has a gas metallicity of roughly 20% of the solar value ( $12 + \log(\text{O/H}) = 8.01^{+0.21}_{-0.21}$ ), which is in mild tension with what is expected from the Fundamental Metallicity Relation (FMR). The only other galaxy known at a similar redshift ( $z \sim 5$ ) for which [Ne III] is detected shows a similar displacement in metallicity, as do nearby LyC leakers. Since the FMR is considered a relation describing the smooth chemical evolution of galaxies, in which galaxies are in near-equilibrium between star formation and gas inflow and outflow, the deviation of these two galaxies at  $z \sim 5$  suggests that primeval galaxies (and rare, LyC-leaking galaxies in the local Universe) might be out of equilibrium by being subject to an excess of gas accretion, resulting in an excess of metallicity dilution. However, more measurements at this cosmic epoch are certainly needed to verify this trend.
- Our detection of Mg II in emission, the highest EW emission line observed in this source after Ly $\alpha$  (and the highest redshift detection to date), demonstrates its potential for several applications. Firstly, it can simply act as a spectroscopic redshift confirmation at high redshift – especially in the EoR (at  $z \gtrsim 6$ ), where Ly $\alpha$  will be absorbed by the neutral IGM. Secondly, since the escape of Mg II correlates with that of Ly $\alpha$  (Henry et al., 2018), it might provide a new way to indirectly but effectively identify leaking LyC radiation in the same sources during an epoch when the Universe is opaque also to LyC photons. Finally, detecting Mg II in these sources would provide a tool to predict the intrinsic properties of Ly $\alpha$  within galaxies, allowing improved constraints on the neutral fraction in the IGM derived from the Ly $\alpha$  prevalence.

## REFERENCES

---

- Abazajian K. N., et al., 2009, [ApJS](#), **182**, 543
- Arrigoni Battaia F., Hennawi J. F., Cantalupo S., Prochaska J. X., 2016, [ApJ](#), **829**, 3
- Arrigoni Battaia F., Hennawi J. F., Prochaska J. X., Oñorbe J., Farina E. P., Cantalupo S., Lusso E., 2019, [MNRAS](#), **482**, 3162
- Asplund M., Grevesse N., Sauval A. J., Scott P., 2009, [ARA&A](#), **47**, 481
- Astropy Collaboration et al., 2013, [A&A](#), **558**, A33
- Astropy Collaboration et al., 2018, [AJ](#), **156**, 123
- Augustin R., et al., 2019, [MNRAS](#), **489**, 2417
- Bacon R., et al., 2010, in McLean I. S., Ramsay S. K., Takami H., eds, Society of Photo-Optical Instrumentation Engineers (SPIE) Conference Series Vol. 7735, Ground-based and Airborne Instrumentation for Astronomy III. p. 773508, [doi:10.1117/12.856027](#)
- Bacon R., et al., 2015, [A&A](#), **575**, A75
- Bacon R., et al., 2017, [A&A](#), **608**, A1
- Bacon R., et al., 2021, arXiv e-prints, [p. arXiv:2102.05516](#)
- Baldwin J. A., Phillips M. M., Terlevich R., 1981, [PASP](#), **93**, 5 (BPT)
- Becker G. D., Bolton J. S., 2013, [MNRAS](#), **436**, 1023
- Becker G. D., Bolton J. S., Haehnelt M. G., Sargent W. L. W., 2011, [MNRAS](#), **410**, 1096
- Berg D. A., Erb D. K., Henry R. B. C., Skillman E. D., McQuinn K. B. W., 2019a, [ApJ](#), **874**, 93
- Berg D. A., Chisholm J., Erb D. K., Pogge R., Henry A., Olivier G. M., 2019b, [ApJ](#), **878**, L3
- Bian F., Kewley L. J., Dopita M. A., 2018, [ApJ](#), **859**, 175
- Bolton J. S., Becker G. D., Raskutti S., Wyithe J. S. B., Haehnelt M. G., Sargent W. L. W., 2012, [MNRAS](#), **419**, 2880
- Bolton J. S., Puchwein E., Sijacki D., Haehnelt M. G., Kim T.-S., Meiksin A., Regan J. A., Viel M., 2017, [MNRAS](#), **464**, 897
- Bonnet H., et al., 2004, [The Messenger](#), **117**, 17
- Bordoloi R., Rigby J. R., Tumlinson J., Bayliss M. B., Sharon K., Gladders M. G., Wuyts E., 2016, [MNRAS](#), **458**, 1891
- Borisova E., et al., 2016, [ApJ](#), **831**, 39
- Bothwell M. S., Maiolino R., Kennicutt R., Cresci G., Mannucci F., Marconi A., Cicone C., 2013, [MNRAS](#), **433**, 1425
- Bothwell M. S., Maiolino R., Peng Y., Cicone C., Griffith H., Wagg J., 2016a, [MNRAS](#), **455**, 1156

## References

---

- Bothwell M. S., Maiolino R., Cicone C., Peng Y., Wagg J., 2016b, [A&A](#), **595**, A48
- Bouwens R. J., et al., 2015, [ApJ](#), **803**, 34
- Bressan A., Marigo P., Girardi L., Salasnich B., Dal Cero C., Rubele S., Nanni A., 2012, [MNRAS](#), **427**, 127
- Bruzual G., Charlot S., 2003, [MNRAS](#), **344**, 1000
- Cai Z., et al., 2017, [ApJ](#), **837**, 71
- Cantalupo S., 2017, Gas Accretion and Giant Ly $\alpha$  Nebulae. Springer International Publishing AG, p. 195, doi:10.1007/978-3-319-52512-9\_9
- Cantalupo S., Porciani C., Lilly S. J., Miniati F., 2005, [ApJ](#), **628**, 61
- Cantalupo S., Porciani C., Lilly S. J., 2008, [ApJ](#), **672**, 48
- Cantalupo S., Lilly S. J., Haehnelt M. G., 2012, [MNRAS](#), **425**, 1992
- Cantalupo S., Arrigoni-Battaia F., Prochaska J. X., Hennawi J. F., Madau P., 2014, [Nature](#), **506**, 63
- Cardelli J. A., Clayton G. C., Mathis J. S., 1989, [ApJ](#), **345**, 245
- Cen R., Miralda-Escudé J., Ostriker J. P., Rauch M., 1994, [ApJ](#), **437**, L9
- Chabrier G., 2003, [PASP](#), **115**, 763
- Chiang Y.-K., Ménard B., Schiminovich D., 2019, [ApJ](#), **877**, 150
- Chisholm J., Prochaska J. X., Schaefer D., Gazagnes S., Henry A., 2020, [MNRAS](#), **498**, 2554
- Christensen L., et al., 2012a, [MNRAS](#), **427**, 1953
- Christensen L., et al., 2012b, [MNRAS](#), **427**, 1973
- Cisewski J., Croft R. A. C., Freeman P. E., Genovese C. R., Khandai N., Ozbek M., Wasserman L., 2014, [MNRAS](#), **440**, 2599
- Cresci G., Mannucci F., Curti M., 2019, [A&A](#), **627**, A42
- Croft R. A. C., Miralda-Escudé J., Zheng Z., Blomqvist M., Pieri M., 2018, [MNRAS](#), **481**, 1320
- Curti M., Mannucci F., Cresci G., Maiolino R., 2020, [MNRAS](#), **491**, 944
- Davé R., Hernquist L., Katz N., Weinberg D. H., 1999, [ApJ](#), **511**, 521
- Díaz A. I., Castellanos M., Terlevich E., Luisa García-Vargas M., 2000, [MNRAS](#), **318**, 462
- Dijkstra M., 2014, [Publ. Astron. Soc. Australia](#), **31**, e040
- Djorgovski S., Spinrad H., McCarthy P., Strauss M. A., 1985, [ApJ](#), **299**, L1
- Dopita M. A., Sutherland R. S., Nicholls D. C., Kewley L. J., Vogt F. P. A., 2013, [ApJS](#), **208**, 10
- Doré O., et al., 2018, preprint, ([arXiv:1805.05489](#))
- Draine B. T., 2011, Physics of the Interstellar and Intergalactic Medium. Princeton University Press
- Eckert D., et al., 2015, [Nature](#), **528**, 105
- Eisenhauer F., et al., 2003, in Iye M., Moorwood A. F. M., eds, Society of Photo-Optical Instrumentation Engineers (SPIE) Conference Series Vol. 4841, Instrument Design and Performance for Optical/Infrared Ground-based Telescopes. pp 1548–1561 ([arXiv:astro-ph/0306191](#)), doi:10.1117/12.459468
- Elias L. M., Genel S., Sternberg A., Devriendt J., Slyz A., Visbal E., Bouché N., 2020, [MNRAS](#), **494**, 5439

- Erb D. K., Steidel C. C., Shapley A. E., Pettini M., Reddy N. A., Adelberger K. L., 2006, [ApJ](#), **646**, 107
- Erb D. K., Quider A. M., Henry A. L., Martin C. L., 2012, [ApJ](#), **759**, 26
- Fardal M. A., Katz N., Gardner J. P., Hernquist L., Weinberg D. H., Davé R., 2001, [ApJ](#), **562**, 605
- Faucher-Giguère C.-A., Lidz A., Hernquist L., Zaldarriaga M., 2008, [ApJ](#), **688**, 85
- Faucher-Giguère C.-A., Kereš D., Dijkstra M., Hernquist L., Zaldarriaga M., 2010, [ApJ](#), **725**, 633
- Feltre A., Charlot S., Gutkin J., 2016, [MNRAS](#), **456**, 3354
- Feltre A., et al., 2018, [A&A](#), **617**, A62
- Ferland G. J., et al., 2013, Rev. Mex. Astron. Astrofis., **49**, 137
- Finley H., et al., 2017, [A&A](#), **608**, A7
- Francis P. J., et al., 1996, [ApJ](#), **457**, 490
- Franx M., Illingworth G. D., Kelson D. D., van Dokkum P. G., Tran K.-V., 1997, [ApJ](#), **486**, L75
- Freudling W., Romaniello M., Bramich D. M., Ballester P., Forchi V., García-Dabló C. E., Moehler S., Neeser M. J., 2013, [A&A](#), **559**, A96
- Fumagalli M., Cantalupo S., Dekel A., Morris S. L., O'Meara J. M., Prochaska J. X., Theuns T., 2016, [MNRAS](#), **462**, 1978
- Furlanetto S. R., Schaye J., Springel V., Hernquist L., 2003, [ApJ](#), **599**, L1
- Furlanetto S. R., Schaye J., Springel V., Hernquist L., 2005, [ApJ](#), **622**, 7
- Fynbo J. U., Møller P., Warren S. J., 1999, [MNRAS](#), **305**, 849
- Gallego S. G., et al., 2018, [MNRAS](#), **475**, 3854
- Garzilli A., Boyarsky A., Ruchayskiy O., 2017, [Physics Letters B](#), **773**, 258
- Gazagnes S., Chisholm J., Schaefer D., Verhamme A., Izotov Y., 2020, [A&A](#), **639**, A85
- Geach J. E., et al., 2016, [ApJ](#), **832**, 37
- Giavalisco M., et al., 2011, [ApJ](#), **743**, 95
- Gladders M. D., Yee H. K. C., Ellingson E., 2002, [AJ](#), **123**, 1
- Götberg Y., de Mink S. E., Groh J. H., Leitherer C., Norman C., 2019, [A&A](#), **629**, A134
- Gould A., Weinberg D. H., 1996, [ApJ](#), **468**, 462
- Guseva N. G., et al., 2020, [MNRAS](#), **497**, 4293
- Gutkin J., Charlot S., Bruzual G., 2016, [MNRAS](#), **462**, 1757
- Haardt F., Madau P., 2012, [ApJ](#), **746**, 125 (HM12)
- Hayashino T., et al., 2004, [AJ](#), **128**, 2073
- Heckman T. M., Lehnert M. D., van Breugel W., Miley G. K., 1991, [ApJ](#), **370**, 78
- Heneka C., Cooray A., Feng C., 2017, [ApJ](#), **848**, 52
- Hennawi J. F., Prochaska J. X., Cantalupo S., Arrigoni-Battaia F., 2015, [Science](#), **348**, 779
- Henry A., Berg D. A., Scarlata C., Verhamme A., Erb D., 2018, [ApJ](#), **855**, 96
- Hernquist L., Katz N., Weinberg D. H., Miralda-Escudé J., 1996, [ApJ](#), **457**, L51

## References

---

- Hicks E. K. S., Malkan M. A., Teplitz H. I., McCarthy P. J., Yan L., 2002, [ApJ, 581, 205](#)
- Hirschmann M., Charlot S., Feltre A., Naab T., Somerville R. S., Choi E., 2019, [MNRAS, 487, 333](#)
- Hogan C. J., Weymann R. J., 1987, [MNRAS, 225, 1P](#)
- Hu E. M., Songaila A., Cowie L. L., Stockton A., 1991, [ApJ, 368, 28](#)
- Humphrey A., et al., 2008, [MNRAS, 390, 1505](#)
- Hunter J. D., 2007, [Computing in Science & Engineering, 9, 90](#)
- Hutchison T. A., et al., 2019, [ApJ, 879, 70](#)
- Ikeuchi S., Ostriker J. P., 1986, [ApJ, 301, 522](#)
- Ivezić Ž., et al., 2019, [ApJ, 873, 111](#)
- Izotov Y. I., Schaerer D., Thuan T. X., Worseck G., Guseva N. G., Orlitová I., Verhamme A., 2016a, [MNRAS, 461, 3683](#)
- Izotov Y. I., Orlitová I., Schaerer D., Thuan T. X., Verhamme A., Guseva N. G., Worseck G., 2016b, [Nature, 529, 178](#)
- Izotov Y. I., Schaerer D., Worseck G., Guseva N. G., Thuan T. X., Verhamme A., Orlitová I., Fricke K. J., 2018a, [MNRAS, 474, 4514](#)
- Izotov Y. I., Worseck G., Schaerer D., Guseva N. G., Thuan T. X., Fricke Verhamme A., Orlitová I., 2018b, [MNRAS, 478, 4851](#)
- Jaskot A. E., Oey M. S., 2013, [ApJ, 766, 91](#)
- Jeong M.-S., et al., 2020, [ApJ, 902, L16](#)
- Jones E., Oliphant T., Peterson P., et al., 2001, SciPy: Open source scientific tools for Python, <http://www.scipy.org/>
- Juneau S., et al., 2014, [ApJ, 788, 88](#)
- Kakuma R., et al., 2019, preprint, ([arXiv:1906.00173](#))
- Karman W., et al., 2016, [A&A, 585, A27](#)
- Katz N., Weinberg D. H., Hernquist L., 1996, [ApJS, 105, 19](#)
- Kausch W., et al., 2015, [A&A, 576, A78](#)
- Keel W. C., Cohen S. H., Windhorst R. A., Waddington I., 1999, [AJ, 118, 2547](#)
- Kewley L. J., Dopita M. A., Sutherland R. S., Heisler C. A., Trevena J., 2001, [ApJ, 556, 121](#)
- Kewley L. J., Groves B., Kauffmann G., Heckman T., 2006, [MNRAS, 372, 961](#)
- Kewley L. J., Nicholls D. C., Sutherland R., Rigby J. R., Acharya A., Dopita M. A., Bayliss M. B., 2019, [ApJ, 880, 16](#)
- Khaire V., et al., 2019, [MNRAS, 486, 769](#)
- Khullar G., et al., 2021, [ApJ, 906, 107](#)
- Kinney A. L., Bohlin R. C., Calzetti D., Panagia N., Wyse R. F. G., 1993, [ApJS, 86, 5](#)
- Kollmeier J. A., Zheng Z., Davé R., Gould A., Katz N., Miralda-Escudé J., Weinberg D. H., 2010, [ApJ, 708, 1048](#)
- Kornei K. A., Shapley A. E., Martin C. L., Coil A. L., Lotz J. M., Weiner B. J., 2013, [ApJ, 774, 50](#)

- Kriek M., van Dokkum P. G., Labbé I., Franx M., Illingworth G. D., Marchesini D., Quadri R. F., 2009, [ApJ](#), **700**, 221
- Kulkarni G., Keating L. C., Haehnelt M. G., Bosman S. E. I., Puchwein E., Chardin J., Aubert D., 2019a, [MNRAS](#), **485**, L24
- Kulkarni G., Worseck G., Hennawi J. F., 2019b, [MNRAS](#), **488**, 1035
- Kull A., Böhringer H., 1999, [A&A](#), **341**, 23
- Laporte N., Nakajima K., Ellis R. S., Zitrin A., Stark D. P., Mainali R., Roberts-Borsani G. W., 2017, [ApJ](#), **851**, 40
- Leclercq F., et al., 2017, [A&A](#), **608**, A8
- Levesque E. M., Richardson M. L. A., 2014, [ApJ](#), **780**, 100
- Lukić Z., Stark C. W., Nugent P., White M., Meiksin A. A., Almgren A., 2015, [MNRAS](#), **446**, 3697
- Lusso E., et al., 2019, [MNRAS](#), **485**, L62
- Madau P., Dickinson M., 2014, [ARA&A](#), **52**, 415
- Mainali R., Kollmeier J. A., Stark D. P., Simcoe R. A., Walth G., Newman A. B., Miller D. R., 2017, [ApJ](#), **836**, L14
- Maiolino R., Mannucci F., 2019, [A&ARv](#), **27**, 3
- Maiolino R., et al., 2008, [A&A](#), **488**, 463
- Malkan M. A., Jensen L. D., Rodriguez D. R., Spinoglio L., Rush B., 2017, [ApJ](#), **846**, 102
- Mannucci F., Cresci G., Maiolino R., Marconi A., Gnerucci A., 2010, [MNRAS](#), **408**, 2115
- Martin D. C., Chang D., Matuszewski M., Morrissey P., Rahman S., Moore A., Steidel C. C., 2014, [ApJ](#), **786**, 106
- Mason C. A., Treu T., Dijkstra M., Mesinger A., Trenti M., Pentericci L., de Barros S., Vanzella E., 2018, [ApJ](#), **856**, 2
- Matsuda Y., et al., 2012, [MNRAS](#), **425**, 878
- Matthee J., et al., 2021, [MNRAS](#), **505**, 1382
- McCarthy P. J., Spinrad H., van Breugel W., Liebert J., Dickinson M., Djorgovski S., Eisenhardt P., 1990, [ApJ](#), **365**, 487
- McGreer I. D., Mesinger A., D'Odorico V., 2015, [MNRAS](#), **447**, 499
- Meiksin A. A., 2009, [Reviews of Modern Physics](#), **81**, 1405
- Meiksin A., White M., 2003, [MNRAS](#), **342**, 1205
- Momose R., et al., 2014, [MNRAS](#), **442**, 110
- Morrissey P., et al., 2018, [ApJ](#), **864**, 93
- Nagao T., Maiolino R., Marconi A., 2006, [A&A](#), **459**, 85
- Oñorbe J., Hennawi J. F., Lukić Z., 2017, [ApJ](#), **837**, 106
- Oñorbe J., Davies F. B., Lukić Z., Hennawi J. F., Sorini D., 2019, [MNRAS](#), **486**, 4075
- Oke J. B., Gunn J. E., 1983, [ApJ](#), **266**, 713
- Oteo I., et al., 2018, [ApJ](#), **856**, 72

## References

---

- Ouchi M., et al., 2018, [PASJ](#), **70**, S13
- Partridge R. B., Peebles P. J. E., 1967, [ApJ](#), **147**, 868
- Patrício V., et al., 2016, [MNRAS](#), **456**, 4191
- Pentericci L., et al., 2018, [A&A](#), **619**, A147
- Pérez-Montero E., Hägele G. F., Contini T., Díaz Á. I., 2007, [MNRAS](#), **381**, 125
- Pettini M., et al., 2010, [MNRAS](#), **402**, 2335
- Planck Collaboration et al., 2014, [A&A](#), **571**, A16
- Prescott M. K. M., Dey A., Jannuzzi B. T., 2013, [ApJ](#), **762**, 38
- Puchwein E., Haardt F., Haehnelt M. G., Madau P., 2019, [MNRAS](#), **485**, 47 (P19)
- Rahmati A., Pawlik A. H., Raičević M., Schaye J., 2013, [MNRAS](#), **430**, 2427
- Rauch M., et al., 1997, [ApJ](#), **489**, 7
- Rauch M., et al., 2008, [ApJ](#), **681**, 856
- Rauch M., Becker G. D., Haehnelt M. G., Gauthier J.-R., Ravindranath S., Sargent W. L. W., 2011, [MNRAS](#), **418**, 1115
- Rauch M., Becker G. D., Haehnelt M. G., Gauthier J.-R., Sargent W. L. W., 2013, [MNRAS](#), **429**, 429
- Richard J., et al., 2019, preprint, ([arXiv:1906.01657](#))
- Rigby J. R., Bayliss M. B., Gladders M. D., Sharon K., Wuylts E., Dahle H., 2014, [ApJ](#), **790**, 44
- Roche N., Humphrey A., Binette L., 2014, [MNRAS](#), **443**, 3795
- Rosdahl J., Blaizot J., 2012, [MNRAS](#), **423**, 344
- Rubin K. H. R., Weiner B. J., Koo D. C., Martin C. L., Prochaska J. X., Coil A. L., Newman J. A., 2010, [ApJ](#), **719**, 1503
- Rubin K. H. R., Prochaska J. X., Ménard B., Murray N., Kasen D., Koo D. C., Phillips A. C., 2011, [ApJ](#), **728**, 55
- Sachkov M., Shustov B., Gómez de Castro A. I., 2018, in den Herder J.-W. A., Nikzad S., Nakazawa K., eds, Society of Photo-Optical Instrumentation Engineers (SPIE) Conference Series Vol. 10699, Space Telescopes and Instrumentation 2018: Ultraviolet to Gamma Ray. p. 106993G, doi:10.1117/12.2312923
- Salmon B., et al., 2015, [ApJ](#), **799**, 183
- Sánchez S. F., Humphrey A., 2009, [A&A](#), **495**, 471
- Sanders R. L., et al., 2016, [ApJ](#), **816**, 23
- Sanders R. L., et al., 2021, [ApJ](#), **914**, 19
- Schaye J., Theuns T., Rauch M., Efstatihou G., Sargent W. L. W., 2000, [MNRAS](#), **318**, 817
- Schenker M. A., Ellis R. S., Konidaris N. P., Stark D. P., 2014, [ApJ](#), **795**, 20
- Scholz T. T., Walters H. R. J., 1991, [ApJ](#), **380**, 302
- Scholz T. T., Walters H. R. J., Burke P. J., Scott M. P., 1990, [MNRAS](#), **242**, 692
- Senchyna P., et al., 2017, [MNRAS](#), **472**, 2608
- Senchyna P., Stark D. P., Chevallard J., Charlot S., Jones T., Vidal-García A., 2019, [MNRAS](#), **488**, 3492

- Shapley A. E., Steidel C. C., Pettini M., Adelberger K. L., 2003, [ApJ](#), **588**, 65
- Shapley A. E., et al., 2017, [ApJ](#), **846**, L30
- Sharples R., et al., 2013, *The Messenger*, **151**, 21
- Shibuya T., et al., 2014, [ApJ](#), **788**, 74
- Silva M. B., Santos M. G., Gong Y., Cooray A., Bock J., 2013, [ApJ](#), **763**, 132
- Silva M. B., Kooistra R., Zaroubi S., 2016, [MNRAS](#), **462**, 1961
- Smette A., et al., 2015, [A&A](#), **576**, A77
- Smit R., et al., 2014, [ApJ](#), **784**, 58
- Smit R., et al., 2015, [ApJ](#), **801**, 122
- Smit R., Swinbank A. M., Massey R., Richard J., Smail I., Kneib J. P., 2017, [MNRAS](#), **467**, 3306
- Sobral D., Smail I., Best P. N., Geach J. E., Matsuda Y., Stott J. P., Cirasuolo M., Kurk J., 2013, [MNRAS](#), **428**, 1128
- Springel V., 2005, [MNRAS](#), **364**, 1105
- Springel V., Yoshida N., White S. D. M., 2001, [New Astron.](#), **6**, 79
- Stark D. P., 2016, [ARA&A](#), **54**, 761
- Stark D. P., et al., 2015, [MNRAS](#), **454**, 1393
- Stark D. P., et al., 2017, [MNRAS](#), **464**, 469
- Steidel C. C., Adelberger K. L., Shapley A. E., Pettini M., Dickinson M., Giavalisco M., 2000, [ApJ](#), **532**, 170
- Steidel C. C., Bogosavljević M., Shapley A. E., Kollmeier J. A., Reddy N. A., Erb D. K., Pettini M., 2011, [ApJ](#), **736**, 160
- Steidel C. C., Strom A. L., Pettini M., Rudie G. C., Reddy N. A., Trainor R. F., 2016, [ApJ](#), **826**, 159
- Stott J. P., et al., 2016, [MNRAS](#), **457**, 1888
- Swinbank A. M., Bower R. G., Smith G. P., Wilman R. J., Smail I., Ellis R. S., Morris S. L., Kneib J. P., 2007, [MNRAS](#), **376**, 479
- Swinbank A. M., et al., 2009, [MNRAS](#), **400**, 1121
- Tanimura H., et al., 2019, [MNRAS](#), **483**, 223
- Thatte N. A., et al., 2014, in Ramsay S. K., McLean I. S., Takami H., eds, Society of Photo-Optical Instrumentation Engineers (SPIE) Conference Series Vol. 9147, Ground-based and Airborne Instrumentation for Astronomy V. p. 914725, doi:10.1117/12.2055436
- Tinker J., Kravtsov A. V., Klypin A., Abazajian K., Warren M., Yepes G., Gottlöber S., Holz D. E., 2008, [ApJ](#), **688**, 709
- Toshikawa J., et al., 2016, [ApJ](#), **826**, 114
- Toshikawa J., et al., 2018, [PASJ](#), **70**, S12
- Tremonti C. A., et al., 2004, [ApJ](#), **613**, 898
- Troncoso P., et al., 2014, [A&A](#), **563**, A58
- Umeshata H., et al., 2019, [Science](#), **366**, 97

## References

---

- Valls-Gabaud D., MESSIER Collaboration 2017, in Gil de Paz A., Knapen J. H., Lee J. C., eds, Vol. 321, Formation and Evolution of Galaxy Outskirts. pp 199–201, doi:10.1017/S1743921316011388
- Vanzella E., et al., 2016, *ApJ*, 825, 41
- Vanzella E., et al., 2017, *MNRAS*, 465, 3803
- Vanzella E., et al., 2020, *MNRAS*, 491, 1093
- Veilleux S., Osterbrock D. E., 1987, *ApJS*, 63, 295
- Venemans B. P., et al., 2007, *A&A*, 461, 823
- Verhamme A., Schaerer D., Maselli A., 2006, *A&A*, 460, 397
- Verhamme A., Orlitová I., Schaerer D., Izotov Y., Worseck G., Thuan T. X., Guseva N., 2017, *A&A*, 597, A13
- Vernet J., et al., 2011, *A&A*, 536, A105
- Viel M., Haehnelt M. G., Springel V., 2004, *MNRAS*, 354, 684
- Villar-Martín M., Sánchez S. F., Humphrey A., Dijkstra M., di Serego Alighieri S., De Breuck C., González Delgado R., 2007, *MNRAS*, 378, 416
- Van der Walt S., Colbert S. C., Varoquaux G., 2011, *Computing in Science and Engineering*, 13, 22
- Walther M., Oñorbe J., Hennawi J. F., Lukić Z., 2019, *ApJ*, 872, 13
- Weinberg D., et al. 1999, in Banday A. J., Sheth R. K., da Costa L. N., eds, Evolution of Large Scale Structure : From Recombination to Garching. p. 346 ([arXiv:astro-ph/9810142](https://arxiv.org/abs/astro-ph/9810142))
- Weiner B. J., et al., 2009, *ApJ*, 692, 187
- Wisotzki L., et al., 2016, *A&A*, 587, A98
- Wisotzki L., et al., 2018, *Nature*, 562, 229
- Wold I. G. B., Finkelstein S. L., Barger A. J., Cowie L. L., Rosenwasser B., 2017, *ApJ*, 848, 108
- Wuyts S., et al., 2016, *ApJ*, 831, 149
- Yang H., Malhotra S., Gronke M., Rhoads J. E., Dijkstra M., Jaskot A., Zheng Z., Wang J., 2016, *ApJ*, 820, 130
- Yang H., et al., 2017, *ApJ*, 844, 171
- Zeimann G. R., et al., 2015, *ApJ*, 798, 29
- de Barros S., et al., 2016, *A&A*, 585, A51
- de Graaff A., Cai Y.-C., Heymans C., Peacock J. A., 2019, *A&A*, 624, A48

# APPENDIX A

## MODELLING LYMAN- $\alpha$ EMISSION

---

### A.1 Model parameters and fitting functions

#### A.1.1 Emission processes

This section contains the fitting functions for the relevant quantities in the formulae for recombination and collisional excitation emissivity (Eqs. (1.1) and (1.2) in Sects. 1.2.1 and 1.2.2), which are repeated here for clarity.

Recombination emissivity (Eq. (1.1)) is written as

$$\epsilon_{\text{rec}}(T) = f_{\text{rec, A/B}}(T) n_e n_{\text{HII}} \alpha_{\text{A/B}}(T) E_{\text{Ly}\alpha}. \quad (\text{A.1})$$

Collisional excitation emissivity (Eq. (1.2)) is given by

$$\epsilon_{\text{exc}}(T) = \gamma_{1s2p}(T) n_e n_{\text{HI}} E_{\text{Ly}\alpha}. \quad (\text{A.2})$$

#### Recombination fitting functions

The underlying equation governing Ly $\alpha$  emission due to recombination in the IGM is given in Eq. (A.1). The recombination fraction  $f_{\text{rec, A/B}}$  gives the number of recombinations that ultimately result in the emission of a Ly $\alpha$  photon. This fraction can be modelled using the relations given in [Cantalupo et al. \(2008\)](#) and [Dijkstra \(2014\)](#) and can be summarised as follows:

$$f_{\text{rec, A/B}} = \begin{cases} 0.41 - 0.165 \log_{10} \left( \frac{T}{10^4 \text{K}} \right) \\ \quad - 0.015 \left( \frac{T}{10^4 \text{K}} \right)^{-0.44}, & \text{case-A} \\ 0.686 - 0.106 \log_{10} \left( \frac{T}{10^4 \text{K}} \right) \\ \quad - 0.009 \left( \frac{T}{10^4 \text{K}} \right)^{-0.44}, & \text{case-B.} \end{cases}$$

**Table A.1** Coefficients  $c_i$  in Eq. (A.4) and their corresponding temperature regimes.

	<b>Regime 1</b>	<b>Regime 2</b>	<b>Regime 3</b>
$c_0$	$-1.630155 \cdot 10^2$	$5.279996 \cdot 10^2$	$-2.8133632 \cdot 10^3$
$c_1$	$8.795711 \cdot 10^1$	$-1.939399 \cdot 10^2$	$8.1509685 \cdot 10^2$
$c_2$	$-2.057117 \cdot 10^1$	$2.718982 \cdot 10^1$	$-9.4418414 \cdot 10^1$
$c_3$	2.359573	-1.883399	5.4280565
$c_4$	$-1.339059 \cdot 10^{-1}$	$6.462462 \cdot 10^{-2}$	$-1.5467120 \cdot 10^{-1}$
$c_5$	$3.021507 \cdot 10^{-3}$	$-8.811076 \cdot 10^{-4}$	$1.7439112 \cdot 10^{-3}$
	<b>Regimes</b>	<b>Temperature values</b>	
	Regime 1	$2 \cdot 10^3 \text{ K} \leq T < 6 \cdot 10^4 \text{ K}$	
	Regime 2	$6 \cdot 10^4 \text{ K} \leq T < 6 \cdot 10^6 \text{ K}$	
	Regime 3	$6 \cdot 10^6 \text{ K} \leq T \leq 1 \cdot 10^8 \text{ K}$	

The recombination coefficient,  $\alpha_{\text{A/B}}$ , is given in the work of [Draine \(2011\)](#) as follows:

$$\alpha_{\text{A/B}} = \begin{cases} 4.13 \cdot 10^{-13} \left( \frac{T}{10^4 \text{ K}} \right)^{-0.7131 - 0.0115 \log_{10} \left( \frac{T}{10^4 \text{ K}} \right)} \text{ cm}^3 \text{ s}^{-1}, & \text{case-A} \\ 2.54 \cdot 10^{-13} \left( \frac{T}{10^4 \text{ K}} \right)^{-0.8163 - 0.0208 \log_{10} \left( \frac{T}{10^4 \text{ K}} \right)} \text{ cm}^3 \text{ s}^{-1}, & \text{case-B.} \end{cases}$$

### Collisional excitation fitting functions

For collisional excitation, the Ly $\alpha$  luminosity density is given by Eq. (A.2). The function  $\gamma_{1s2p}$  in this formula is given by

$$\gamma_{1s2p}(T) = \Gamma(T) \exp \left( -\frac{E_{\text{Ly}\alpha}}{k_B T} \right), \quad (\text{A.3})$$

where  $k_B$  is the Boltzmann constant. The function  $\Gamma(T)$  is characterised in [Scholz et al. \(1990\)](#) and [Scholz & Walters \(1991\)](#) as follows:

$$\Gamma(T) = \exp \left( \sum_{i=0}^5 c_i (\ln T)^i \right), \quad (\text{A.4})$$

where the coefficients  $c_i$  found by [Scholz et al. \(1990\)](#) and [Scholz & Walters \(1991\)](#) are dependent on the temperature regime (shown in Table A.1). As noted in Sect. 1.2.2, the rates are not identical to those applied in the cosmological hydrodynamical simulation, but in the relevant temperature regime deviate so little that the Ly $\alpha$  emission would not be appreciably changed.

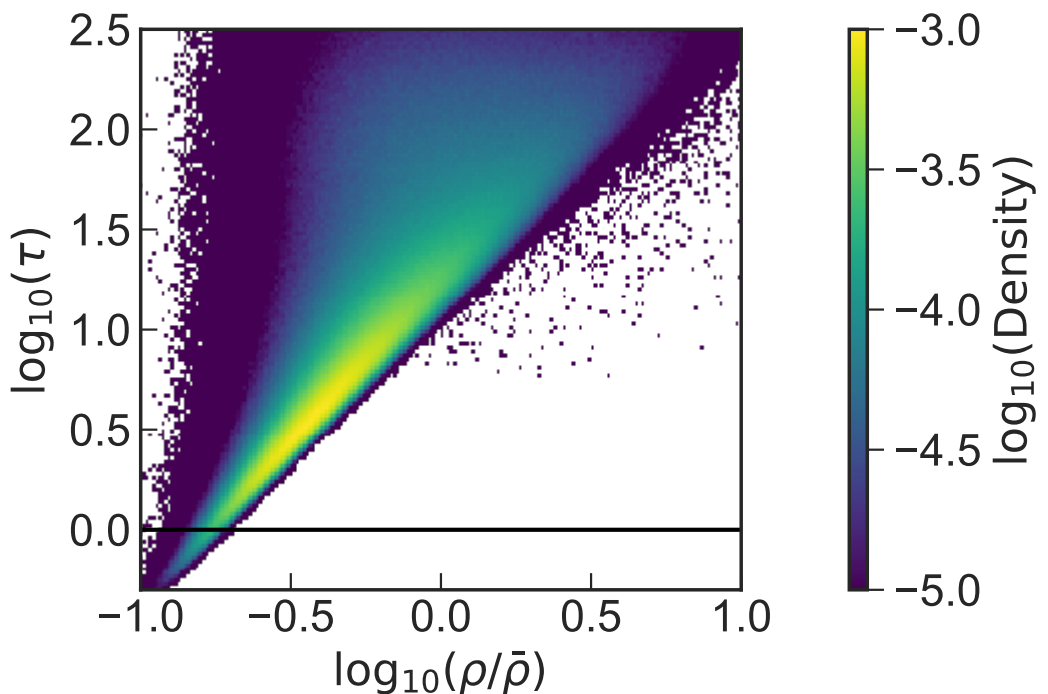


**Figure A.1** Two-dimensional density histogram for each of 2048 pixels in spectra along 5000 (randomly selected) lines of sight at  $z = 4.8$ , as a function of the Ly $\alpha$  optical depth  $\tau$  and overdensity  $\rho/\bar{\rho}$  in the sightline; the two parameters are measured at line centre, where the optical depth was divided by 2 just to account for the hydrogen between the source and the observer (see text).

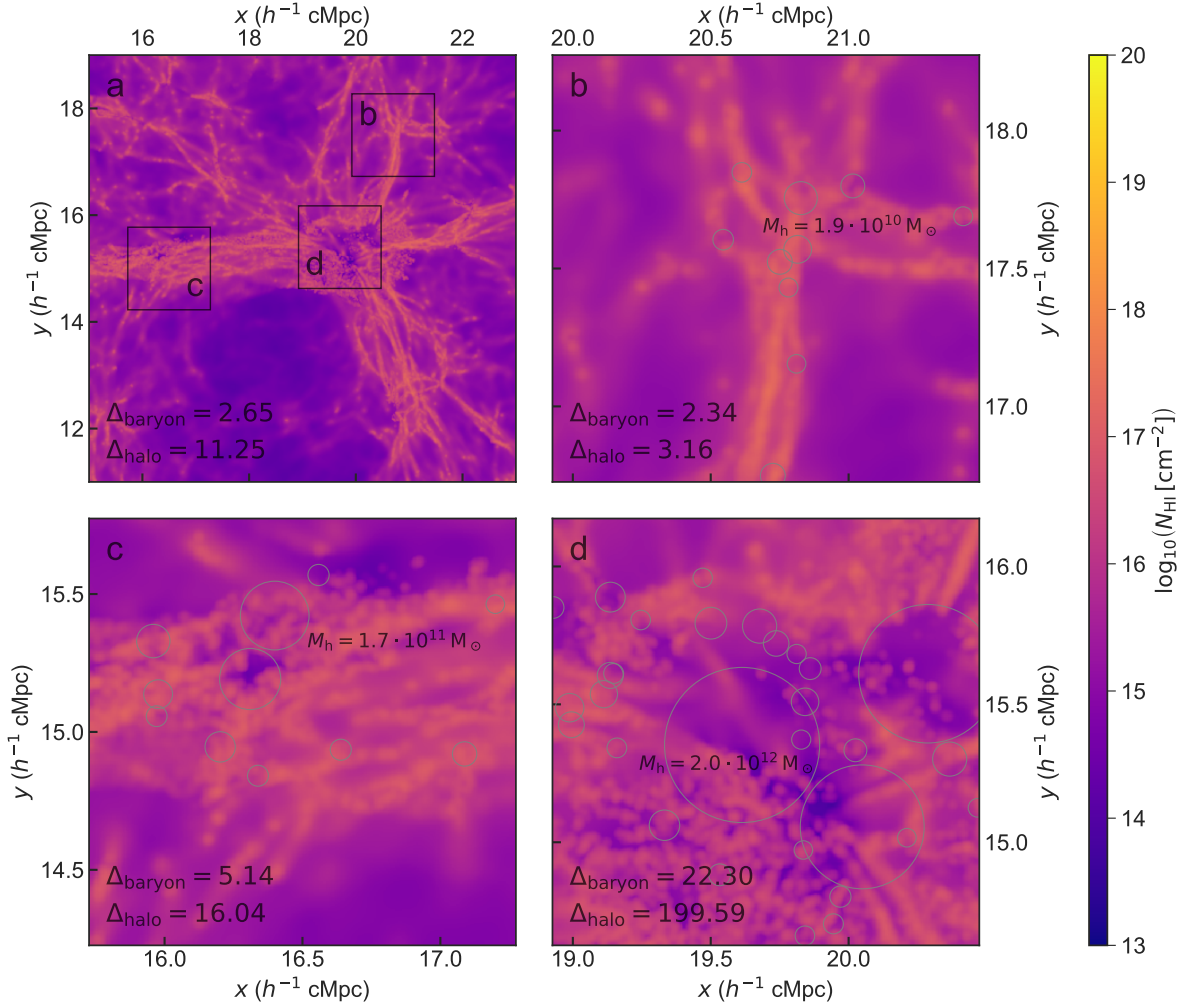


**Figure A.2** Simulated column density of neutral hydrogen,  $N_{\text{HI}}$ , in a simulation snapshot at  $z = 4.8$ . The same regions as in Fig. 1.8 are shown. Moreover, the same density thresholds used for the collisional excitation component are applied, that is only gas below half the critical self-shielding density is shown, meaning this is the column density that would correspond to a narrowband image of the low-density gas with  $\Delta\lambda_{\text{obs}} = 3.75 \text{ \AA}$  ( $\sim 1.19 h^{-1} \text{ cMpc}$ ). Panel **a** shows an overview of part of the simulation snapshot that corresponds to region 1 in Fig. 1.4. This is centred on the same comoving coordinates both spatially and spectrally, but now less extended in wavelength range. This panel shows a region of  $8 \times 8 h^{-2} \text{ cMpc}^2$  ( $5.2 \times 5.2 \text{ arcmin}^2$ ) on a pixel grid of  $1024 \times 1024$ . Panels **b-d** show column density maps of neutral hydrogen the size of the MUSE FOV consisting of  $300 \times 300$  pixels. The areas covered by these maps are indicated by the black squares in the overview panel **a**. In the bottom left corner of each panel, two different measures of the overdensity of the region are shown (see Sect. 1.3.4 for more details). In panels **b-d**, halos with halo mass of  $M_h > 10^{9.5} M_\odot$  are shown as circles, their size indicating their projected virial radius (see Sect. 1.3.4). The most massive halo in each panel is annotated.

## A.1 Model parameters and fitting functions

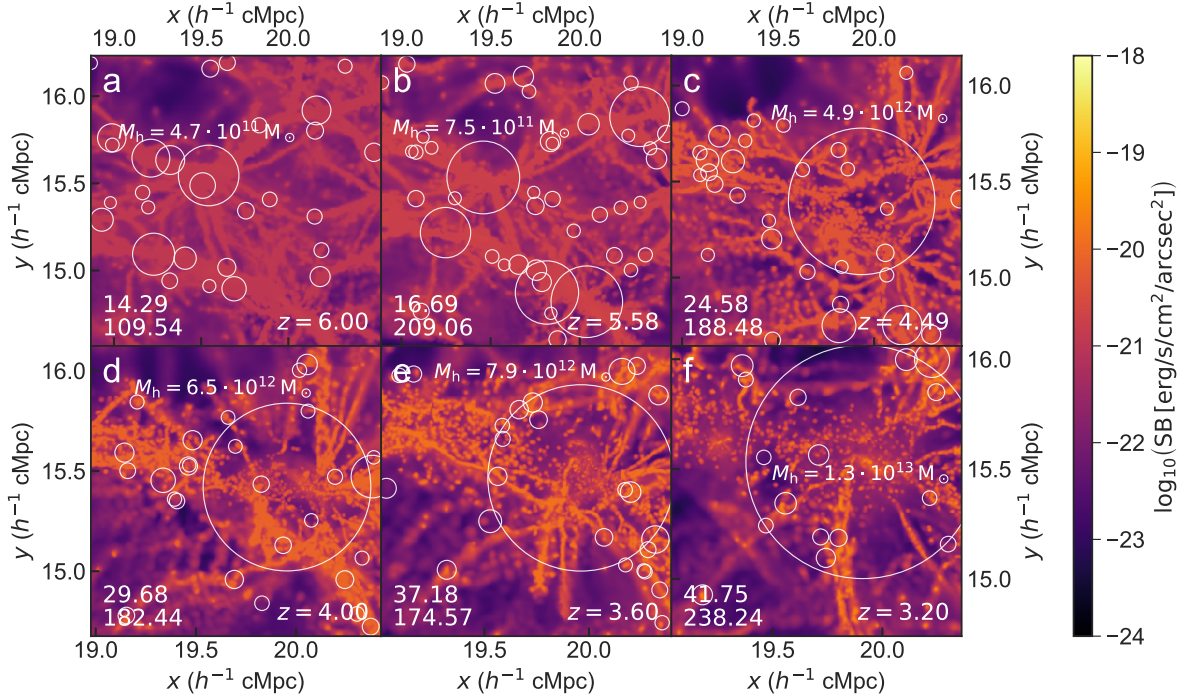


**Figure A.3** Ly $\alpha$  SB for a combination of recombination emission (of all gas in the simulation) below the mirror limit and collisional excitation of gas below half the critical self-shielding density at different redshifts. Both the mirror limit and the critical self-shielding density evolve as a function of redshift (see Fig. 1.1). The panels show snapshots at redshifts of  $z = 6.00$ ,  $z = 5.58$ ,  $z = 4.49$ ,  $z = 4.00$ ,  $z = 3.60$ ,  $z = 3.20$  for a narrowband with  $\Delta\lambda_{\text{obs}} = 3.75 \text{ \AA}$ ; at  $z = 5.76$ ; this corresponds to  $\sim 1.19 h^{-1} \text{ cMpc}$ , but this again changes with redshift. The panels all display a pixel grid of  $300 \times 300$  and the angular size of the MUSE FOV ( $1 \times 1 \text{ arcmin}^2$ ), which translates to different physical sizes at each corresponding redshift. The regions are all centred at the same comoving transverse coordinates as panel d in Fig. 1.8 and Fig. 1.10; however, the narrowband centre (the coordinate along the line of sight) has been chosen to coincide with the most massive halo in each panel to ensure the entire filament is captured in each panel. The two numbers in the bottom left corner show the same two different measures of the overdensity of the region,  $\Delta_{\text{baryon}}$  and  $\Delta_{\text{halo}}$  (see Sect. 1.3.4 for more details). Halos with halo mass of  $M_h > 10^{9.5} M_\odot$  are shown as circles, their size indicating their projected virial radius. The most massive halo in each panel is annotated. The scale varies between different panels since the angular size is kept constant across all redshifts.

## A.2 Ly $\alpha$ optical depth

This work does not contain treatment of Ly $\alpha$  line radiative transfer effects (Sect. 1.2.4). For our purposes, the treatment without radiative transfer gives us valuable insights into the lower-density IGM filaments on large, cosmological scales without having to resort to implementing computationally expensive radiative transfer methods that are difficult to accurately model, for example because the effects of dust are poorly constrained.

In Fig. A.1, a two-dimensional density histogram for each of 2048 pixels in mock Ly $\alpha$  absorption spectra along 5000 lines of sight at  $z = 4.8$  is shown as a function of both the Ly $\alpha$  optical depth  $\tau$  and overdensity  $\rho/\bar{\rho}$  in the relevant pixel. These spectra are extracted on the fly at redshift intervals  $\Delta z = 0.1$  and are constructed from the gas density and neutral fraction, temperature, and peculiar velocity of neutral hydrogen along these lines of sight (for details, see Bolton et al., 2017, where they are studied in the context of the Ly $\alpha$  forest). The peculiar velocity of the gas in a given pixel has been used to translate its position to redshift space where optical depth is determined. Therefore both density and optical depth are effectively measured at line centre. The optical depth was divided by a factor of 2 to account for the fact that on average only half of the matter is in between the source and the observer; the other half is located behind the source.<sup>1</sup> From this figure, it is clear that at mean density optical depths of order 10 are reached, indicating that radiative transfer has an effect on most regions. However, effectively this plot still shows an overestimated measure of optical depth. Since it uses a measure of optical depth at line centre, this does not mean that physically no Ly $\alpha$  emission is detected in the optically thick regime ( $\tau > 1$ ). Many Ly $\alpha$  photons may be able to escape because an initial scattering not only changes the direction of propagation of photons, but also shifts their frequency and the optical depth decreases quickly when moving away from line centre. An example of this effect is the Ly $\alpha$  radiation from galaxies, where densities are high enough to have optical depths of the order of  $10^6$ , but escape away from line centre is still possible. The optical depth thus mostly informs the expected degree of scattering, that is spatial and spectral broadening of the line profile.

Additionally, the neutral hydrogen (H I) column density at  $z = 4.8$  is shown in Fig. A.2 for precisely the same simulation region (and density limits used for collisional excitation) as in Fig. 1.8, with the same narrowband width of  $\Delta\lambda_{\text{obs}} = 3.75 \text{ \AA}$  (equivalent to  $\sim 1.19 h^{-1} \text{ cMpc}$ ), and pixel grids of pixel grid of  $1024 \times 1024$  (panel a) and  $300 \times 300$  (panels b-d). The overview map (panel a) shows that all areas have column densities of at least  $N_{\text{HI}} \sim 10^{15} \text{ cm}^{-2}$ . The most extreme features of the low-density gas show column densities of  $10^{17}\text{-}10^{18} \text{ cm}^{-2}$ , which is the range of Lyman-limit systems. Except for the self-shielding prescription, simulations that are very similar to that used in this work are found to match observational H I column

---

<sup>1</sup>We note that the division by 2 is necessary as the Ly $\alpha$  optical depths were originally extracted to study Ly $\alpha$  forest absorption in the spectra of background sources in which case all the gas that affects a pixel in redshift space is in front of the source in real space.

density distributions well at lower redshifts, where data are more abundant, at least up to  $N_{\text{HI}} \sim 3 \cdot 10^{16} \text{ cm}^{-2}$ , where self-shielding is expected to have a negligible effect (Bolton et al., 2017). At higher column densities, the self-shielding prescription that we use (Rahmati et al., 2013) was calibrated to yield realistic column density distributions. At the highest column densities, our simulation will certainly be affected by our simplistic galaxy formation model. These high densities are, however, not the focus of this study.

As with Fig. A.1, it has to be taken into account that this is the column density projected for the entire narrowband. Emitting structures seen within this slice always lie between the boundaries of this region. Therefore part of the column density that is projected may be behind the emitting region, as seen from the observer’s perspective. This means that, on average, the actual values of column densities photons travels through is about half of what is displayed.

As discussed in Sect. 1.2.4, it is expected that the precise way in which these scattering processes affect the perceived SB images are the result of a competition between two underlying effects. One possibility is that the photons emerging from the filamentary structure might be spread out, causing the signal to become fainter. The second possibility is that the filament signal might be enhanced by Ly $\alpha$  radiation coming from nearby dense structures (where additional radiation is likely to be produced in galaxies) that is scattered in the filament, thereby causing the filaments to appear brighter. As mentioned, similar simulations including radiative transfer show a mixture of these two effects, where the SB of filaments generally is not affected much or even boosted (private communication, Weinberger, 2019).

### A.3 Redshift evolution

The region extensively discussed in Sect. 1.3.4, shown in panel d of Fig. 1.8 and all panels in 1.10, is shown at different redshifts in Fig. A.3, again showing the combination of recombination emission of all gas in the simulation below the mirror limit and collisional excitation of gas below half the critical self-shielding density. The panels shown are centred at the same transverse comoving coordinates as panel d in Fig. 1.8 and all panels in 1.10, but the narrowband centre (the coordinate along the line of sight) is now chosen to coincide with the most massive halo in each panel to ensure the same structure is captured in each panel. Each panel covers the angular size of the MUSE FOV, the physical extent of which varies at different redshifts.

Following the redshift evolution from high to low (going from panel a to panel f), we note that the comoving size of the observed region shrinks roughly from  $\sim 1.5 \times 1.5 h^{-2} \text{ cMpc}^2$  to just over  $\sim 1 \times 1 h^{-2} \text{ cMpc}^2$  since the angular size of the FOV is kept fixed at  $1 \times 1 \text{ arcmin}^2$ . The appearance of new massive ( $M_h > 10^{9.5} M_\odot$ ) halos and their evolution in relative movement and mass accretion, indicated by the increase in their virial radii, can also be traced between the different panels. Panel e, at  $z = 3.60$ , has the same redshift as shown in the bottom two panels of Fig. 1.10.

## Modelling Lyman- $\alpha$ emission

---

With these conservative limits that exclude emission from the dense (and complicated) central regions of halos, Ly $\alpha$  emission appears brighter at low redshift, where the mirror limit is less affected by SB dimming and self-shielding effects only start to play a role at higher overdensities, as discussed in Sect. 1.3.4. Panels a and b appear particularly homogeneous as large portions are impacted by the mirror limit (24.6% and 22.1% of pixels exceeding the mirror limit). We note that at low redshift, on the other hand, there is less low-density gas that is luminous in Ly $\alpha$ , especially within the large, central halo. The gas there is likely denser and hotter and thus less effective at emitting Ly $\alpha$  radiation, at least within the low-density regime that we are considering (cf. Figs. 1.3 and 1.6 and their discussion in the text).

## APPENDIX B

# ASSESSING THE SOURCES OF REIONISATION: A SPECTROSCOPIC CASE STUDY OF A $30\times$ LENSED GALAXY AT $z \sim 5$ WITH LY $\alpha$ , CIV, Mg II, AND [Ne III]

---

### B.1 Mg ii and C iii significance

In this appendix, we elaborate on the significance of the (non-)detections of the Mg II emission line and the C III]  $\lambda 1907$ , [C III]  $\lambda 1909$  doublet. In Fig. B.1, X-shooter spectra of Mg II are shown for each of the three observation blocks (OBs) individually (first three columns) and the combined result for a smaller and extended aperture (final two columns). The measured velocity offset and flux for each different configuration are summarised in Table B.1.

Furthermore, Fig. B.2 shows the portion of the spectrum where the C III doublet would be expected, both without and with telluric absorption correction (TAC; see Sect. 2.2.1). It is unclear whether a signal is present in the spectra, which lack a clear dark-light-dark pattern (cf. Fig. 2.1), in part because of skyline contamination and partly owing to the strong telluric absorption. We have chosen not to attempt to measure an upper limit for the [C III]  $\lambda 1909$  line directly, as it falls precisely on a region that is heavily impacted by skylines and telluric absorption. Instead, we assume a line ratio (see Sect. 2.3.1).

**Table B.1** Measured velocity offset and line flux in different subsets of the X-shooter data, corresponding to the rows in Fig. B.1. Given quantities are defined as in Table 2.1.

Configuration	$\Delta v$ (km/s)	Flux ( $10^{-18}$ erg s $^{-1}$ cm $^{-2}$ )
OB1	$45 \pm 56$	$5.33 \pm 1.45$
OB2	$54 \pm 53$	$6.17 \pm 1.41$
OB3	$79 \pm 56$	$5.97 \pm 3.01$
Default aperture	$56 \pm 54$	$4.65 \pm 0.90$
Extended aperture	$52 \pm 54$	$5.00 \pm 1.49$

## Assessing the sources of reionisation: a spectroscopic case study of a $30\times$ lensed galaxy at $z \sim 5$ with Ly $\alpha$ , C IV, Mg II, and [Ne III]

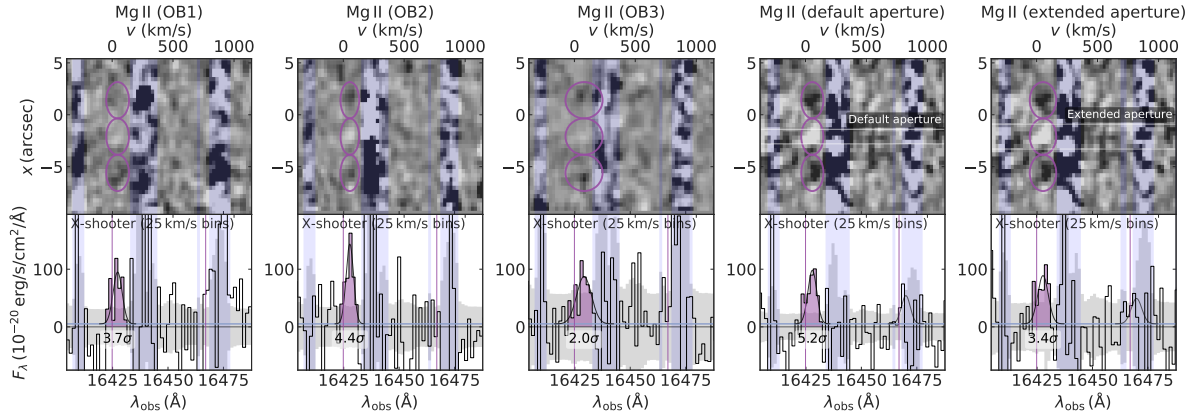


**Figure B.1** X-shooter spectra of Mg II for each of the three OBs individually (first three columns) and the combined spectra for a smaller and extended aperture (final two columns). One-dimensional spectra for the individual OBs have been extracted from the same smaller aperture as in the fourth column.

## B.2 SDSS selection

For the comparison sample drawn from the SDSS DR7 (discussed in Sect. 2.4.2), we outline the selection criteria here in detail. Following previous studies (e.g. Kewley et al., 2006; Juneau et al., 2014; Feltre et al., 2016), we select galaxies satisfying the following criteria:

- (i) TARGETTYPE = GALAXY and Z\_WARNING = 0.
- (ii) For all emission lines in the ratios [O III]/H $\beta$ , [N II]/H $\alpha$ , [S II]/H $\alpha$ , and [O I]/H $\alpha$  used in BPT diagrams, we require a SNR of  $\text{SNR} > 3/\sqrt{2} \approx 2.12$  on the ratios themselves (leading to a more complete sample, see Juneau et al. (2014) – additionally, formal uncertainty corrections as discussed in their Appendix A have been applied). Furthermore, we only select galaxies with  $\text{SNR} > 30$  on the [O II] doublet – see the discussion in Sect. 2.4.2.
- (iii) In order to align with previous studies, redshifts between  $0.04 < z < 0.2$ . These lower and upper limits are imposed to avoid strong fiber-aperture effects, and to cover detections of intrinsically weak lines while maintaining a good completeness for Seyfert-type galaxies, respectively (e.g. Juneau et al., 2014).
- (iv) A valid stellar mass measurement (17 entries have  $M_* = -1$ ).

This leads to a final sample of 8960 galaxies. We classify the galaxies into star-forming, composite, Seyfert, and LINER classes (although we will focus only on star-forming and Seyfert types), based on the [N II], [S II], and [O I] BPT diagrams, following Kewley et al. (2006). Subsequently, the line fluxes are corrected for dust extinction using the Cardelli et al. (1989) reddening curve assuming  $R_V = A_V/E(B-V) = 3.1$ , and a fiducial intrinsic H $\alpha$ /H $\beta$  ratio of 2.85 for star-forming galaxies, and 3.1 for AGN-dominated systems (for case-B recombination

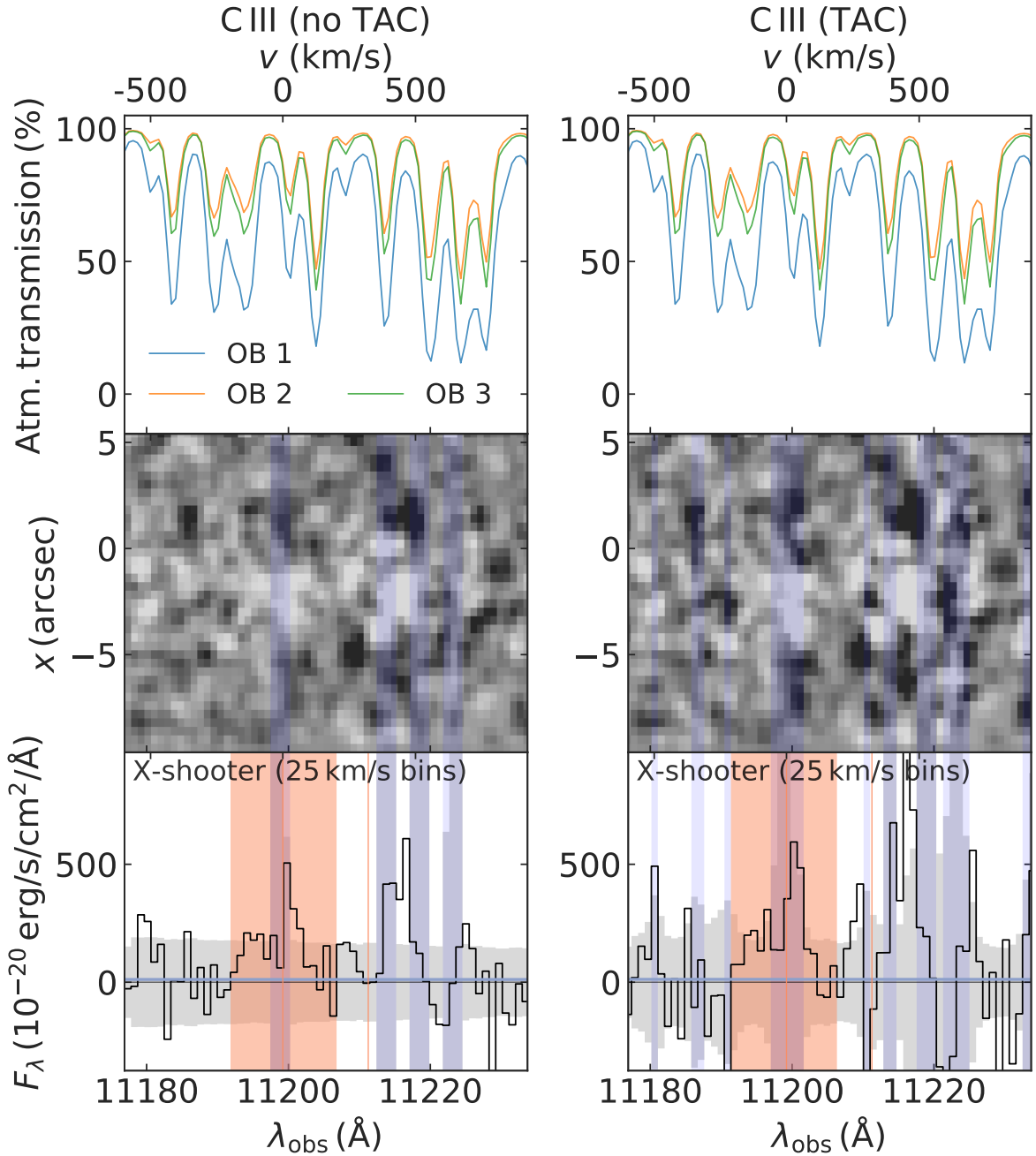


**Figure B.2** X-shooter spectra in the wavelength region where the C III doublet would be expected, both without and with TAC (see Sect. 2.2.1). The top row shows the resulting atmospheric transmission calculated by MOLECFIT. A region within  $-200 \text{ km/s} < v < 200 \text{ km/s}$  of the expected 1907 line centre, which has been used to place an upper limit on the flux, is highlighted in the bottom row of one-dimensional spectra.

at  $T = 10^4$  K and  $n_e \sim 10^2\text{--}10^4 \text{ cm}^{-3}$ , see [Kewley et al., 2006](#)). In this sample, 2484 galaxies or 27.7% have a SNR  $> 5$  [Ne III] detection.

### B.3 JWST ETC calculation

Given the observed Mg II  $\lambda 2796$  flux of  $5.0 \cdot 10^{-18} \text{ erg s}^{-1} \text{ cm}^{-2}$  (see Table 2.1) and assuming a typical flux ratio of  $F_{2796}/F_{2804} \approx 1.9$  between the Mg II lines at 2796 and 2804 (e.g. [Henry et al., 2018](#)), the total flux of the doublet would become  $7.6 \cdot 10^{-18} \text{ erg s}^{-1} \text{ cm}^{-2}$ . However, taking into account the lensing magnification of  $\mu = 29$ , we derive an intrinsic flux of  $2.6 \cdot 10^{-19} \text{ erg s}^{-1} \text{ cm}^{-2}$  at  $z = 4.88$ . We note that the uncertainty and spatial variation of the lensing magnification makes this only a rough estimate of the true intrinsic flux. Assuming an object with the same luminosity at  $z = 7$  (in which case Mg II would be observed at  $\lambda_{\text{obs}} = 2.24 \mu\text{m}$ ), this would lead to an observed flux of  $1.13 \cdot 10^{-19} \text{ erg s}^{-1} \text{ cm}^{-2}$ . The continuum flux density from our fit is  $2.29 \cdot 10^{-20} \text{ erg s}^{-1} \text{ cm}^{-2}$ <sup>–1</sup> or 383 nJy at  $\lambda_{\text{obs}} = 2.24 \mu\text{m}$ , which translates to  $2.5 \cdot 10^{-22} \text{ erg s}^{-1} \text{ cm}^{-2}$ <sup>–1</sup> or 4.18 nJy if it were unlensed at  $z = 7$ .

Alternatively, our estimate implies  $F_{2796} = 7.4 \cdot 10^{-20} \text{ erg s}^{-1} \text{ cm}^{-2}$ . This is inconsistent with a recent estimate from [Chisholm et al. \(2020\)](#), the difference being explained by the fact that their higher flux estimate (by a factor  $\sim 8$ ) arises from considering a source with a *H*-band magnitude of 25 (in the F160W filter; this corresponds to  $M_{\text{UV}} \simeq -21.9$  at  $z = 7$ ). The unlensed observed magnitude of RCS0224z5 is  $\sim 26.8$  mag, which at  $z \simeq 4.88$  translates to  $M_{\text{UV}} \simeq -19.6$ . This implies an observed magnitude of 27.4 at  $z = 7$  – a factor  $\sim 9$  fainter than a 25 mag source – and is instead appropriate when considering intrinsically fainter and hence more common sources. In a typical extremely deep field, one would on average expect less than one source at  $z \sim 7$  with magnitude 25, and the order of  $N \sim 1$  in a medium-deep field, compared to  $N \sim 2$  and  $N \gtrsim 70$  respectively for a  $m_{\text{UV}} \sim 27.4$  mag source (derived from the  $z \sim 7$  number counts in the  $5 \text{ arcmin}^2$  XDF and  $\sim 120 \text{ arcmin}^2$  CANDELS-DEEP fields presented in [Bouwens et al. 2015](#)).

Simulations<sup>1</sup> of the near-infrared spectrograph on *JWST* (NIRSpec), point out that for an (intrinsically) relatively faint object like RCS0224z5, detecting Mg II spectroscopically would be challenging: for example, a 10 ks exposure with the multi-object spectrograph observing mode at low resolution would result in a signal of Mg II at the level of  $0.65\sigma$  per spectral pixel (but we note that integrating over the few pixels containing the line could slightly increase the overall SNR). At  $R \sim 100$ , this would render the doublet (separated by  $\sim 770 \text{ km/s}$ ) unresolved as well. The same exposure would yield a SNR of 0.56 per spectral pixel at medium spectral resolution (the F170LP/G235M grating achieving  $R \sim 1000$  at  $\lambda_{\text{obs}} = 2.24 \mu\text{m}$ ), which would resolve the doublet down to  $\sim 300 \text{ km/s}$ . Finally, a deep (10 h) exposure allow a SNR of 0.67 per spectral pixel at high resolution ( $R \sim 2000$  or  $\sim 150 \text{ km/s}$ ). Still, for objects with a more intense episode

---

<sup>1</sup> *JWST* Exposure Time Calculator: <https://jwst.etc.stsci.edu>.

of ongoing star formation (possibly boosting the flux by a factor of a few, up to a factor  $\sim 8$  for a  $M_{\text{UV}} \simeq -21.9$  source as in Chisholm et al. 2020, as discussed above), or for lensed objects (like RCS0224z5), observations of Mg II would be feasible in deep spectroscopic surveys.

